The structure and evolution of magmatic complexes in fold-and-thrust belts: a case study of Cerro Negro, Neuquén Province, Argentina

by Meryem Derya Gürer

Thesis submitted for the degree of Master of Science

Physics of Geological Processes,

Department of Physics

December 2012

Faculty of Mathematics and Natural Sciences
University of Oslo

Det matematisk- naturvitenskapelige fakultet
Universitetet i Oslo

"The Beauty of the Mountain is hidden for all those who try to discover it from the top, supposing that, one way or another, one can reach this place directly. The Beauty of the Mountain reveals only to those who climbed it ..."

— Antoine de Saint-Exupéry

Acknowledgements

The work presented was carried out at the Centre for Physics of Geological Processes (PGP), University of Oslo between January and November 2012. A Centre of Excellence grant from the Norwegian Research Council to PGP supported the project financially. I would like to thank the Konrad-Adenauer-Foundation, Germany for guidance and financial support throughout my studies in Germany, Australia and Norway. My time as a Master's student was academically and personally very rewarding. Many people have helped me in different ways along the way. This thesis would not have been written without their support and company.

First, I want to thank Olivier Galland, my main supervisor, who initiated the project and field mapping in the Argentinian Andes. I have greatly benefited from his insight and knowledge of Andean Geology. Without him I would not have had the chance to embark on this project. I am grateful for his support and enthusiastic supervision. Thank you for providing me with guidance and giving me the room to pursue my own ideas. I am grateful to Fernando Corfu for his co-supervision, for introducing me to geochronology and for even taking me to see some Norwegian rocks with "proper zircons". I admire his patience, attention to detail and wit. Thank you for always motivating me and taking the time to discuss and read my work.

Else-Ragnhild Neumann has provided invaluable help with the geochemical interpretation. I want to thank particularly Andreas Beinlich, who helped a great deal with fieldwork preparations, introduced me to the different laboratories in Oslo and acted as a mentor early on in the project. Henrik Svensen has given me a lab job, which I much appreciated – even though the demands of my project left not much time for it. Special thanks to Caroline Sassier for her delicious cooking during the fieldwork and for several days of field assistance. Eberhard "El Gringo" and Jonathan assisted me skillfully and successfully with my attempts at Argentinian horse riding on the Black Mountain. H. Leanza helped with logistics and permits in Argentina. ¡Muchas Gracias por todo!

This project would not have been possible without co-operations with several universities in Germany, which allowed me to use their laboratories. Many thanks to P. Späthe (Würzburg), R. Hoffbauer (Bonn), E. Hoffmann, C. Münker and U. Casper (Cologne). I am grateful to Gunborg Bye Fjeld for careful guidance in the Oslo mineral separation laboratory. I would like to thank all colleagues and fellow students at PGP, especially Liene, Kristin, Kerstin and Hedda. I am grateful for discussions and input from Douwe, Abi and Mat at various times. I greatly appreciate the continuous support I received from Chris Ballhaus over the years.

I am indebted to Leonie for all her support and help, both emotional and practical. I wish to thank Mari, Achim, Vera, Thomas and Javier for their friendships that have begun during my undergraduate studies in Bonn and have survived great distances. It has been a great experience to live with flatmates throughout my stay in Oslo. I am glad to have met Katerina! Special thanks go to my Norwegian hosts Kjersti, Armin and Sten for sharing their homes; I always loved coming back to you. Matt's creativity and enthusiasm made the grey November weeks before the deadline more colourful. I am very grateful for the motivation, driving force and inspiration I received from my friends Conny, Julia and Nur. I especially appreciated Conny's generosity in sharing her office, coffee, music and frustration during the quiet summer months in Oslo.

Finally, I want to thank Mark Lauer and Marion Kohler for sharing their admirable views on life and science.

To my mother, who always supported me.

Table of Contents

Preface

In contrast to the classical concept of magma ascent in extensional settings, recent studies show that volcanism also occurs in compressional settings. The nature of the interplay between magmatism and tectonics in fold-and-thrust belts however, remains a major question, notably in active margins. The mechanisms of magma transport in such settings and whether magmatism affects tectonic deformation need to be addressed. The question of whether magma can reach the surface in zones of regional compression is not only a matter of scientific debate, it also has implications for our understanding of natural resources and the mitigation of natural hazards, such as volcanic eruptions and earthquakes (*Tibaldi et al.*, 2010).

Detailed studies of well-exposed magmatic systems that have been emplaced in fold-and-thrust belts may help to address some first order questions related to shallow magmatic systems that evolve in fold-and-thrust belts: how does magma reach the surface in a shortening crust? Is there a link between tectonic deformation and magma emplacement? Is magma following crustal heterogeneities (i.e. thrust ramps)?

Even though very promising, interdisciplinary studies that link structural field observations with petrological, geochemical and geochronological information remain relatively rare. This study aims to define and answer some of these first order questions. It is based on detailed structural mapping and sampling of a well-exposed intrusive complex emplaced in a fold-and-thrust belt. As a case study we chose the area between the towns of Tricao Malal and Chos Malal in the Neuquén Province, Argentina. The stratigraphy of the surrounding sediments is well constrained. Based on existing studies and new data obtained during this fieldwork, a new geological map has been constructed. Cross-sections illustrate the structural architecture of the study area, especially the relation between magmatic intrusions and structures in the country rock. Absolute ages and geochemical data were obtained for a range of magmatic conduits with different geometries, resolving the compositional and temporal relationships between different magma conduits. The integration of structural observations with absolute ages allowed the regional state of stress during magma emplacement to be resolved. Subsequently, these were integrated with geochemical data, to provide insights into whether or not the magmatic products of Cerro Negro are distinct and more evolved than adjacent systems and of the average magmatic arc.

Introduction

Magmatism in compressional tectonic settings: initial controversy and recent advances

Magmatic intrusions are the major mechanism through which magma is transported and stored in the Earth's crust. The study of their formation and emplacement is important for developing our understanding of the evolution of the Earth's crust and major heat and mass transport mechanisms in general. Magmatic activity occurs in different plate tectonic settings (convergent, divergent, strike-slip, intraplate) and produces magmas that are emplaced at different levels, ranging from the lower-middle crust to the surface. Volcanic arcs form above subduction zones and manifest the interplay between tectonics and volcanism. They commonly represent areas of overall compression. Extensional zones are commonly found in the back-arc region, as well as transpression or strike-slip tectonics in the volcanic front (*Tibaldi et al.*, 2010). Magmatic intrusions provide a record of stress conditions in the crust during magma emplacement. This review aims to give an overview of the evolution of our understanding of magmatic systems and the state-of-the-art knowledge of magma emplacement in compressional settings with emphasis on active margins.

Structure and shape of magma conduits

Different tectonic settings translate into different states of stress in the brittle crust, which in return exert a fundamental control on how magma reaches the surface. Magma intrudes into the brittle crust by hydraulic fracturing, forming sheet intrusions with different geometries, ranging from vertical over inclined to horizontal (*Hubbert and Willis*, 1957; *Sibson*, 2003). Sheet intrusions are tabular bodies of magma with very small aspect ratios of thickness/length, typically 10^{-2}-10^{-4} (*Walker*, 1986; *Rubin*, 1993; 1995). This means that they can vary from sub-centimetre scale to many metres in thickness, whereas the lateral dimensions can extend over many kilometres. Sheet intrusions that cut discordantly through surrounding planar structures (i.e. bedding) are called dykes. In contrast, concordant sheet intrusions that run parallel to planar structures surrounding them, are called sills (*Best*, 2003). Dykes are mostly vertical to subvertical and are not limited to a particular tectonic regime, whereas sills are mostly horizontal, but can also be curved where the host rock is deformed. Overall, sills are concordant with respect to stratigraphic layering, but local discontinuities and irregularities are common. As with dykes, sills have been recognised in different tectonic settings.

Magma transport and emplacement mechanisms

Sheet intrusions are inferred to form by hydraulic fracturing in the brittle crust. Thus, magma is preferentially emplaced into the plane (σ_1-σ_2) perpendicular to the least principal stress component (σ_3) (*Sibson*, 2003). In extensional and strike-slip regimes, magmatic dykes are generally expected to be vertical and magma rises along vertical fractures perpendicular to the least principal stress (σ_3) (Figure 1: *Cas*, 1987; *Watanabe et al.*, 1999). In compressional regimes, magma conduits are expected to be horizontal, as compressional stresses and rheological boundaries enhance the formation of

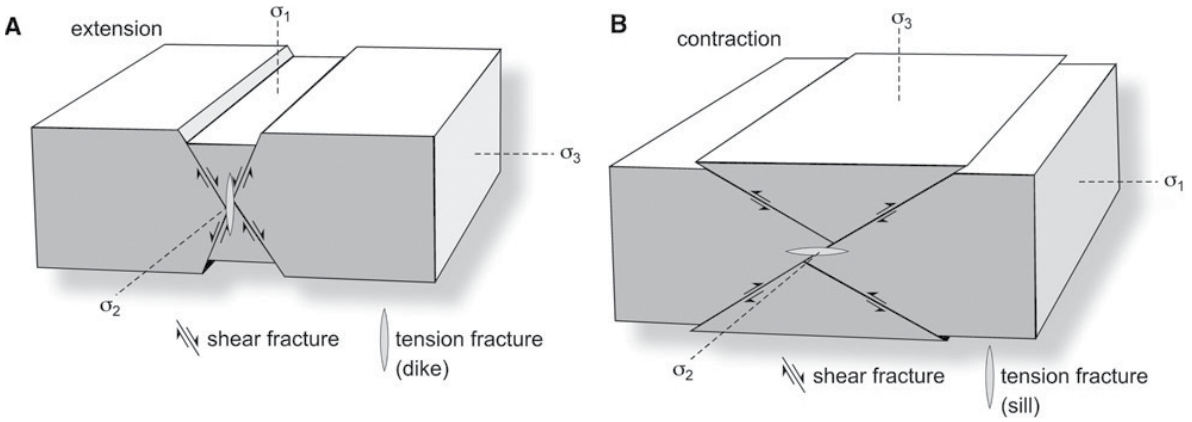

Figure 1: *Simplified stress regime, shear and tension fractures in the brittle upper crust, A) extensional stress regimes favour the development of normal and steeply dipping shear fractures, while tension fractures are (sub-) vertical (dykes), perpendicular to the least compressive principle stress (σ_3). B) In compressional stress regimes, where σ_3 is vertical, the reverse and gently dipping orientation of shear fractures leads to (sub-) horizontal shear fractures (sills). Magma rise and emplacement are expected to be more favourable in extension than in compression, as vertical tension fractures may act as preferential magma pathways. From Ferré et al. (2012).*

flat-lying intrusions (*Ferré et al.*, 2012).

Consequently, because magma conduits in compression are expected to be horizontal, volcanism has been thought to require regional extension, and compressional settings were widely assumed to impede magma from reaching the surface (*Hamilton*, 1994; *Watanabe et al.*, 1999). This is because in compressional settings in the brittle crust, the principal stress (σ_1) and the resulting hydraulic fractures are horizontal (Figure 1; e.g. *Hubbert and Willis*, 1957; *Sibson*, 2003; *Ferré et al.*, 2012). Therefore, subhorizontal sills are expected to form without associated surface volcanism, instead of vertical feeder dykes that transport magma upward.

This theoretical argument has led many authors to the statement that volcanism should be rare, if not absent, in regional compression. As a consequence of this, it was also concluded that

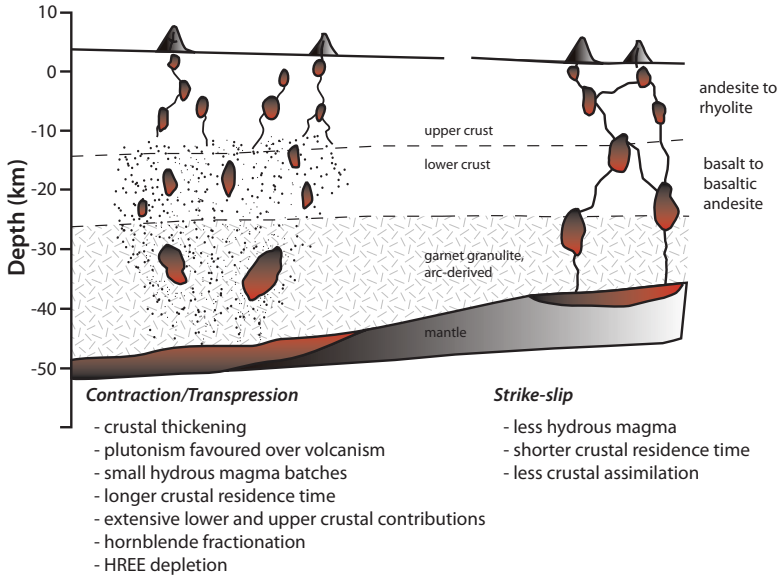

Figure 2: *Diagram illustrating the control of crustal stress state on the petrology and geochemistry of magmatic rocks. Magmas in contractional/transpressional settings (left), and strike-slip settings (right) show several distinct characteristics. The relative proportions of source region and processes (fractional crystallisation, assimilation hybridisation and mixing) vary between these discontinuous stress states. From Tibaldi et al. (2010).*

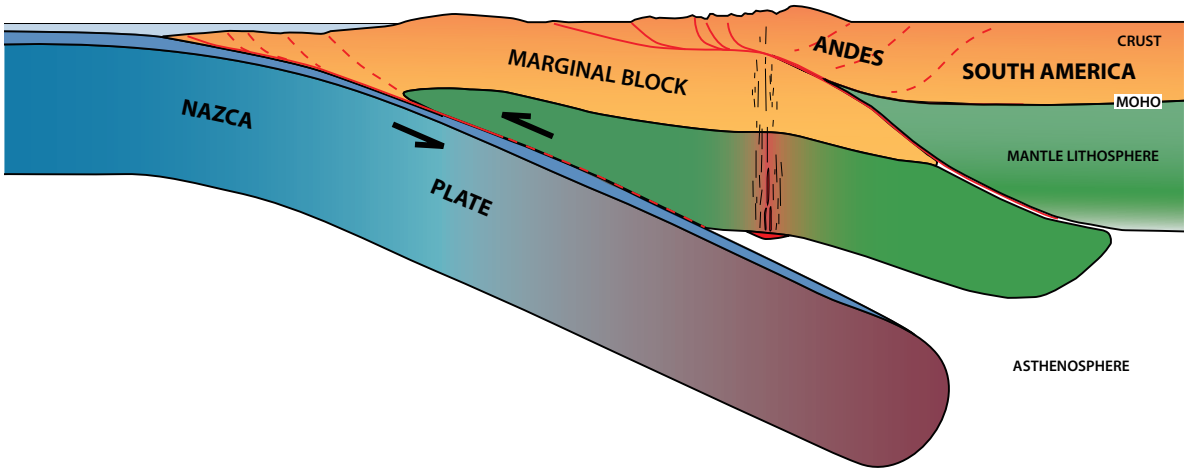

Figure 3: *Simplified cross-section across the Nazca-South America plate boundary and the Andes. Faults are in red. Position of present-day volcanic arc and possible feeding across the lithosphere are indicated. It should be noted that magma pathways and faults are not directly associated with each other. Modified from Armijo et al. (2010).*

magmas are stored in deeper levels of the crust (e.g. *Glazner and Bartley*, 1994; *Hamilton*, 1994; *Watanabe et al.*, 1999). According to *Tibaldi et al.* (2010) compressive stress regimes lead to more diffuse magma transport pathways, longer crustal residence times and pronounced plutonism in general. It has been invoked that magmas emplaced in compressional regimes interact more with the crust and magma mixing is a common process. The petrologic and geochemical effects include higher degrees of crustal contributions to ascending magmas, and a hydrous fractionating mineral assemblage (Figure 2). *Cembrano and Lara* (2009) have concluded that magmas that migrate under crustal compression are generally more evolved.

This assumption has been challenged by several counter examples. Tromen volcano, Argentina, displays bimodal volcanism that is commonly assumed to be diagnositic of extensional tectonics (*Galland et al.*, 2007b). There are examples of basaltic magmas erupted from volcanic systems in compression, where the crust has been considerably thickened (e.g. in the Altiplano and Tibet), (*Trumbull et al.*, 2006; *Mo et al.*, 2007). On the contrary, there are volcanoes that erupt highly evolved magmas even though they are known to be in an extensional setting (e.g. Askja, Iceland), (e.g. *Macdonald et al.*, 1987).

The apparent contradictions arising from these studies illustrate that our current understanding of the tectonic control on the chemistry of magmatic systems is rather poor. This is mainly a consequence of the dominating assumption that volcanism in compression is rare if not absent. The hypothesis that faults and magma pathways have no connection to each other is also illustrated by the simple sketches of magma pathways (Figure 3) in active margins (straight from the mantle to the surface) found in most textbooks and scientific articles (e.g. *Kapp et al.*, 2007; *Armijo et al.*, 2010).

Furthermore, the apparent link between volcanism and regional extensional tectonics leads *Watanabe* (1999) to the conclusion that the overall stress state of volcanic arcs at convergent margins should be strike slip (with σ_3 and greatest principal stress, σ_1, both horizontal) instead of compressional reverse (σ_3 vertical). In other words, local extensional domains have been invoked to explain the occurrence of volcanism in dominantly compressional settings. Some of the reasoning for this may be related to the fact that convergence of

lithospheric plates is generally more often oblique than strictly perpendicular (e.g. *McCaffrey*, 1996).

Early work pointed out that there may be a strong link between tectonics and magmatism and that deformation may favour magma ascent in the crust (*Cloos*, 1923). This intuitive concept has been further developed by analogue experiments and physical models (*Kalakay et al.*, 2001; *Galland et al.*, 2003; *Tibaldi*, 2005; *Galland et al.*, 2007a; *Galland et al.*, 2007b; *Tibaldi and Pasquare*, 2008). In recent years, there is growing field evidence for volcanism in compressional settings at active margins (*Tibaldi*, 1995; *Galland et al.*, 2007a; *González et al.*, 2009), which contradicts a well-established paradigm and subsequent developments based on it.

In addition to the most fundamental question - how does magma rise through the brittle crust that is under compression? - there are many open questions regarding the transport and emplacement of magma in the brittle crust: does space have to be provided in order to emplace magma or does the "room problem" diminish when the three dimensional geometry of such bodies is taken into account? Does magma overpressure exert a big enough driving force for the magma to rise (*Legrand et al.*, 2002)? Do crustal heterogeneities serve as preferential magma pathways? Is it possible that magma is horizontally deflected when it rises through a c. 40 km thick heterogeneous crust?

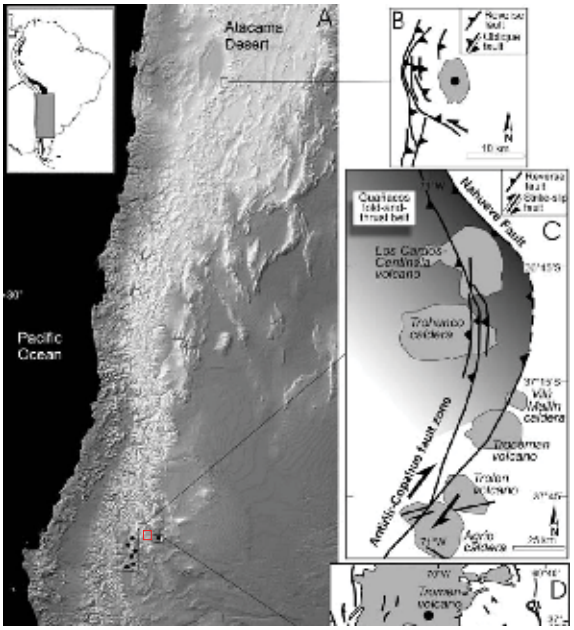

Figure 4: *Location of a selection of field examples from the Argentinian-Chilean Andes mentioned in the text and their relation to thrusts. A) Overview of the location of selected magmatic systems. B) Small volcanic edifice trapped in a thrust system resulting from contractional neotectonics east of the Atacama Desert, Chile (Branquet and de Vries, 2001). C) Plio–Quaternary volcanoes aligned along the Andean frontal thrust zone in Argentina (Tibaldi, 2008). D) Tromen volcano, Argentina, that has been active during compressional deformation (Galland et al., 2007b). The location of the study area presented here (Cerro Negro de Tricao Malal), west of Tromen volcano in the Neuquén Basin, Argentina, is marked with a red bounding box. Modified from Tibaldi et al. (2010).*

Examples of volcanism in compression

There is growing field and geophysical evidence of coeval compressional deformation and volcanism. Recent studies (e.g. *Tibaldi*, 2005; *Galland et al.*, 2007b; *González et al.*, 2009) suggest that some volcanoes are active in an overall compressional tectonic setting. Examples include El Reventador volcano in Ecuador, which has formed in a transpressional or compressional regime (*Tibaldi*, 2005; *Tibaldi and Pasquare*, 2008), Tromen volcano in Argentina, which has grown in a compressional setting (*Marques and Cobbold*, 2002; *Galland et al.*, 2007b), and several volcanoes in the Salar de Atacama region of the Central Andes that manifest coeval compressional deformation and magmatism (*Branquet and de Vries*, 2001; *González et al.*, 2009). In other cases, the

temporal link between contractional tectonics and volcanism has not been unequivocally determined (e.g. Taapaca volcano in Chile) (*Clavero et al.*, 2004). In Japan, field observations and geophysical data also suggest that there is a link between contractional tectonics and magmatism (*Miura*, 2000; *van der Werff*, 2000; *Yoshida*, 2001; *Townend and Zoback*, 2006). The Gangdese arc in southern Tibet is another example of a magmatic system developed in compression (*He et al.*, 2007; *Kapp et al.*, 2007).

All of the aforementioned field-based observations challenge the assumption that volcanism is rare, if not absent in compressional regimes (*Glazner and Bartley*, 1994; *Hamilton*, 1994; *Watanabe et al.*, 1999). Additionally, it has been pointed out that all of the mentioned field examples, e.g. Guagua Pichincha in Ecuador (*Legrand et al.* 2002), volcanic edifices in the Calchaquì valley of Argentina, (*Guzmán et al.*, 2006) and several volcanic complexes in the eastern Neuquén Andes (*Folguera and González Díaz*, 2006; *Miranda et al.*, 2006) amongst numerous others are associated with thrust faults (Figure 4), suggesting that thrusts may control the transport and storage of magma.

Structural relationships between magma conduits and faults

Shallow magma transport and emplacement is the most direct geological record of magmatic plumbing systems and adjacent faults, and thus represents an important volcanic-tectonic link. One key issue related to the study of such systems and the underlying structures is the lack of good exposures, as the volcanic products mostly cover them. This is especially the case in active volcanic arcs. Therefore, the study of exhumed or eroded volcanic complexes is promising. Because the field relationships are not always clear, the study of the relationships between tectonic structures and magmatic conduits should be combined with scaled analogue experiments.

Complex relationships between tectonic structures and magmatism have been well documented in the Andes and Japan, where the dominant deformation regime is compressional (e.g. *Legrand et al.*, 2002; *Tibaldi*, 2005; *Galland et al.*, 2007b; *González et al.*, 2009). A number of studies clearly show that active volcanoes in compressional settings are associated with thrust faults, most of them being on top of the hanging wall of thrusts (e.g. *Galland et al.*, 2007b). This strongly suggests that faults and magma pathways are not decoupled from each other and that faults have a substantial effect on the emplacement of magma in the brittle crust. As a consequence, one of the fundamental uncertainties related to magma emplacement in compressional settings is whether magmas rise along pre-existing faults or, whether thrusts form in response to magma emplacement.

Recent studies have pointed at the importance of crustal heterogeneities (e.g. folds and faults) as preferential magma pathways (*Kalakay et al.*, 2001; *Galland et al.*, 2003; *González et al.*, 2009; *Ferré et al.*, 2012), arguing that compressional deformation and magmatism are not two independent processes. If this is the case, the study of feedback relationships between magmatism and deformation is crucial for our understanding of active margin tectonics and the evolution of fold-and-thrust belts in general.

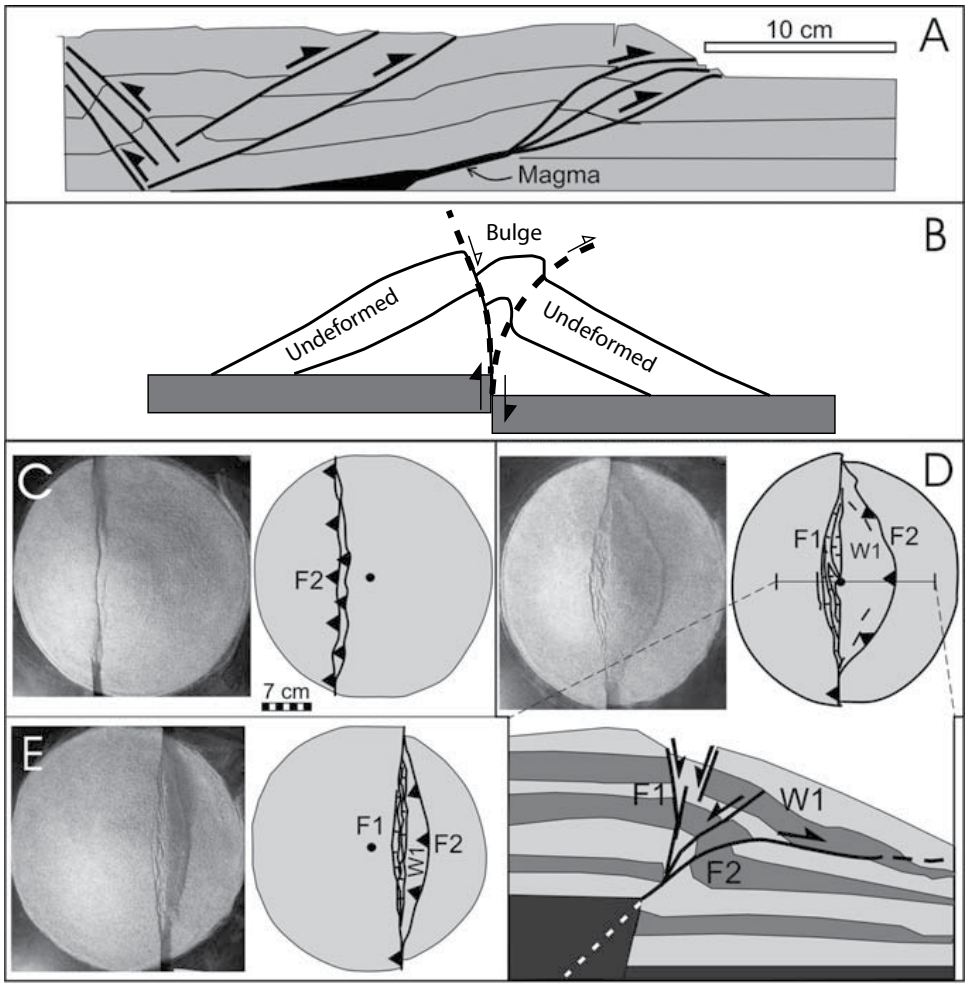

Figure 5: *Laboratory experiments of volcanoes in contractional settings (with the exception of B Merle et al. (2001), where deformation in a volcanic edifice located above a vertical fault has been studied). (A) Galland et al. (2007a) illustrates the movement of magma along thrust planes. Series of experiments (C, D, E) of volcanic edifices lying above thrusts with different position with respect to the cone (from Tibaldi, 2008); (C) cone summit located on the footwall block, (D) above: the cone summit above the surface trace of the substrate fault, (D) below: section view of the deformation within the cone; (E) cone summit on the hanging wall block. Modified from Tibaldi (2005).*

Magma emplacement has been documented and modelled for different tectonic settings, with emphasis on the mechanism that allows the migration of magma in a shortening crust (Figure 5; *Hutton*, 1997; *Kalakay et al.*, 2001; *Musumeci et al.*, 2005; *Tibaldi*, 2005; *Zellmer et al.*, 2005; *Galland et al.*, 2007a; *Galland et al.*, 2007b; *Mazzarini et al.*, 2010; *Ferré et al.*, 2012). Scaled physical models of magmatic systems can provide important insights into the mechanics of magma intrusion in compressional regimes. From laboratory experiments we know that the shape of magmatic intrusions is primarily controlled by the ratio between intrusion and deformation velocity (*Roman-Berdiel et al.*, 1995; *Corti et al.*, 2005; *Galland et al.*, 2007a; *Mazzarini et al.*, 2010; *Montanari et al.*, 2010). High injection rates coupled with low deformation rates (dominance of magma emplacement over deformation) result in circular intrusions, whereas low injection rates coupled with high deformation rates (dominance of deformation over magma emplacement) results in elongated intrusions (*Corti et al.*, 2005; *Mazzarini et al.*, 2010; *Montanari et al.*, 2010). These studies come to the following conclusions: (1) magmas can rise along thrusts and eventually reach the surface in tectonic regimes characterised by contractional deformation, (2) unconsolidated intrusions may

influence thrust formation. These points support the hypothesis that deformation does control the emplacement of magma in a contracting crust.

Ferré et al. (2012) studied the influence of brittle tectonic structures on the emplacement of magmas of various compositions in compressional settings for two experimental cases, where magma intrusion and compressional deformation are either coeval or diachronous. Their results suggest that active and pre-existing structures, such as fault thrust and ramps, can act as preferential magma pathways.

In the case of Tromen volcano, field observations show that vertical magma conduits are located above the thrust hanging wall (*Galland et al.*, 2007b). However, the analogue experiments are unable to reproduce this feature observed in nature. Instead, in all experiments magma erupts along the trace of the thrust (*Galland et al.*, 2007a). This inconsistency between field observations and laboratory experiments suggests that the assumptions used in the experiments are too simple and that there is an underlying process that is not yet understood. It should be kept in mind that laboratory experiments represent a simplified approximation of geological systems. However, some important first order statements can be made based on such experiments. *Mazzarini et al.* (2010) pointed out that analogue experiments allow us to study simple, end-member states of stress (i.e. purely compressional), where the thermal effects of intrusions on the country rock cannot be taken into account. Thus, faulting and bending take place without the formation of cleavage/ductile deformation.

Based on field, geophysical (Guagua Pichincha, El Reventador volcanoes) and laboratory observations, some workers have suggested a physical, vertical partitioning of magmatic systems at depth (*Legrand et al.*, 2002; *Galland et al.*, 2007a; *Tibaldi*, 2008; *González et al.*, 2009) in order to explain the upward transport of magma in compressional systems (Figure 7).

In the case of Guagua Pichincha volcano, such a vertical partitioning in the state of stress (i.e. orientation of stress tensors) has been measured (Figure 6; *Legrand et al.*, 2002). The stress tensors of the earthquake swarms below the city of

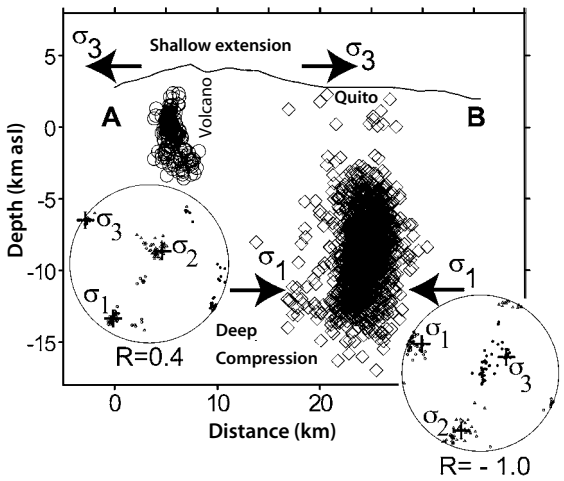

Figure 6*: Crustal section showing stress tensors of earthquake swarm below Guagua Pichincha volcano (A) and the Quito swarm (B). Note the adverse orientation of the stress tensors. These suggest extension at the shallow level of the volcano (A) and deep compression under Quito (B). From Legrand et al. (2002).*

Quito (located 15-20 km east of the volcano) are similar to the regional stress tensors. Both suggest compression. In contrast, the stress tensors below Guagua Pichincha volcano are very different from the regional and Quito stress tensors, suggesting a shallow, local extensional stress regime.

The swarms at Guagua Pichincha and Quito, which are most likely caused by the same magmatic system, suggest that there are shallow extensional domains in an overall compressive region and that such transition may be influenced by the volcanic edifice itself (*Legrand et al.*, 2002).

The inconsistency between the laboratory experiments and field observations further supports the hypothesis of vertical partitioning of

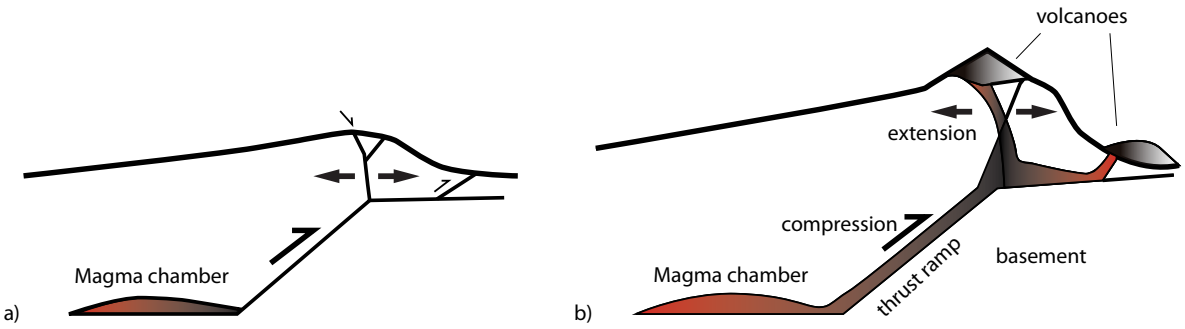

Figure 7: *Illustration of the proposed partitioning of magmatic systems, possible magma pathways and emplacement mechanisms in compressional settings such as the Central Andes. a) Beginning of compression during which blind reverse faults, fold propagation folds, and/or fault bend folds accommodate horizontal shortening. b) Ongoing compression during which magma transported to the upper crust may be stored at subhorizontal reservoirs (sills), at fault flat segments, and/or within the cores of anticlinal structures. Subsequently, once magma pressure overcomes the gravitational load, reverse faults may act as fault valves allowing magma to migrate from the flat reservoirs to the surface. Volcanoes occurring at the hinge zone of anticlines may result from a combination of concurrent compression at the magma-filled core of the fold, and extension at the hinge zone, causing magma to ascend through a tear in the hinge zone (e.g. Tibaldi et al., 2008). Illustration is not scaled. Modified from Gonzáles et al. (2009).*

magmatic systems in compressional settings (Figure 7). *Gonzalés et al.* (2009) conclude that magma can reach the surface in a purely compressional system if one of two end-member mechanisms occurs: (1) an interconnected network of sills and shallow thrusts is formed due to magma overpressure (similar to hydrothermal fluid flow mechanisms proposed by *Sibson* (1996), and/or (2) overcoming a critical state of stress, reverse faults are activated and release the magma previously stored in sills or in the cores of anticlines. The latter has been suggested as a mechanism for pluton formation (*Kalakay et al.*, 2001).

Even though this proposed partitioning has not yet been directly observed in nature, it may indeed account for some of the inconsistencies between field observations and analogue experiments. If such a transition exists, it poses the question: what is the mechanism that controls the transition between the deep and shallow parts of the system? What is the exact geometry of such a system and what is the relationship between the magma conduits and the tectonic structures?

To answer some of these questions, detailed structural field studies of exposed, relevant intrusions in fold-and-thrust belts are required. One possible candidate is the well-exposed Cerro Negro de Tricao Malal intrusive body emplaced in the Agrio fold-and-thrust belt in northwestern Patagonia, Argentina.

Summary

The nature of the interplay between compressional tectonics and volcanism is a fundamental question and long standing debate in active continental margin settings. Many structural field observations and analogue experiments come to the conclusion that faults are closely related to magma transport in all types of tectonic setting (*Hutton*, 1982; *Guineberteau et al.*, 1987; *Hutton*, 1988; *D'Lemos et al.*, 1992; *Corti et al.*, 2005). Analogue experiments of magmas emplaced in compressional settings show geometric similarities with natural examples (*Hutton*, 1997; *Kalakay et al.*, 2001; *Musumeci et al.*, 2005; *Tibaldi*, 2005; *Zellmer et al.*, 2005; *Galland et al.*, 2007a; *Galland et al.*, 2007b; *Mazzarini et al.*, 2010; *Ferré et al.*, 2012) and as such, analogue modelling may represent a valuable approach in the study of magma emplacement mechanisms in actively shortening regions. There is little doubt concerning the existence of feedback mechanisms between volcanism and tectonics. However, many important questions related to this topic remain open for debate, the most fundamental being: how does magma reach the surface in compressional settings? Is magma following thrusts? Is there a vertical partitioning of magmatic systems in compression and if so, is it possible to observe such transition? What controls the depth of it? Detailed structural field studies of exposed subvolcanic intrusions are thus required, if we want to understand modes and conditions of magma emplacement, the internal structure of volcanoes and magma migration pathways in general.

This project aims to answer the following questions by integrating structural field observations with geochronology and geochemistry: do magma conduits (sills and dykes) follow tectonic structures (folds and faults)? Is there a vertical partitioning of the Cerro Negro magmatic system? Is it observable? What is the temporal relationship between magma conduits and the surrounding sediments? Is magmatism contemporaneous with regional shortening? Is the chemistry of the magmatic conduits of Cerro Negro distinctive of a particular stress regime? The answers to these questions may indeed provide insight into broader problems related to magma emplacement in compressional settings.

Geological setting

The Andean Cordillera

The Andean Cordillera is the world's second highest orogenic belt and longest continental mountain chain extending over 8000 km along the western margin of the South American Plate. The Andean Cordillera was created as a result of the subduction of the oceanic Nazca Plate beneath the continental South American Plate which began in the Mesozoic (*Forsythe*, 1982). The shortening in the Andean margin and ongoing intense volcanic activity has been evident along the volcanic arc for more than 30 m.y. (*Allmendinger et al.*, 1997; *Trumbull et al.*, 2006).

The uplift of the modern Andes started in the Late Oligocene after a major reorganisation of the oceanic plates in the eastern Pacific (e.g. *Tebbens and Cande*, 1997) and accelerated convergence between the Nazca and South America Plates (*Allmendinger et al.*, 1997). The Andean Cordillera is continuous along strike, but a lateral tectonic and magmatic segmentation related to subduction geometry variations (from near horizontal to 30° eastward dipping) coinciding with segmentation of the downgoing Nazca Plate has been recognised (*Barazangi and Isacks*, 1976; *Jordan et al.*, 1983). Furthermore, the Andean mountain chain displays topographic features that seem to correlate with the dip of the downgoing plate (*Jordan et al.*, 1983; *Isacks*, 1988; *Gephart*, 1994), according to which they are subdivided into three morphostructural zones: the Northern Andes, Central Andes and Southern or Patagonian Andes (Figure 8).

The Central Andes are characterised by a strong symmetry. This segment of the mountain belt is the widest at 600-800 km, and hosts elevations over 5 km. Northwards and southwards, the width and altitude of the chain decrease smoothly. The crustal thickness is also greatest in the Central Andes (60-80 km), compared to approximately 40 km elsewhere (*Jordan et al.*, 1983; *Gephart*, 1994; *Capitanio et al.*, 2011).

The Northern Andes extend from Venezuela in the North (12°N) to Peru in the South (10°S) and result from the subduction of several plates (Cocos, Nazca and Caribbean Plates). They consist of three parallel ranges that are concave to the East, and a few hundred kilometres wide. The altitude in the southern part reaches 6000 m (Peruvian Cordillera Blanca).

Figure 8: *Segmentation of the Andean Cordillera. Triangles mark the location of volcanoes. The volcanic zones (NVZ= Northern Volcanic Zone, CVZ= Central Volcanic Zone, and SVZ= Southern Volcanic Zone) are separated by volcanic gaps. Topography data from the Shuttle Radar Topography Mission (SRTM).*

The Central Andes extend from Peru and Bolivia in the North (10°S) to Chile and Argentina in the (35°S). This portion results from the subduction of the Nazca Plate under the South American Plate. It is characterised by an arcuate

geometry concave towards the West. This corresponds to the curved Bolivian orocline. The most outstanding feature of this region is the broadening of the Cordillera, embedding the Altiplano and Puna plateaux, which have average elevations above 4 km. The Altiplano-Puna Plateau (1800 km long and 350-400 km wide on average) is the highest plateau associated with abundant magmatism and is second only to the Tibetan Plateau in height and extent (*Allmendinger et al.*, 1997).

The Southern Andes, extend from Chile to Argentina between 35°S and 55°S and result from the subduction of the Nazca and Antarctic Plates that interact with the Antarctic Peninsula and Scotia Plate. The altitude within the several hundred kilometres long straight chain decreases progressively from the North (4000-5000 m) to the Tierra del Fuego in the South (2000-3000 m).

The volcanic zones of the Andes, namely the Northern Volcanic Zone (NVZ), Central Volcanic Zone (CVZ), and Southern Volcanic Zone (SVZ), are located along the western edge of South America. The main volcanic arc is the largest in the Central Andes. The boundary between the volcanic zones is marked by volcanic gaps that result from the flattening of the subduction zone (*Thorpe et al.*, 1984). On both sides of the central segment, a gap of volcanism marks the transition between the CVZ, the NVZ and the SVZ.

The SVZ, roughly located between 33°S and 46°S, has formed due to the slightly dextral-oblique subduction of the Nazca Plate under the South American Plate along the Peru-Chile Trench (*Cembrano and Lara*, 2009). The northern end of the SVZ is marked by the flat-slab subduction of the Juan Fernández Ridge, which is linked to a volcanic gap called the Pampean flat-slab segment since the late Cenozoic (*Charrier et al.*, 2007). The southern limit of the SVZ is marked by the Chile Triple Junction, where the Chile Rise subducts under South America, giving rise to the Patagonian Volcanic Gap.

This part of the volcanic zone has been subject to various studies dealing with the relationship between tectonics and magmatism (e.g. *Lopez-Escobar et al.*, 1977; *Hildreth and Moorbath*, 1988; *Folguera and González Díaz*, 2006; *Kay and Ramos*, 2006). In the SVZ, the arc has a well-defined volcanic front and areas of back-arc extension with transitional zones in between.

Evolution of the Andean subduction through time

Oceanic plates have been subducting nearly continuously under the Pacific continental margin since the Late Palaeozoic (*Tankard et al.*, 1995). Recent plate reconstructions (*Pardo-Casas and Molnar*, 1987; *Somoza*, 1998) provide good constraints on the Cenozoic convergence history at the western margin of South America (Figure 9). According to these studies the convergence geometry at the latitude of the Neuquén Basin changed dramatically through time, but remained fairly constant at the latitude of the study area for the past 49.5 Ma.

The evolution of this subduction is well constrained by magnetic anomalies in the surviving parts of the downgoing plate, the oldest being Paleocene (*Pardo-Casas and Molnar*, 1987). Older stages of subduction are less well constrained.

According to *Cobbold et al.* (1999), subduction was accompanied by thinning of the continental lithosphere in the Triassic and Jurassic. Throughout southern South America NW-SE trending rift basins formed in the Triassic. One of these basins is the Neuquén Basin in northwestern Pa-

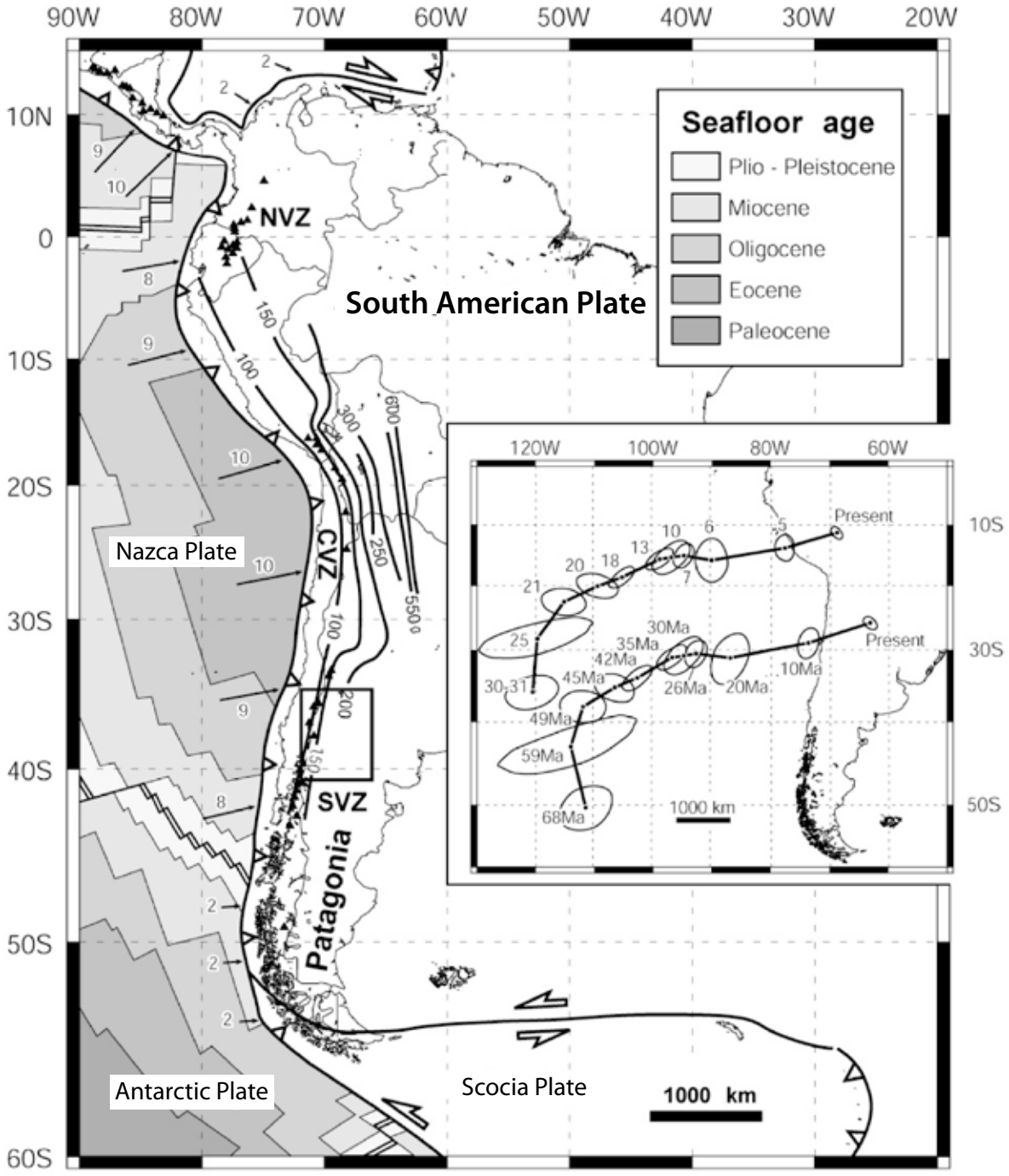

Figure 9: *South American plate tectonics since the Tertiary. Black box marks the location of the Neuquén Basin. The Nazca and Antarctica oceanic plates subduct underneath the Pacific margin of South America (marked by white triangles). The main map shows the increasing seafloor age with distance from the spreading ridges (darker shades of grey with increasing age), the relative convergence speed between the oceanic plates and the South American Plate (cm/year) and the Andean arc volcanoes (black triangles). Steep segments of the subducted Nazca slab correlate with volcanoes of the NVZ, CVZ, and SVZ. Particle paths for Nazca Plate relative to South America (inset) are for period from 68 Ma (anomaly 30-31) to Present. Convergence has been relatively steady since 49.5 Ma (anomaly 21). Modified from Cobbold et al. (1999).*

tagonia, which will be described in more detail in the following sections. The basin was filled with marine deposits during the continued subsidence in the Jurassic and active rifting stopped in the Toarcian (181 Ma). The tectonic regime shifted towards a more compressional from the Late Cretaceous onwards. Uplift and erosion of the magmatic arc led to the deposition of clastic

sediments. The Neuquén Basin underwent inversion in the Tertiary (*Uliana et al.*, 1995). The vector of relative motion between the Nazca and Northern Patagonia (at 40°S) was very oblique to the margin during the Palaeogene and became progressively less so during the Neogene (*Pardo-Casas and Molnar*, 1987).

The rate of convergence also changed through time, being relatively rapid in the Eocene, decreasing in the Early Oligocene and increasing again in the Late Oligocene to Early Miocene. This strong increase in convergence rate in Late Oligocene time is coeval with the development of important compressional tectonic characteristics and the onset of Late Cenozoic magmatism. In Late Miocene times convergence rate slowed down (*Somoza*, 1998).

Currently, the convergence geometry is oblique across the main Cordillera and the foothills of Patagonia. The principal compressive stress trends NE-E, subparallel to the vector of relative motion (*Zoback*, 1992). Horizontal compression is also confirmed by in situ stress measurements (*Guzmán et al.*, 2007), GPS measurements (*Klotz et al.*, 2001), earthquake focal mechanisms (*Chiu*, 1992; *Assumpção and Araujo*, 1993; *Meijer et al.*, 1997), structural data and geomorphological evidence (*Cobbold and Rossello*, 2003; *Folguera et al.*, 2004; *Galland et al.*, 2007; *Messager et al.*, 2010). In addition to the E-W compression, the Southern Andes are characterised by a strike-slip regime with N-S tension, resulting from the east-directed shear on the southern plate boundary (*Meijer et al.*, 1997).

The Neuquén Basin

The Neuquén Basin is located in NW Patagonia, on the eastern foreland of the Andean Cordillera. It lies in Argentina and Central Chile between 32°S and 40°S latitude and covers a roughly triangular area of 160 000 km^2 (*Cobbold and Rossello*, 2003). It is bound by the Sierra la Pintada to the North, the Patagonian Massif to the South and the Andean volcanic arc to the West. Two major structural domains are distinguished: the deformed Andean Sector and the submerged Neuquén Embayment (Figure 10).

The evolution of the Neuquén Basin is strongly linked to the evolution of the Andes. Various stages of extension and compression represent different stages of the evolution of the mountain chain. Therefore, it is essential to consider the evolution of the Neuquén Basin in the regional framework of the Andes. The Neuquén Basin first formed as a rift basin during Early Mesozoic extension which resulted from slow subduction of oceanic crust beneath the South American margin (*Cobbold and Rossello*, 2003).

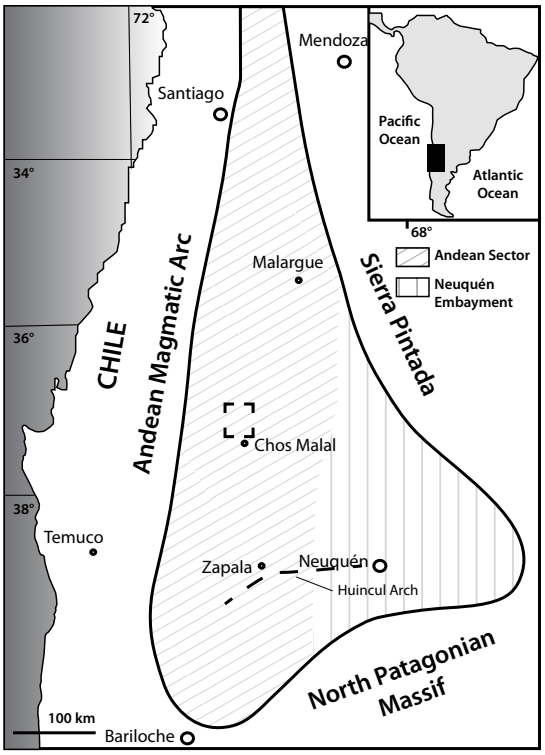

Figure 10: *Simplified map of the Neuquén basin showing the field area. Modified from Howell et al. (2005).*

The basement of the Neuquén Basin consists of igneous and volcaniclastic rocks of the Choiyoi Formation of Permo-Triassic age. The overlying basin fill with a thickness of over 5 km comprises a continuous succession of Late Triassic to Early Cenozoic fossiliferous marine and continental sediments, overlain by a thin Recent cover (Figure 11).

In the Late Triassic to Early Jurassic, synrift sediments were deposited during an extensional phase that records the onset of the breakup of Gondwana (*Franzese and Spalletti*, 2001). Postrift subsidence is marked by marine Jurassic to Early Cretaceous sediments, whereas conditions became progressively continental in the Late Cretaceous. The Cenozoic comprises continental sediments and volcanic rocks, as well as high-level intrusions.

The sedimentary sequences thin towards the northeastern and southeastern edges of the basin (*Cobbold et al.*, 1999). In contrast, the western edge of the basin has been uplifted and forms the present day foothills, as a result of the Andean Orogeny. This exhumation of the basin fill in the Cenozoic together with a dry climate has resulted in excellent outcrops of Late Triassic to Late Cretaceous strata. Due to these outcrop conditions and abundant fossils, the Early Mesozoic structural styles and sedimentary environments of the Neuquén Basin are well constrained. In contrast, due to sparse outcrops of younger strata, the Cenozoic history of the Neuquén Basin

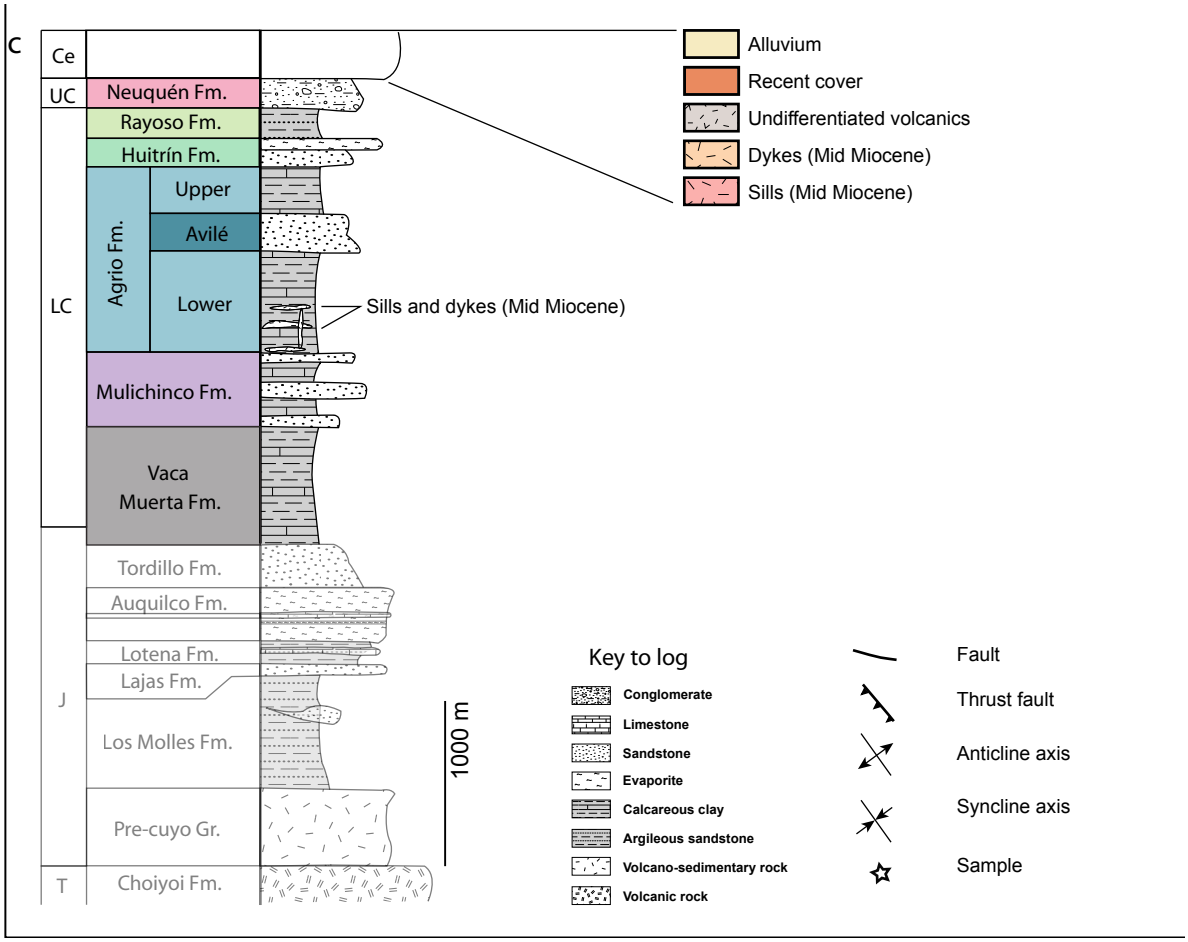

Figure 11: *Stratigraphic column of the study area and map legend. Transparent stratigraphic units do not crop out in the study area, but are mentioned in the geological overview. Stratigraphic column also serves as key to the geological and structural maps presented in the results section (Figures 20a,b, 21a-d). Modified from Galland et al. (2003).*

is not well constrained. Cenozoic volcanic rocks and high-level intrusions are common in the Andean Cordillera, but less so in the foothills. Age determinations are widely lacking (*Cobbold et al.*, 1999).

In summary, the alternating changes in tectonic style at the western margin of Gondwana have led to three stages of basin formation. In the Late Triassic to Early Jurassic, prior to the onset of subduction, extensional tectonics gave rise to a series of narrow, isolated depocentres (*Howell et al.*, 2005). The development of a steeply dipping subduction zone and associated magmatic arc along the western margin of Gondwana led to back-arc subsidence in the Neuquén Basin in the Early Jurassic to Early Cretaceous. The basin was subsequently filled in a post-rift stage. In the Late Cretaceous to Cenozoic, the shallowing of the subduction zone led to compression and flexural subsidence with associated crustal shortening and the uplift of the foreland thrust belt (*Howell et al.*, 2005).

Stratigraphy of the Neuquén Basin

The deposition of a thick and virtually continuous Jurassic to Early Cretaceous sedimentary succession (Figure 11) with abundant fossils makes the Neuquén Basin an excellent field laboratory for sequence stratigraphy and basin evolution. For the purpose of this study, it is very useful to have a complete picture of the evolution of the basin and its structural styles.

Jurassic sedimentation

Early Jurassic strata were deposited during a phase of rifting resulting from the break-up of Gondwana that began in the Late Triassic. The Pre-Cuyo Group is an early-rift sequence of continental molasse, volcanic and volcaniclastic deposits that marks the onset of rifting and is truncated by a regional unconformity (*Cobbold et al.*, 1999). The marine deposits of the Cuyo-Group were accumulated during the late synrift to post-rift phase (*Legarreta and Uliana*, 1996). Marine transgression from the Pacific due to thermal subsidence together with eustatic sea level rise deposited the organic-rich, dark mudstone of the Los Molles Formation of marine or lacustrine-saline origin (*Cobbold et al.*, 1999). The Lotena Formation comprises marine and continental clastic deposits of detrital origin, as well as carbonates of the La Manga Member (*Vergani et al.*, 1995). Jurassic sediments are not exposed in the study area, but have been recognised in outcrops in surrounding areas in the West.

Early Cretaceous sedimentation

The Early Cretaceous sedimentation in the Neuquén Basin comprises the Mendoza Group, the lower part of which is a marine mega-sequence, dominated by the Vaca Muerta Formation (*Weaver*, 1931). It consists of dark, bituminous shales interbedded with well-laminated limestones (Figure 12).

The marine shales result from low-energy sedimentation of poorly oxygenated, organic-rich deposits in a basin interior setting. The presence of calcareous layers suggests sea level fluctuations. According to *Leanza* (2001) the vertebrate and invertebrate fossil content indicates marine conditions with warm temperate waters.

Outcrops of this formation were mapped in a topographic low in the central southern sector of the study area, in the core of an anticlinal structure and represent the stratigraphically lowest outcropping unit. The thickness of the Vaca Muerta Formation is 650 m and has been traversed by the Tricao Malal well x-1 (*Guerello*,

Figure 12: *Road cut through dark bituminous shales of the Vaca Muerta Formation, the main source rock for hydrocarbons in the Neuquén Basin.*

2006). The Vaca Muerta Formation is the primary hydrocarbon source rock in the Neuquén Basin (*Urien*, 1994).

Subsequently, a relative sea level fall deposited the fluvial to marine clastics of the Mulichinco Formation (*Schwarz and Howell*, 2005). This unit comprises grey-green to brown, fine-grained sandstones and calcareous sandstones with abundant marine and non-marine fossils. The depositional setting is variable, ranging from fluvial braid plains to outer-shelf marine (*Schwarz and Howell*, 2005). The thickness of this formation in the study area is approximately 100 m. The Mulichinco Formation mostly crops out as a bivalve-rich thick coquina. Occasionally metre scale banked beds were observed. Outcrops of this unit are limited to the southern part of the study area, where they are found in the eroded cores of anticlines. The top of the formation is associated with a transgressive phase that resulted in the deposition of the dark shales of the overlying Agrio Formation (*Schwarz and Howell*, 2005).

The Agrio Formation (*Weaver*, 1931) crops out over big parts of the study area (Figure 13). It is subdivided into the Lower Agrio, Avilé and Upper Agrio Members. *Leanza* (2001) proposed an alternative nomenclature: the Pilmatué, Avilé and Agua de la Mula Members. The lowest subunit consists of grey shales with intercalated limestones of marine origin, followed by the medium-grained sandstones of the Avilé Member deposited under shallow marine conditions. Planar and cross-stratified layers are common. Furthermore, some layers comprise abundant mudstone intraclasts. The thickness of the Avilé sandstone varies between 25 m and 75 m, and reaches up to 150 m in thickness in the northeastern part of the study area. It is followed by the Upper Agrio or Agua de Mula shales of marine origin. This subunit of the Agrio Formation is approximately 250-300 m in thickness. The alternation between dark shales intercalated with limestones and calcareous sandstones suggests variations in relative sea level. The fossil assemblage indicates shallow marine, temperate conditions in an offshore environment (*Leanza*, 2001). Overall, the Agrio Formation has resulted from periodic tectonic activity and eustasy marked by multiple transgressive-regressive sequences (*Cob-*

Figure 13: *Road section through the Agrio Formation consisting of grey shales and limestones and prominent Avilé sandstones.*

bold et al., 1999; *Veiga et al.*, 2005). Throughout the study area, the Agrio unit is folded into tight anticlines and synclines.

The Agrio Formation is followed by the Huitrín Group, which is divided into two members. The basal Troncoso Member of the Huitrín Group comprises fluvial and aeolian sandstones (approximately 80 m in thickness). Individual banks are several metres in thickness and comprised of medium-grained grey to pale green sandstone, locally interbedded with dark grey to green pelites. Ripple structures have been observed, suggesting a fluvial depositional environment. The basal Troncoso Member is followed by the yellow to light brown evaporites of the top Troncoso Member that mark hypersaline conditions arising from a restricted connection with the Pacific and subsequent transition to continental conditions. These deposits are only sparsely preserved and act as regional detachment horizons. Overall, the transition from fluvial sandstones that were deposited by braided river systems to aeolian deposits reflecting an arid environment, suggests an upward-drying system (*Strömbäck et al.*, 2005). Outcrops of this unit are found in an anticlinal structure along the eastern border and in several synclines along the western border of the field area.

The Rayoso Formation (*Uliana et al.*, 1995) consists of basal evaporites intercalated with parallel laminated red mudstone that become more prominent towards the top. The transition between the Upper Troncoso Member and the basal Rayoso Formation is not well marked, as both result from hypersaline marine environments. Progradation to continental conditions is marked by the muddy, red fluvial deposits of the Upper Rayoso Formation. This formation was only mapped to the East of Cerro Colorado, along Ruta Provincial 2 on the way to Tricao Malal and in an anticline in the central north of the study area.

Late Cretaceous sedimentation

In the Late Cretaceous, renewed uplift and erosion resulted in a regional unconformity. During this time all connections to the Pacific Ocean were cut off and depositional conditions became fully continental. Exhumation led to the deposition of large amounts of coarse-grained clastic material of the Neuquén Formation. The prominent redbeds of the Neuquén Formation discordantly overlie the Early Cretaceous deposits (*Cobbold et al.*, 1999). These redbeds represent the stratigraphically youngest sediments in the study area and are abundant at the eastern margin of the field area, where they are unconformably overlain by lava flows from Tromen volcano.

Cenozoic deposits

Cenozoic sediments are scarce in the Neuquén Basin. However, high-level andesitic intrusions pierce through the deformed Mesozoic sediments at several localities in the fold-and-thrust belt (*Cobbold et al.*, 1999; *Cobbold and Rossello*, 2003). These intrusions are the main subject of this study and will be described in detail in the following sections. Lavas of mostly andesitic composition and associated pyroclastic deposits unconformably overlie the intrusions (*Cobbold and Rossello*, 2003). In general, absolute age constraints for many of these magmatic units are insufficient or missing.

Regional tectonic structures

The previously described Mesozoic and Cenozoic sedimentary sequence crops out over a wide area and has been folded and faulted since the Middle Cretaceous (*Windhausen*, 1914; *Keidel*, 1925; *Groeber*, 1929; *Wichmann*, 1934) to be uplifted and exhumed by several kilometres in the foothills of the Andes (*Cobbold and Rossello*, 2003). In the following section, the most important tectonic structures will be described (Figure 14).

Cortaderas fault system

A linear structure that trends E-SE across the foothills was first described by *Groeber* (1929). The Cortaderas fault system (also Cortaderas Lineament) (*Ramos and Rolleri*, 1978; *Ramos*, 1981; *Ramos and Barbieri*, 1989) represents the boundary that separates the Chos Malal fold-and-thrust belt to the North from the Agrio fold-and-thrust

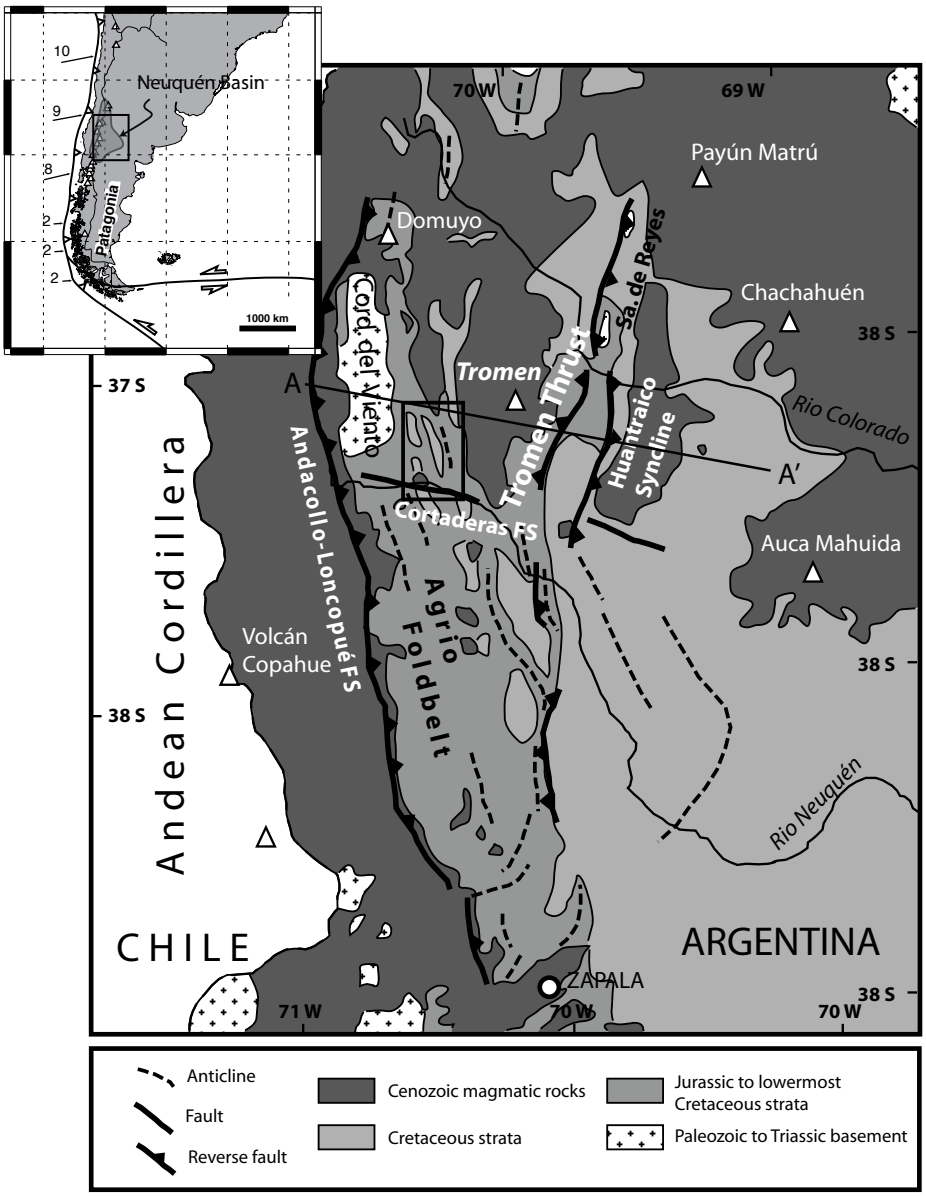

Figure 14: *Simplified geological map of the Neuquén Basin, NW Neuquén Province. Map illustrates main sedimentary and magmatic units, main volcanoes (white triangles) and tectonic structures. FS denotes fault system. The location of a crustal scale cross-section (W-E; Figure 15) is indicated. Box indicates study area around Cerro Negro. Inset shows large-scale tectonic setting, current velocity vectors for Nazca Plate relative to South America (numbers in cm/yr). Modified from Cobbold and Rossello (2003); Galland et al. (2003).*

belt to the South which display distinctive evolutionary characteristics (*Ramos and Kay*, 2006).

This structural feature can be traced to the Southern Volcanic arc front and was interpreted as a basement boundary that was activated during Andean deformation (*Ramos*, 1981). *Cobbold and Rosello* (2003) consider this prominent structure to be a N-NE verging thrust fault with an anticline in its hanging wall and volcaniclastic growth strata in its footwall. Based on field observations the authors have concluded that the thrust was active between the late Late Palaeocene and Early Miocene.

It has been pointed out that Cenozoic (Miocene to Holocene) magmatism is concentrated north of the Cortaderas fault system, whereas it is near absent in the South (*Ramos and Barbieri*, 1989). Furthermore, it has been attributed to be the southern limit of a Miocene shallow subduction zone (e.g. *Kay*, 2006). *Ramos and Kay,* (2006) provide a detailed description of the major geologic features of the regions north and south of the Cortaderas fault system.

Agrio fold-and-thrust belt

The Agrio fold-and-thrust belt (*Ramos and Rolleri*, 1978) is approximately 50 km wide and contains Jurassic to Early Cretaceous sedimentary rocks. These are folded into mostly upright and tight anticlines, and wide and flat synclines. The observation of such bimodal trend and the upright geometry of the anticlines suggests that strike-slip displacement parallel to the orogen may have played an important role during the development of this belt. The variable fold wavelengths have been attributed to competition of thin-skinned and thick-skinned processes. Thin-skinned tectonics are due to the detachment of evaporite or shale (Huitrín and Rayoso Formations), whereas thick-skinned tectonics caused the reactivation of Mesozoic normal faults (*Cobbold and Rossello*, 2003).

With the exception of Late Eocene andesitic lavas (located near Collipilli), younger folded rocks are relatively rare in this belt. Several shallow magmatic intrusions of Middle to Late Eocene age and bitumen dykes have been described in the region (*Cobbold and Rossello*, 2003). Furthermore, a shallow magmatic system of Middle Mi-

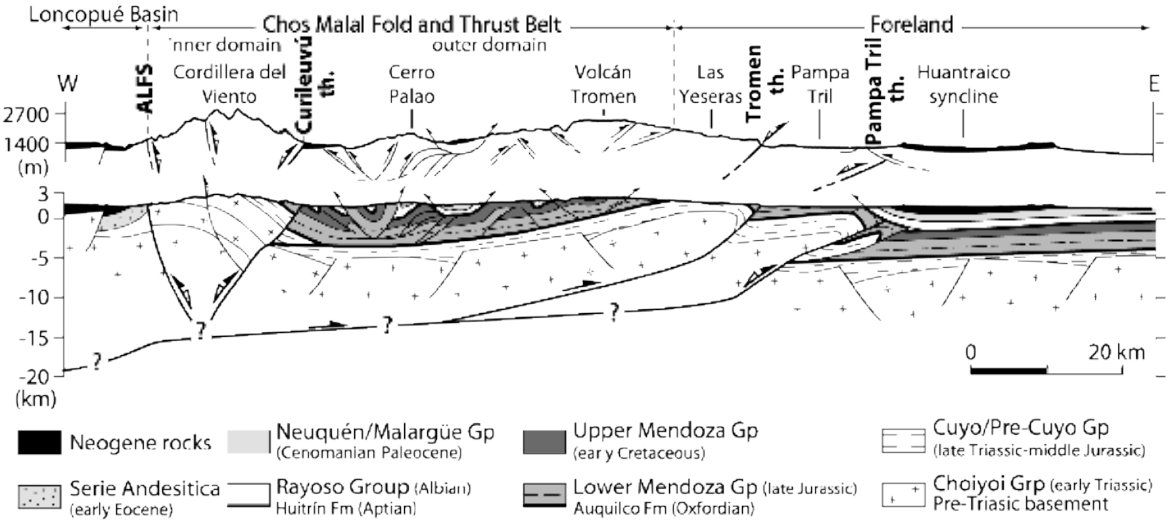

Figure 15: *East-west structural cross-section across the Chos Malal fold-and-thrust belt (at 37°15'S) (after Vergani et al., 1995; Kozlowski et al., 1996; Cobbold et al., 1999; Zamora Valcarce et al., 2006b; Folguera et al., 2007a). The location of the cross-section is marked in the previous figure. ALFS, Andacollo-Loncopué Fault System; th., thrust; Gp., Group; Fm, Formation. The extent of crustal features at depth remains unknown. For reasons of simplicity a basal detachment at the limit upper/lower crust is presented. From Messager et al. (2010).*

ocene age has been recognised at Cerro Negro (*Kay*, 2006).

For the purpose of this study, we do not distinguish between the Agrio fold-and-thrust belt and its northern continuation, the Chos Malal fold-and-thrust belt (*Bracaccini*, 1970), bound by the Cordillera del Viento in the West. Figure 15 illustrates the structural relationships at the southern limit of the Cordillera del Viento, which is not developed further south than 37°15'S.

The east-verging Rio Curí Leuvú thrust marks the eastern edge of the Cordillera del Viento, where it offsets Mesozoic sediments. *Folguera et al.*, (2007a) suggest that, at least in the northern part of the Cordillera del Viento, pronounced uplift after 15 Ma is related to the activity of this thrust.

Tromen Thrust

The Tromen Thrust is a prominent structure north of the Cortaderas Lineament. It is located 50 km east of the study area, where extends over 70 km (*Bracaccini*, 1970; *Kozlowski et al.*, 1996). It is characterised by an arcuate trace along the eastern flank of the Tromen volcanic edifice, where Jurassic evaporates are exposed in a large overturned hanging-wall anticline (*Cobbold and Rossello*, 2003). The arcuate trace has been attributed to growth under the weight of the volcano (*Marques and Cobbold*, 2002; *Galland et al.*, 2007). As inferred from seismic profiles, the Tromen Thrust involves basement rock (*Kozlowski et al.*, 1996), and has been interpreted to be a reactivated Jurassic normal fault that is still active today (*Cobbold and Rossello*, 2003).

Huantraico Syncline

The Huantraico Syncline lies north of the Cortaderas Lineament and is an important regional structure, as it records Early Miocene compression in a back-arc setting. Folding affects lavas of Late Eocene (*Ramos and Barbieri*, 1989) to Early Miocene (*Cobbold and Rossello*, 2003) age. According to *Kozlowski et al.* (1996) folding postdates lavas with ages of 16.3±0.1 Ma (Ar-Ar), but predates others with ages of 6.7±0.5 Ma. Similar age constraints are reported by *Ramos and Barbieri* (1989). More recently, *Kay and Copeland* (2006) revisited the locality and provided additional data that does not change the youngest age for compressional deformation.

Timing and style of regional deformation

The tectonic history of the Neuquén Andes has comprised recurrent periods of compression and extension, resulting in complex patterns in the foothills of the Neuquén Andes, where abundant folds and thrusts shape the landscape. The timing of deformation in the Neuquén Basin is revealed by unconformities, variations in sediment thickness and intrusive relationships. During Andean deformation pre-existing normal faults from the rift phase that were activated as back thrusts and the rock mechanics of the basin fill controlled the style of deformation (*Vergani et al.*, 1995; *Kozlowski et al.*, 1996). The evaporites of the Rayoso and Huitrín Formations acted as major detachment horizons (Figures 15, 16; *Vergani et al.*, 1995). Pioneering geologists (*Windhausen*, 1914; *Keidel*, 1925; *Groeber*, 1929; *Wichmann*, 1934) described the abundant folds and thrusts in the foothills of the Neuquén Basin and attributed them to different phases of compressional tectonic deformation. These are the three phases of Andean deformation based on the work of *Steinmann* (1929) in the Peruvian Andes. For the Northern Neuquén Basin, these have been examined in detail and linked to tectonic structures by *Cobbold and Rosello* (2003) as follows:

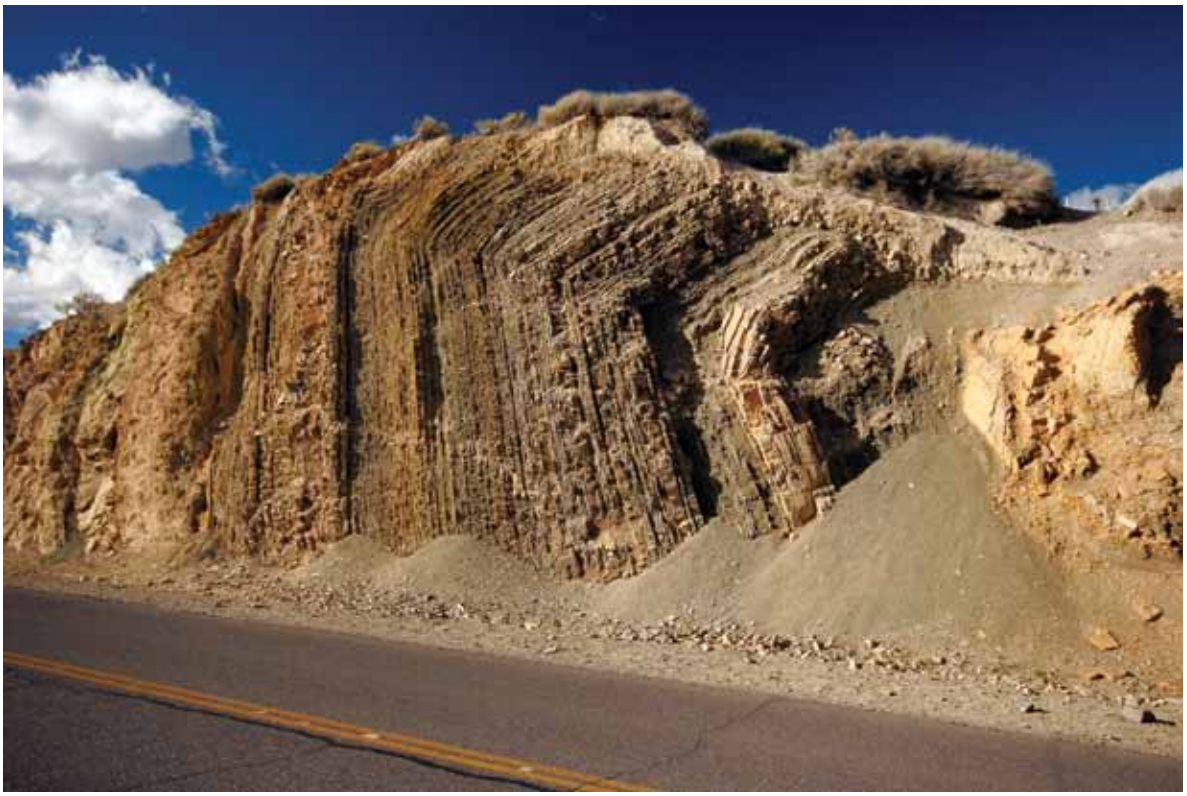

Figure 16: *Backthrust anticline in the Huitrín Formation that acts as a regional detachment horizon in the northern Neuquén Basin.*

1. The Peruvian phase (Middle to Late Cretaceous) was contemporaneous with the opening of the South Atlantic. An increased convergence rate and shallowing of the Benioff Zone (*Pardo-Casas and Molnar*, 1987) was responsible for E-W shortening, resulting thrusts, transpressional reactivation of a rift transfer zone (e.g. the Huincul Arch), regional unconformities (e.g. between the Agrio and Huitrín Formations), and the development of a widespread retro-arc foreland basin containing more than 2500 m of mainly continental sedimentary rocks.

2. The Incaic phase (Eocene) was responsible for SE trending folds and thrusts, reactivation of previous structures, abundant andesitic lavas and high-level intrusions, and a swarm of NE trending bitumen dykes. Rapid, oblique convergence at the Pacific margin led to right-lateral displacements parallel to the orogen and strike-slip faulting. These observations led *Cobbold and Rosello* (2003) to the conclusion that there has been an important Eocene transpression, representing the main phase of deformation in the foothills of the Neuquén Basin. This contrasts the work of several authors that have suggested that the Incaic phase was followed by a period of extensional tectonics (Oligocene to Early Miocene) (*Jordan et al.*, 2001; *Folguera et al.*, 2002). In recent years, additional regional evidence for such extension was provided (*Zapata et al.*, 2005; *Burns et al.*, 2006; *Folguera et al.*, 2010).

3. The Quechua phase (Miocene to Recent), during which convergence was rapid and more frontal, produced northerly trending folds and thrusts, the Loncopué hinterland basin, and the Miocene Huantraico Basin, which contains some 1000 m of basaltic lava flows.

The recent tectonic history of the Neuquén Andes is particularly debated. As Neogene to Recent deposits are rare, it is not clear how long compressional deformation lasted. Thus, the Recent tectonic history of the Neuquén Basin is not

well constrained and a topic of a long-standing debate. Based on observations in the Cordillera del Viento (*Kozlowski et al.*, 1996) and Cerro Negro (*Kay*, 2006), *Folguera et al.* (2007a) come to the conclusion that the "youngest compressive pulse of deformation at the easternmost part of the Andes is given by the undeformed Cerro Negro volcanics, east of Cordillera del Viento, dated at 11.7 ± 0.2 Ma (*Kay*, 2006)".

Folguera et al. (2006) have also previously suggested that compressional deformation stopped during the Early Pliocene, and that active tectonics are extensional. On the contrary, in situ stress measurements (*Guzmán et al.*, 2007), GPS (Global Positioning System) measurements (*Klotz et al.*, 2001), earthquake focal mechanisms (*Chiu*, 1992; *Assumpção and Araujo*, 1993; *Meijer et al.*, 1997), structural data, and geomorphological evidence (*Cobbold and Rossello*, 2003; *Folguera et al.*, 2004; *Galland et al.*, 2007; *Messager et al.*, 2010) indicate current horizontal compression. Amongst others, *Messager et al.* (2010) have provided evidence that the extensional features in the study area correspond mainly to thin-skinned gravitational gliding, resulting from crustal uplift. Thus, they argue that the tectonic compressive regime is preserved in the southern Neuquén Basin throughout the Plio-Quaternary, though the slab may have been steepening since 4 Ma. Additionally, they point out that statistical analysis of subduction zone dynamics indicate that slab steepening does not necessarily trigger an extensional state of stress in the overriding plate (*Heuret and Lallemand*, 2005; *Lallemand et al.*, 2005; *Heuret et al.*, 2007; *Schellart et al.*, 2007; *Schellart et al.*, 2008).

These studies complement the interpretations of *Galland et al.* (2007), suggesting that tension fractures result from the growth of compressive structures, whereas the deeper stress field remains compressive. These findings are not compatible with the extensional state of stress invoked by other workers (*Folguera et al.*, 2004; *Ramos and Folguera*, 2005; *Folguera et al.*, 2006; *Ramos and Kay*, 2006; *Folguera et al.*, 2007b; *Folguera et al.*, 2008). As a consequence, the timing and style of Tertiary deformation in the Neuquén Basin is still debated.

Overview over the Cenozoic magmatic history of the Neuquén Basin (between 36°S-38°S)

Magmatic activity has been evident in the southern and south-central Andes since the Mesozoic, when rifting related to the breakup of South America and Africa occurred (*Kay and Copeland*, 2006). For the purpose of this study, only the Cenozoic back-arc magmatism in this region is described, as geochronological and geochemical data from these magmatic rocks are crucial to establish the age of uplift and timing of deformation in this region. Subsequent changes in the position of the volcanic arc front and chemistry during the last 25 m.y. have been attributed to variations in the steepness of the Wadati-Benioff zone (e.g. *Ramos and Folguera*, 2005). Furthermore, the Cortaderas Lineament has been suggested to represent an important structural feature that separates diverse suites of Miocene to Holocene back-arc magmatic rocks. These are widespread in a retro-arc region south of the Cortaderas Lineament, where contractional deformation has played a key role. North of the Cortaderas Lineament magmas of this age are nearly absent (Figure 17; *Kay*, 2005; *Kay*, 2006; *Kay and Copeland*, 2006).

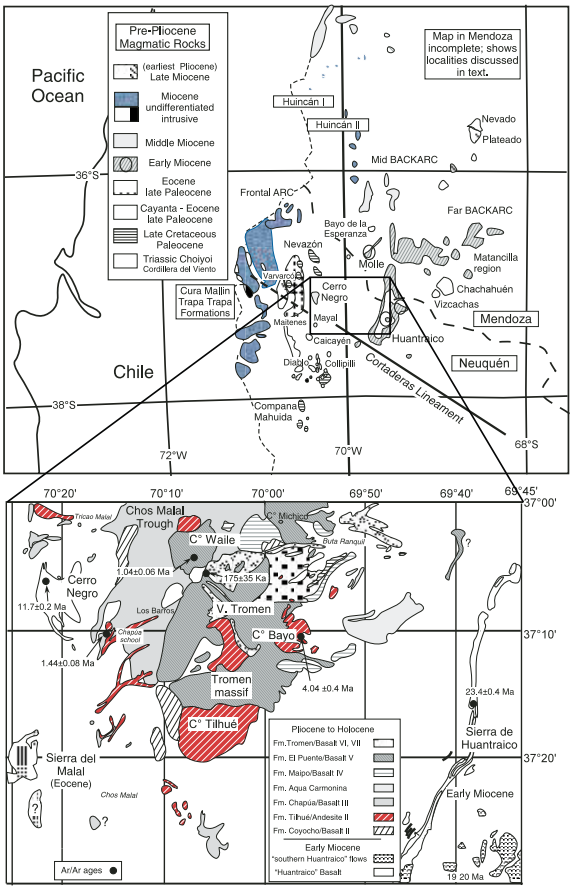

Figure 17: *Maps of pre-Pliocene (top) and Tertiary to Holocene magmatic rocks (bottom) in the Neuquén Region (modified from Kay et al. (2006). The Cortaderas Lineament is marked according to Ramos (1978).*

Tertiary magmatism between 36°S-38°S began with the eruption of Paleocene to Eocene magmas with strong arc-chemical affinities in the near frontal arc region (*Kay*, 2005). A series of shallow level intrusions were emplaced in the previously deformed strata of the Agrio fold-and-thrust belt in Middle Eocene times (*Cobbold and Rossello*, 2003), when the arc front moved east of the Cordillera del Viento (*Kay*, 2005). This was followed by a quiescence in magmatic activity until the initiation of mafic to felsic volcanism with an arc signature in the intra-arc region (ca. 26-20 Ma), and alkali olivine basalts with intraplate chemistry across the back-arc (ca. 20-24 Ma) (*Kay*, 2005).

In the Oligocene and Miocene, the magmatic arc migrated towards the East (*Vergara and Munizaga*, 1974). North of the Cortaderas Lineament, magmatism with an arc geochemical signature was evident as far as 500 km east of the trench, but became inactive with increasing distance from the modern trench (e.g. *Kay*, 2005; *Kay and Copeland*, 2006).

This activity accounted for the roughly 1000 m thick basaltic lava flows that were gently folded in the Huantraico syncline (*Ramos and Barbieri*, 1989; *Kay and Copeland*, 2006).

After about 20 m.y. the situation changed when basaltic andesites to dacites with weak arc signatures erupted in the mid back-arc. The Cerro Negro andesites (ca. 11.7 Ma) from the near back-arc display a stronger arc signature (*Kay*, 2005) and become more important in the Chachahuén volcano (ca. 7.6-4.8 Ma) (*Kay*, 2006). These changes in geochemistry have been interpreted to coincide with steep subduction between 25 and 15 Ma and shallowing in the Late Miocene (e.g. *Ramos and Folguera*, 2005).

Subsequently, the magmatic arc returned to its present day location in the Main Cordillera (*Jordan et al.*, 2001). During the last 5 m.y., the angle of the Wadati-Benioff Zone may have steepened again leading to a wide zone of deformation and retro-arc volcanism (e.g. *Ramos and Folguera*, 2005). In the Pliocene to Holocene magmatism close to the modern volcanic front was characterised by an arc-geochemical signature (*Vergara and Munizaga*, 1974; *Hickey et al.*, 1986; *Folguera et al.*, 2002). East of the main arc, volcanoes like Auca Mahuida, Payun Matru and Tromen, have back-arc (intraplate-like) geochemical signatures (*Saal et al.*, 1993; *Kay*, 2006; *Galland et al.*, 2007).

In summary, there has been pronounced back-arc volcanism in the Early Miocene, but nearly no magmatism in the Middle to Late Miocene, with the exception of Cerro Negro (ca. 11.7 Ma), which is characterised by an arc signature. Subsequently, back-arc magmatic activity increased again in the Pliocene-Holocene. This poses the question: why is there a gap in magmatic activity before and after the activity of Cerro Negro 11.7 m.y. ago? Based on regional geochemical data the hypothesis of transient shallowing of the Andean subduction zone in the Miocene has been proposed (Figure 18; *Kay*, 2005; *Kay*, 2006; *Kay and Copeland*, 2006).

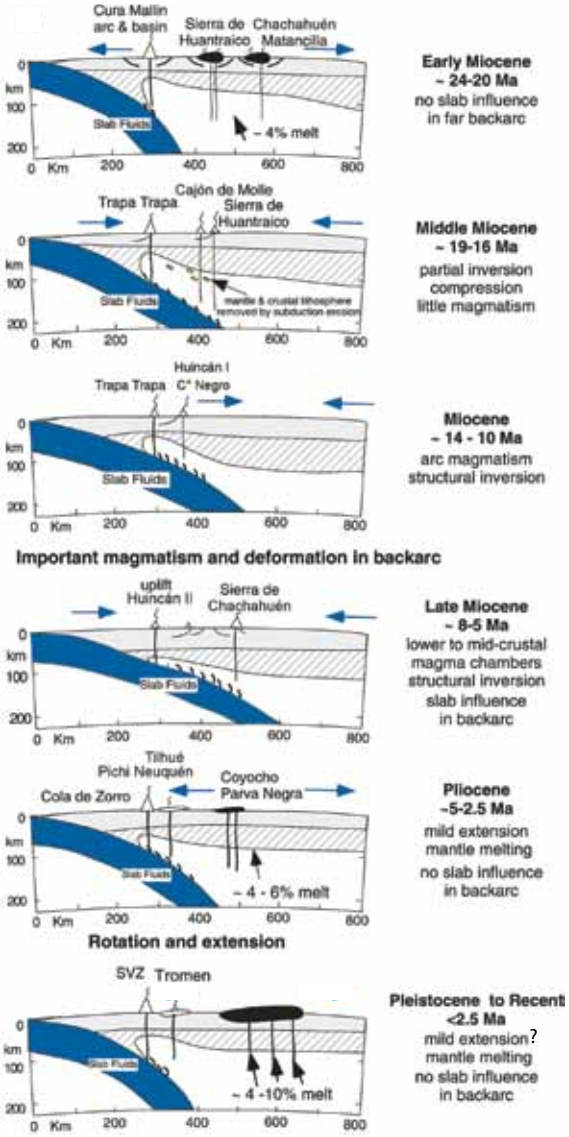

Figure 18: *Lithospheric scale cross-section illustrating Miocene to Holocene magmatism across the Neuquén Basin near 37°S. The model accounts for changes in slab steepness, magma sources and deformation. Magmatic centres with arc or back-arc geochemical signatures are white, those with intraplate-signatures are black. Modified from Kay et al. (2006).*

Case study: Cerro Negro intrusive complex, Neuquén Province, Argentina

This study focuses on a roughly 250 km^2 large area between 37°02' - 37°24' S and 70°38'W - 70°24'W. The study area is located in the Agrio fold-and-thrust belt in the northwestern part of the Neuquén Basin, approximately 40 km north of the town of Chos Malal and 80 km east of the Main Cordillera (Figure 19). The fold-and-thrust belt has resulted from intense E-W shortening, and contains tight folds and thrusts, trending N-S. It is bordered by the Cordillera del Viento to the West and Tromen volcano to the East (*Kozlowski et al.*, 1996). The study area comprises a continuous succession of Early Cretaceous to Late Cretaceous sedimentary rocks, locally pierced by Miocene intrusions and partly overlain by Tertiary volcanic rocks. The Cerro Negro intrusive complex belongs to a magmatic province that intruded into the intensely deformed Agrio fold-and-thrust belt and crops out as a network of sills and dykes around a main intrusion.

We chose the Cerro Negro and surrounding area as they lie in a fold-and-thrust belt with well-known stratigraphy. Furthermore, the magmatic system is well exposed. It has previously been mapped by (*Zöllner and Amos*, 1973) and recently studied by (*Kay*, 2005; *Kay and Copeland*, 2006) in a regional context with emphasis on its geochemical characteristics. Furthermore, Cerro Negro (dated at 11.07±0.2 Ma, *Kay*, (2005)) has been numerously considered to be effusive in origin and postdate the youngest pulse of compressive deformation at the easternmost part of the Neuquén Andes (*Kay and Copeland*, 2006; *Folguera et al.*, 2007a). Studies focusing on the overall structure of the magmatic system and integrating these with geochronology and geochemistry have not previously addressed the case of Cerro Negro.

Figure 19: *Location of the study area in the foothills of the Andes, Northern Patagonia, Argentina. The state border between Argentina and Chile is indicated. East of the study area lies Tromen volcano (3978 m).*

Thus, the Cerro Negro of Tricao Malal, a basaltic to andesitic high-level intrusion piercing through pre-existing folds, provides a good natural laboratory to study the link between tectonics and volcanism.

From the town of Chos Malal, access to the field area is possible along the eastern and western border. From the East access is via the Ruta Nacional 40 towards the Mendoza Province and then a turn onto a gravel road (Ruta Provincial 2) towards the village of Tricao Malal. From the West, access is possible along Ruta Provincial 43, and turn onto Ruta Provincial 41 towards the village of Los Menucos, along the riverbed of Rio Curí Leuvú. Mobility within the field area is limited to a few unsealed paths that are accessible with a four-wheel drive. The central part of the study area was mainly surveyed by foot and on horse. Animal paths, seismic lines and dry riverbeds provided good orientation.

Methods

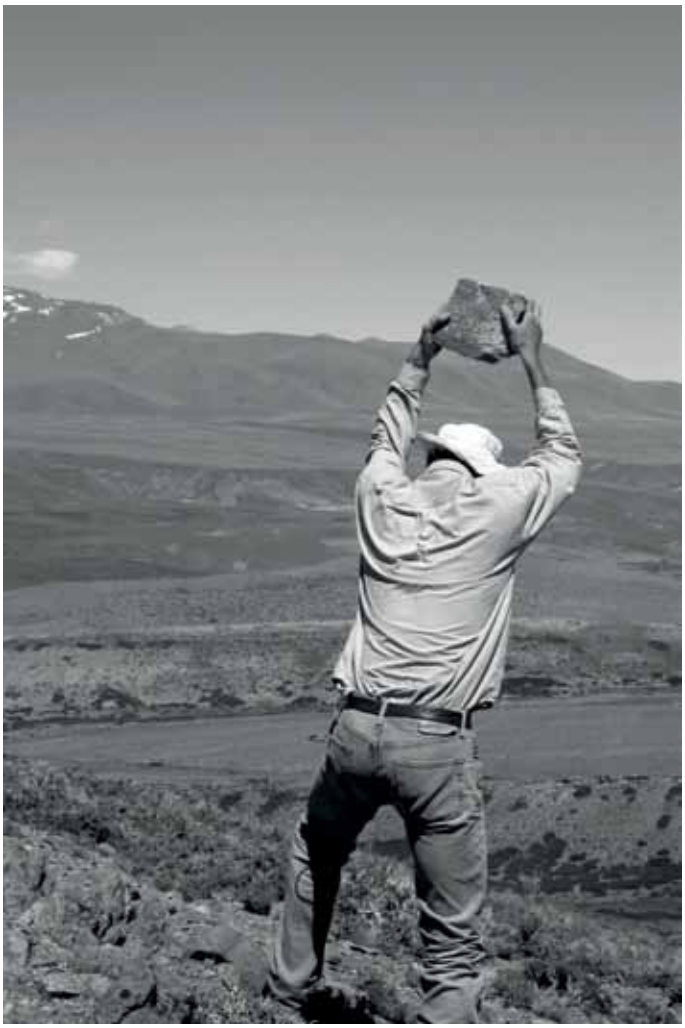

Structural mapping and sample selection

Fieldwork was prepared by compiling existing literature, geological maps and satellite imagery (*Zöllner and Amos*, 1973; *Delpino and Deza*, 1995; *Leanza*, unpublished). It should be noted that there are several regional scale studies of the area, mostly in Spanish, but detailed interdisciplinary literature is scarce. GoogleEarth Pro satellite images were used as the basis for field mapping. Structural mapping and sampling around the Cerro Negro south of Tricao Malal was performed between November and December 2011.

In total 42 samples were taken from dykes and sills of the Cerro Negro Complex. The selection was based on field relationships and grade of alteration. Thin alteration rims were removed in the field. The samples with the lowest grade of alteration, all 2-4 kg in weight, were used for subsequent analyses.

Sample preparation

Samples were cut into separate blocks for thin section preparation, dating and geochemical analyses with a diamond saw at the Department of Geosciences, University of Oslo. To avoid contamination from saw splits, the samples were washed and dried. Thin sections of all samples were prepared at the University of Würzburg, Germany. Based on thin section and SEM (scanning electron microscope) observations, 5 samples that were most likely to yield zircon grains were chosen for dating. Based on thin section observations, the least altered 15 samples were chosen for geochemical analyses.

Geochronology

Zircon is one of the most widely used and reliable geochronometres based on the decay of U (and Th) to Pb. It is present as accessory phase in a wide range of rocks and is not as easily affected by magmatic, metamorphic and erosional processes as other common minerals. As a result, zircon grains commonly consist of distinct segments, each recording a particular period in their history (*Corfu et al.*, 2003). Furthermore, zircon contains U concentrations exceeding that of its host rock. At the same time, it discriminates against its daughter element Pb during crystallisation (e.g. *Davis et al.*, 2003). Several processes may affect U-Pb ages: Pb loss due to radiation damage, U-Pb resetting by recrystallisation, assimilation and inheritance. These processes may complicate the interpretation of geochronological data, but may also provide additional information, such as the time of metamorphic overprints (*Corfu et al.*, 2003). The impact of Pb loss can be minimised by selecting the most appropriate grains (clear, euhedral) and abrading their rims. Geological complications are commonly revealed by (in-)consistency of repeated analyses. Besides the geological factors affecting the accuracy of obtained U-Pb ages of zircons, the calibration of the U-Pb tracer is a crucial factor. It can be calibrated against known solutions and then checked by measuring well-characterised reference solutions or zircons (*Mazzini et al.*, 2010; *Condon and Bowring*, 2011).

Geochronological data were collected from several zircon populations using U-Pb dating applying isotope dilution thermal ionisation mass spectrometry (ID-TIMS), following a modified procedure of

Krogh (1973); *Corfu* (2004); *Schoene et al.* (2010). The texture of zircons in selected samples was studied with a scanning electron microscope.

Five samples (CN-11-01, CN-11-03, CN-11-13, CN-11-14, and CN-11-20) were chosen for dating based on geological criteria, and on thin section and SEM observations. These were crushed using a steel jaw crusher, followed by milling to < 250 µm with a steel cross beater mill. Zircons were then separated by a combination of Wilfley board washing, magnetic and heavy liquid (Diiodomethane) separation, followed by hand picking from the least magnetic heavy fraction under a binocular microscope. The clearest and most euhedral zircon grains were grouped into fractions or selected as single grains, based on their appearance. In order to remove external disturbed domains (*Davis et al.*, 1982), chemical abrasion of zircon grains by combined annealing and multi-step partial dissolution was performed according to the "CA-TIMS" technique (*Mattinson*, 2005; 2010).

Selected grains were washed using HNO_3, H_2O and $(CH_3)_2CO$, weighed on a microbalance and spiked with a $^{202}Pb/^{205}Pb/^{235}U$ tracer. Subsequently, all zircon fractions were dissolved with HF and HNO_3 in Teflon bombs and underwent chemical separation with anion exchange resin (*Krogh*, 1973; *Corfu*, 2004).

The samples were loaded on outgassed Re filaments together with Si-gel and H_3PO_4. Subsequently, they were measured with a MAT262 mass spectrometer either on Faraday cups in static mode, or, for low signals and all $^{207}Pb/^{204}Pb$ ratios, in peak jumping mode using an ion counting secondary electron multiplier. The obtained data were corrected with fractionation factors of 0.1%/amu for Pb and 0.12%/amu for U. The blank correction was 0.1 pg U and 2 pg Pb, or less when the total common Pb was below that level. The initial Pb was corrected with the model of *Stacey and Kramers* (1975). Furthermore, all data were corrected for a deficit of ^{206}Pb due to deficiency of ^{230}Th (*Schärer*, 1984), which results from the young ages of the Cerro Negro magmatic rocks. The data were regressed with the Isoplot software package (*Ludwig*, 2009). The decay constants are those of *Jaffey et al.* (1971). Uncertainties in the isotope ratios and the ages are given and plotted at 2σ (Table 2, Figure 68).

Scanning electron microscopy

The macroscopic properties of zircon can be determined using an optical microscope. In addition to those first order observations, the internal texture of zircon grains (such as primary magmatic zoning and possible cores) is best revealed by backscattered (BSE), secondary electron (SE) and cathodoluminescence (CL) imagery. For this purpose images of our rock samples were collected with a JEOL JSM 6460 LV scanning electron microscope at the Department of Geosciences, University of Oslo, equipped with an energy-dispersive X-ray (EDX) detector for qualitative elemental analyses. Thin sections or grain mounts of selected samples were C-coated prior to analysis. An acceleration voltage of 15 kV was used resulting in an average electron penetration depth of about 2 µm and an excitation volume width of approximately 1.6 µm. CL images were acquired using a JSM-6460 at 15 V acceleration voltage.

Major and trace element analyses

Crushing and pulverising for geochemical analyses was performed first using a steel crusher followed by a planetary agate mill at the University of Bonn, Germany. An agate mill was chosen for milling, as it is known to produce the lowest contamination. All samples were milled for 18 minutes (normal/reverse cycle) at 350 rpm. The powders were dried in an oven at 100°C over night. Subsequently, these powders were used for major and trace element analyses.

Major element analyses were performed by X-ray fluorescence (XRF) on fusion disks, which were produced by mixing 0.6 g homogenous powder with 3.6 g $Li_2B_4O_7$, the latter acting as a flux agent. To produce an isotropic glass and to avoid vesicle formation, the powders were heated to 1300°C using a five-step melting facility. The loss on ignition (LOI) was determined by comparing the weight of 1.5 g of the powdered samples before and after heating at 1000°C for one hour. The whole rock major element geochemistry of 15 samples was determined using the SUPERQ software package on a PANanalytical Axios X-ray spectrometer at the University of Bonn, Germany. The following major elements were determined: Si, Al, Fe, Mn, Mg, Ca, Na, K, Ti, P.

Analytical procedures for trace element analyses of 10 samples followed a slightly modified version of those of *Garbe-Schönberg* (1993); *Hoffmann et al.* (2011) involving a multi-step, multi-acid digestion of 100 mg aliquots of powdered samples with HF-HNO_3. In all stages Merck Suprapur® grade reagents (HF, $HClO_4$, HNO_3 and HCl) were used. Samples (100 mg) were digested with HF-$HClO_4$ in a high pressure/temperature system procedure and filled up to 50 ml. The dilution factor for all analysed samples was 1:6000.

In addition to the 10 samples, 1 blank and 1 rock standard (certified reference material (CRM); JA-1 andesite) were analysed. The list of samples chosen for geochemical analyses is given in the Tables 3 and 4. Trace element determinations were carried out with a Perkin Elmer/Sciex ELAN 6000 ICP-MS (quadrupole mass spectrometer) at the University of Cologne, Germany. Measurements of element concentrations were performed using internal standards Ru-Re (10 $ng.ml^{-1}$), to minimise drift effects, and two calibration solutions prepared from high purity chemical reagents. A batch of 5 samples was bracketed by two calibration procedures. Subsequently, accuracy and precision of determinations were checked with CRM (*Govindaraju*, 1994; *Dulski*, 2001).

The validity of the methods used and the quality of the data produced

Sources of error in geochemical analyses may arise for a variety of reasons. Careful handling and cleaning minimised contamination during sample preparation. For the most sensitive analyses agate was used for milling and ultra-pure reagents for sample dissolution. Furthermore, the composition of the "blank" was determined and subsequently the data were corrected for it. Other sources of contamination may be derived from the nature of the sample, for example if rocks are altered or contain inherited material. Thin alteration rims were cut off and only the freshest parts of the samples were used for subsequent analyses. Overall, the samples are considered to be rather fresh. Accuracy and

precision of trace element determinations were checked with CRM (*Govindaraju*, 1994; *Dulski*, 2001). Precision (relative standard deviation (RSD)) is better than ± 7%. Accuracy for the majority of elements is ± 6-8% compared with well-characterised CRM (JA-1) that was analysed along with the samples (Table 4). An additional uncertainty of 0.1% was produced during weighing.

Having discussed the validity of the methods used and the quality of analyses, we base our geological interpretation on the aforementioned data.

Results

Field observations

During four weeks of fieldwork a total area of roughly 250 km^2 was mapped. The resulting geological and structural map (Figures 20a, 20b) shows the relationships between Late Jurassic to Late Cretaceous sedimentary rocks and magmatic conduits. A sequence of four cross-sections (Figures 21a-d) illustrates these relationships in detail and provides an overview over the lateral differences in folding styles. A full list of field localities (waypoints (WP)) is given in Table 1 as latitude and longitude coordinates (degrees, minutes, seconds). Field data were corrected for magnetic declination and are presented as dip direction/dip angle for planar elements (bedding, faults, foliations). Linear elements associated to planes (striations, slickensides) are noted as pitch (between 0° and 90°) and pitch direction. In the following sections a detailed structural field description of magmatic conduits will be presented, followed by the description of tectonic structures.

Magmatic units

Two types of magmatic units with distinct geometries have been identified: sills and dykes. These units are exposed in different parts of the field area (Figure 22) and are incorporated into different structures. Thus, based on field relations and location, they have been grouped into:

Northern sills
Two subunits (NS_1, NS_2)

Central units
Dykes and sills that build Cerro Negro,
conduits N and S of these

Western unit
Undifferentiated magmatic body (WU)

Southern sills
Three subunits (SS_1, SS_2, SS_3)
Southern dyke
One big conduit (SD)

Cerro Colorado
Undifferentiated magmatic body

Figure 20a: Geological map of Cerro Negro de Tricao Malal and surrounding area, Neuquén Province, Argentina

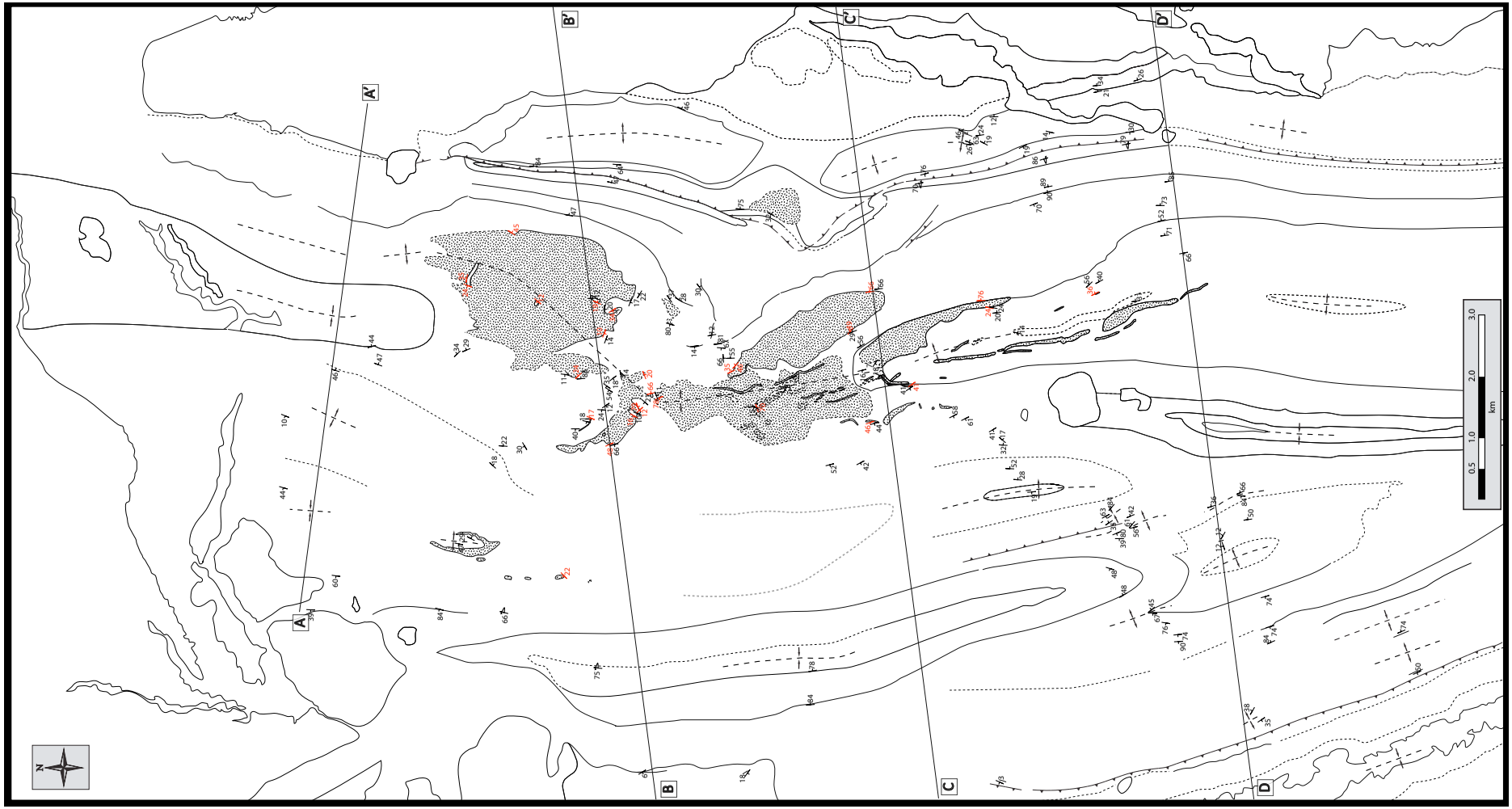

* contacts between magmatic units and sediments are marked in red

Figure 20b: Structural map of Cerro Negro de Tricao Malal and surrounding area, Neuquén Province, Argentina

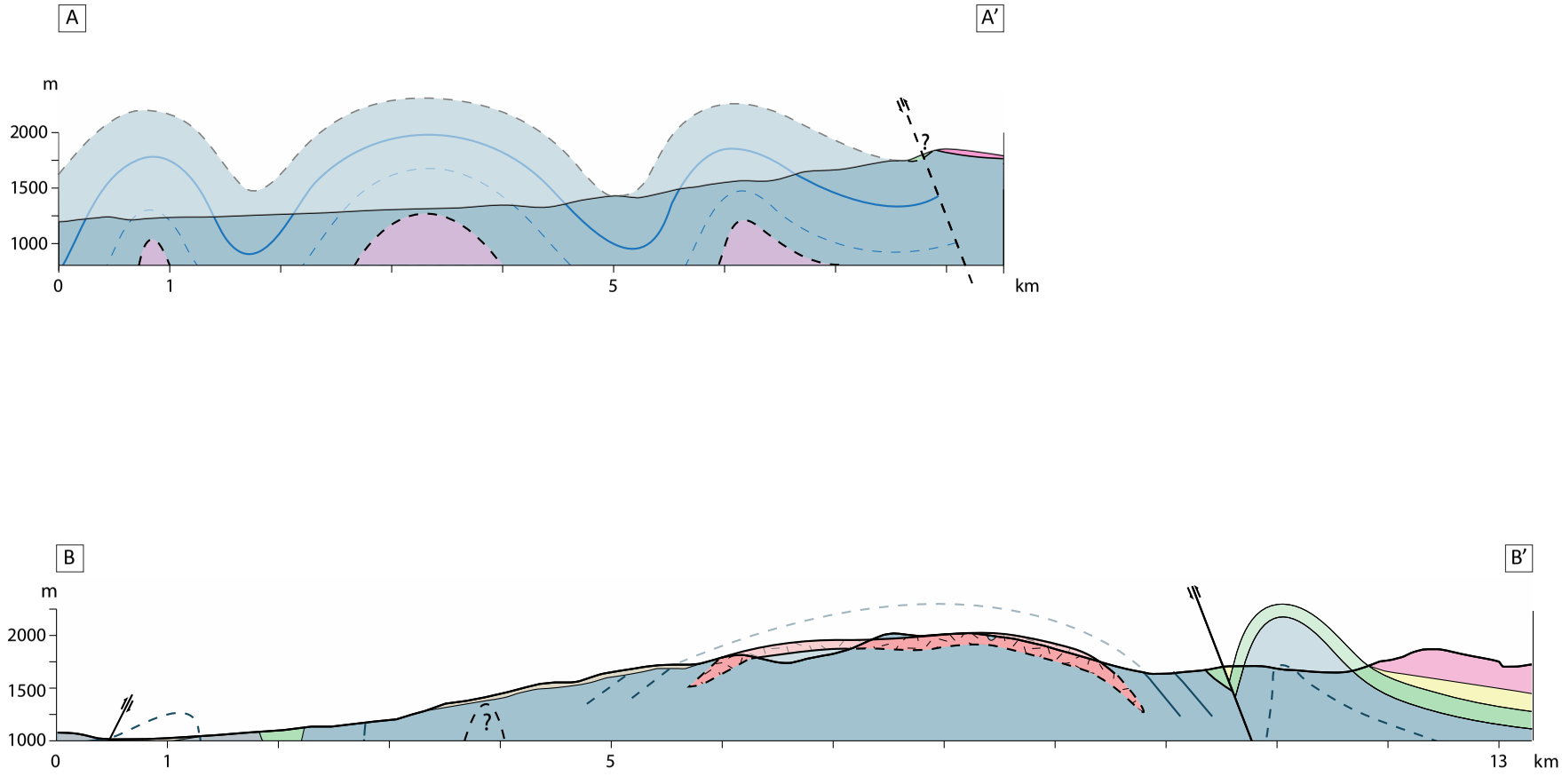

Figure 21a-b: *Structural cross-sections through the central (A-A') and central southern (B-B') part of the study area.*

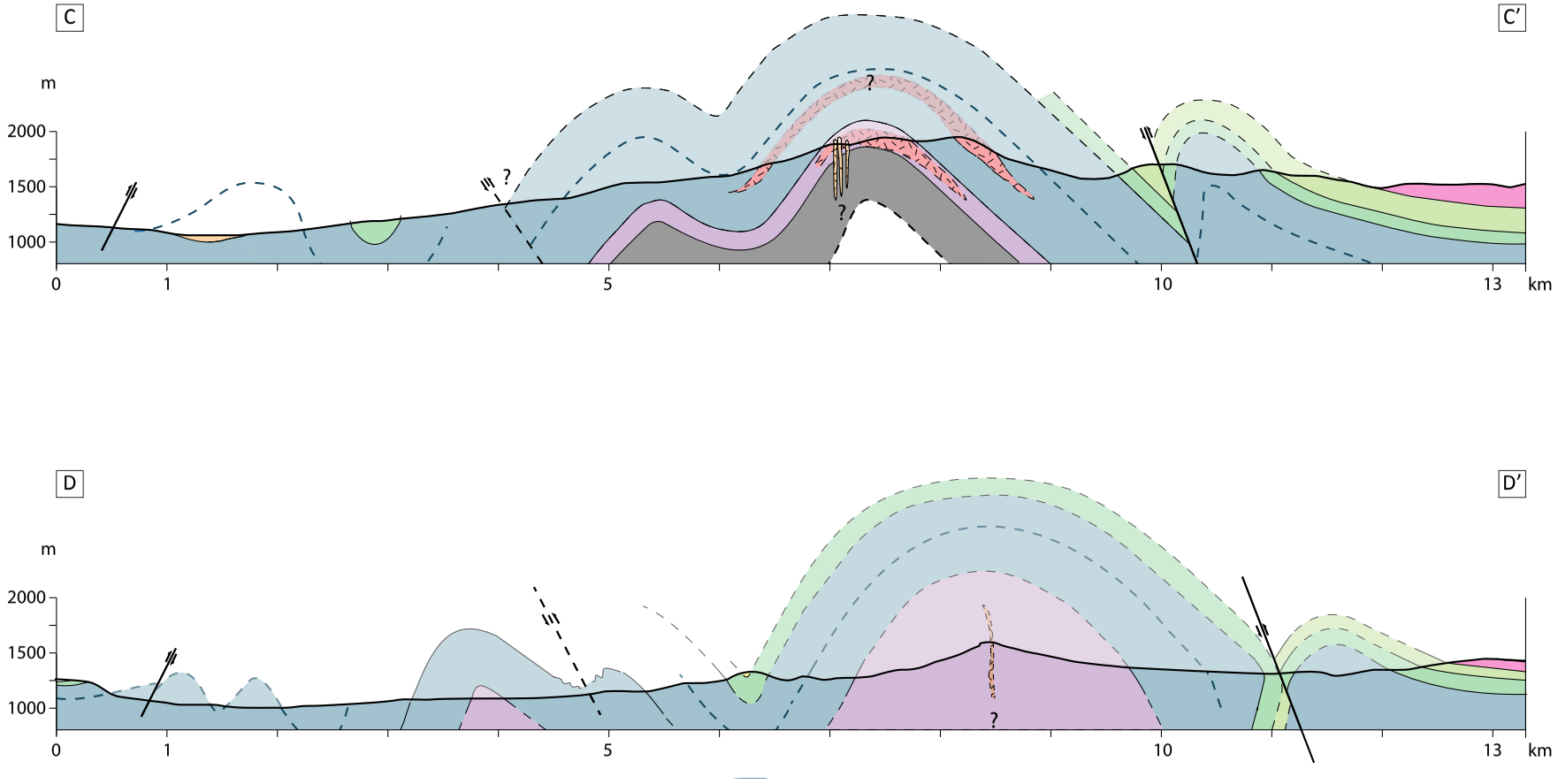

Figure 21c-d: *Structural cross-sections through the central (C-C') and central southern (D-D') part of the study area.*

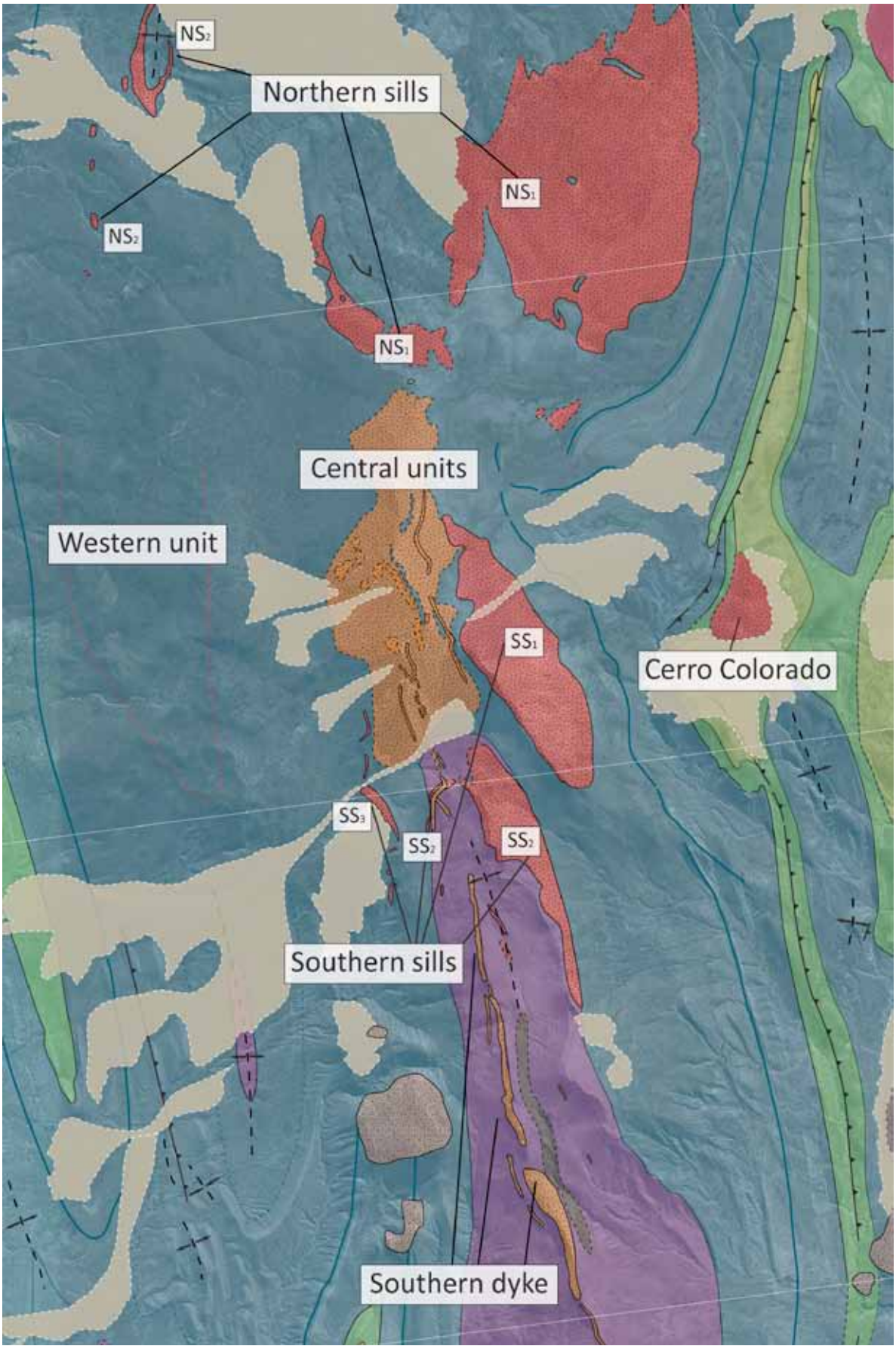

Figure 22: *Overview map showing the location of magmatic conduits. Sills are represented in red, dykes in orange. For bedding, contact data and map legend refer to main geological map (Figures 20a, 20b). For cross-sections refer to Figure 21a-d.*

Northern sills

NS_1 – In the North, roughly 4 km south of the village of Tricao Malal, the biggest outcrop of the magmatic system is accessible. This conduit has previously been mapped as a big sub-circular intrusion (*Zöllner and Amos*, 1973; *Leanza*, unpublished). Several concordant contacts between the intrusion and surrounding sediments were observed. The upper, southernmost contact of the sill to limestones and shales is clearly visible from the eastern flank of Cerro Negro looking towards the Northeast (Figure 23).

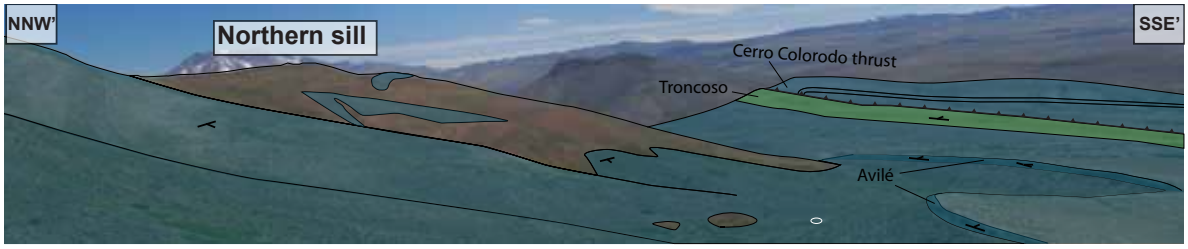

Figure 23: *Field relationships between the Agrio Formation and the sill in the northeastern part of the field area (WP 26-30). Structurally, the sill formed in a wide anticline and is located below the Lower Agrio limestones and shales. South of the big magmatic body, small patches of magmatic rocks have locally discordant contacts with the surrounding shales (centre foreground). White circle around car for scale.*

The Agrio shales dip gently (14°-22°) towards the South and the contact to the andesitic sill is concordant (Figure 24; WP 41, WP 55). This is also the case at the SSE margin of the intrusion (WP 49), where the bedding in Agrio (202/14) is conformable with the contact (201/10).

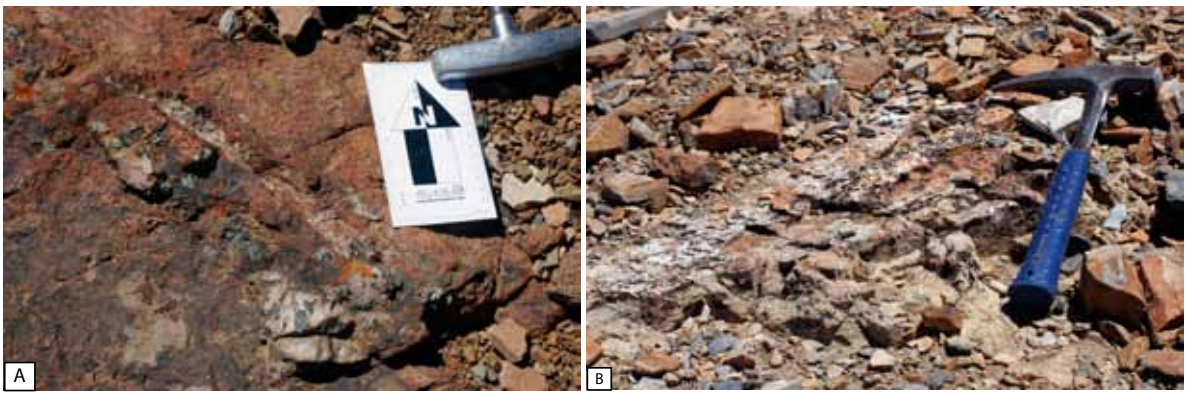

Figure 24: *Upper contact planes between NS_1 and Lower Agrio limestones.* ***a)*** *Wavy, overall concordant contact at WP 54 marked by a chilled margin (dark, fine-grained).* ***b)*** *Concordant contact at WP 55.*

Locally, several small patches of magmatic rocks crop out south of the big magmatic body (WP 35-39). The contacts are rather steep and mostly unconformable. From our field observations we cannot infer in which relation these rocks of andesitic composition are in respect to NS_1.

A small patch of Agrio limestones incorporated by the magmatic rocks of the sill was observed close to the southern limit of the intrusion (WP 53). The bedding in the limestones (89/12) is roughly concordant to the contact of the intrusion (123/19). The field relations suggest that this patch of Agrio limestone is sandwiched in the sill and was carried along as a "xenolith".

Further north, in the centre of the sill, a local outcrop of Agrio limestones surrounded by the intrusion was mapped (WP 67-68). The contact between the sill and the sediments is concordant and most likely represents the lower contact.

On the western side of NS_1 several contacts were observed. The upper contact of the sill to Agrio limestones has been measured at several localities and is locally discordant (WP 199-201). The basal contact (WP 253) of the flat-lying sill to Agrio limestones is less accessible and visible from the western side of NS_1 (Figures 25, 26). Structurally, the flat-lying sill was emplaced within the Lower Agrio Member, below the Avilé sandstones and is roughly concordant. As the outcrop conditions are limited, especially the lower contact cannot be followed over great distances.

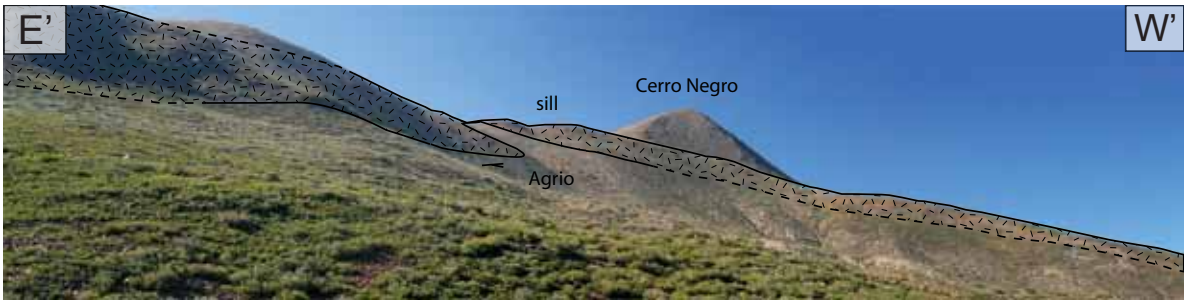

Figure 25: *The basal contact of the flat-lying NS_1, as seen from WP 251 looking towards the SSW. The contact between NS_1 and the surrounding Agrio limestones is locally discordant, but overall concordant.*

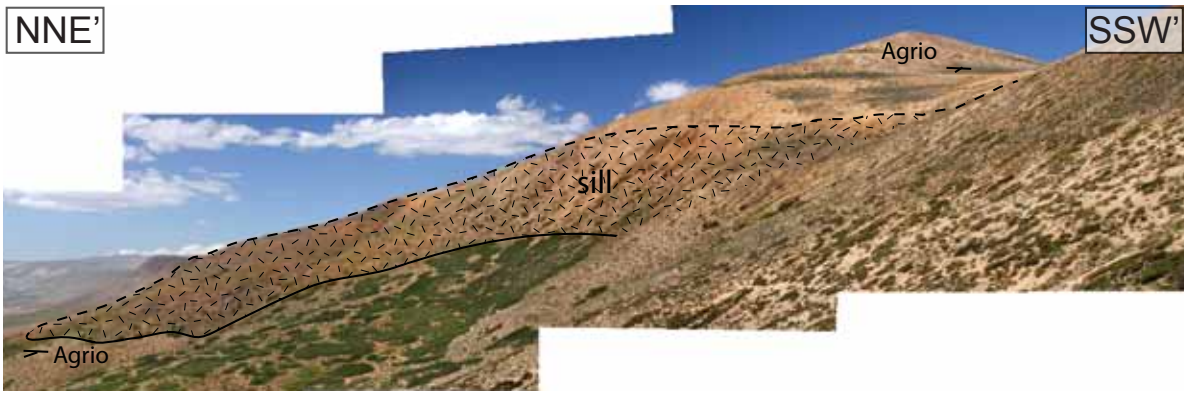

Figure 26: *View onto the basal and top contact of NS_1 as seen from WP 200-202, looking towards the East.*

In the North, close to two puestos (outposts), contacts of the intrusion to Agrio limestones were observed (WP 62-64). There is some variation between the measurements of contact planes between the Agrio limestones and the intrusion. Furthermore, the field relationships are not very clear, as most outcrops are eroded and covered by recent deposits. The contact planes, where clearly visible, are all marked by chilled margins, suggesting that here the upper contact of NS_1 is exposed.

On the eastern side of the sill, the upper contact to Lower Agrio limestones was measured in a small quarry close to the Ruta Provincial 2 to Tricao Malal (WP 18, Figure 27). Based on observations at this location, where the contact is very well exposed, the sill is again located below the Avilé Member

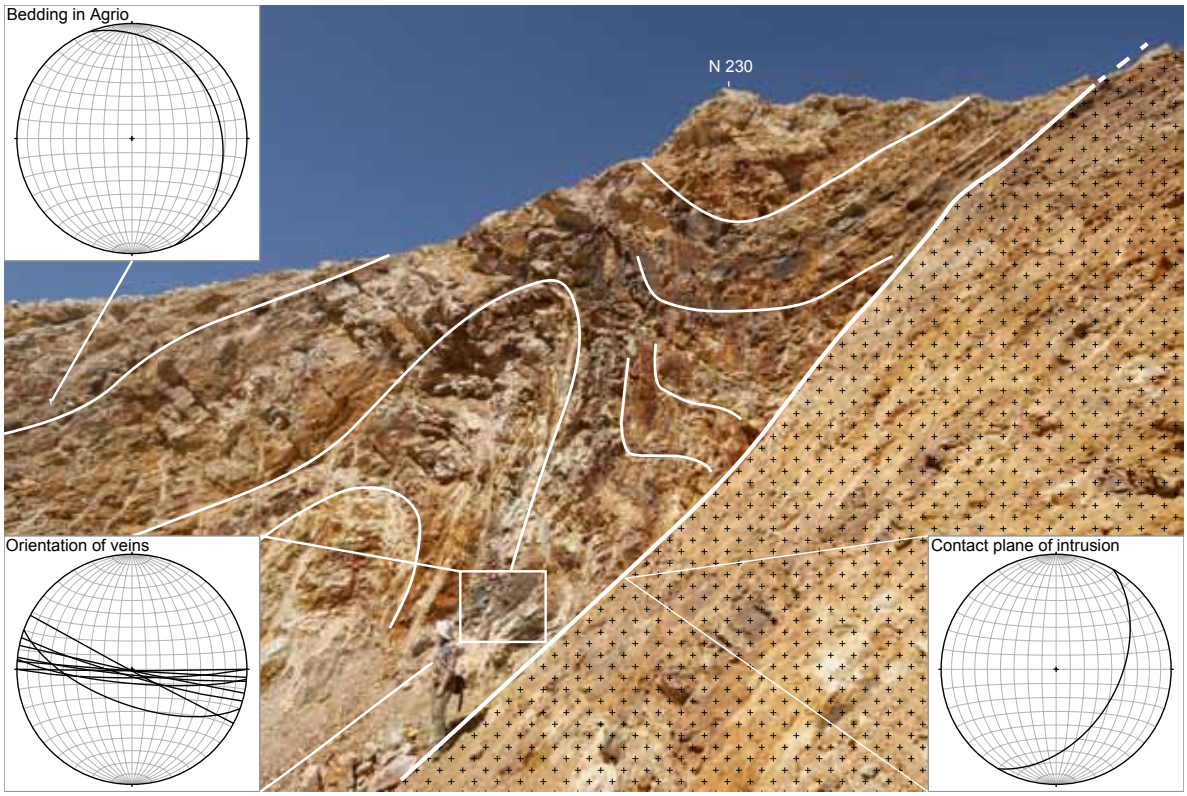

Figure 27: *Upper contact of NS_1 to deformed country rock at WP 18. Stereograms (insets, equal area - lower hemisphere) show bedding in Agrio limestones (upper left), contact plane of intrusion (bottom right), and orientation of mineralised veins (bottom left). Data (in situ measurements) are compatible with E-W shortening.*

of the Agrio Formation. The contact between the strongly deformed country rock (bedding: 72/24) and the sill (124/45) is locally discordant. Furthermore, mineralised dilational veins with an E-W orientation were observed at the contact between the magmatic body and the limestones. There is no evidence of slip on the mineralised planes.

Based on the aforementioned field relations of NS_1 and the surrounding Agrio limestones and shales, we infer that this magmatic conduit is a continuous and flat-lying sill that has not been described as such before. The northeastern part of NS_1 is connected to the magmatic rocks outcropping to its southwest. The connection between the two is covered by a thin layer of Agrio in between, which is best exposed from the western part, looking South (Figures 25, 26). Field relations are illustrated in cross-section B-B' (Figure 21b) and suggest that both, the sill (NS_1) and the surrounding sediments have been gently folded in a wide N-S oriented wide anticline, which will be described in the structural part.

NS_2 – The structure of the northwestern part of the field area is mainly constrained by the continuation of an anticline in the Agrio shales towards the South. A tightly folded sill is exposed in eroded riverbeds east of Ruta Provincial 42 towards Tricao Malal (Figure 28). It is strongly altered, light brown to orange in colour and its magmatic fabric is hard to recognise. There are several small and strongly altered outcrops of eroded magmatic rocks south of the anticline observed at this location. The contacts between the intrusions and the country rock are consistently concordant. The anticline that has been mapped in this part of the field area constrains the structure to the West of Cerro Negro, as there are no other outcrops.

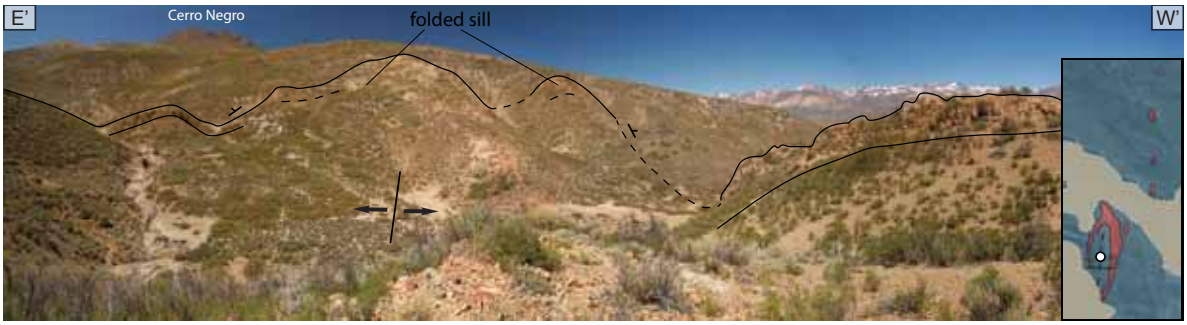

Figure 28: *Sill (NS_2) in the NE part (WP 74). Inset shows location on the geological map. White dot indicates location from which the photograph was taken (looking south). Anticlinal axis is marked. This tightly folded sill helps to constrain the structure of the central western part that is widely covered by Tertiary/Quaternary cover and lacks outcrops.*

WU – The field observations in the central western part alone do not reveal the structure of the Western Unit, as no contacts between the magmatic rocks and the sediments were observed. This part of the field area is widely covered in talus deposits derived from the magmatic units at the summit of Cerro Negro. These deposits are composed of an andesite groundmass containing mafic xenoliths.

Central units

The central part of Cerro Negro, including its summit (2520 m), is built-up by a dense network of sills and dykes as well as limestones and shales of the Agrio Formation that crop out as a thin layer between the intrusions (Figure 29). The bedding and several contacts between Agrio shales and intrusions (marked by chilled margins have been measured (inset Figure 29).

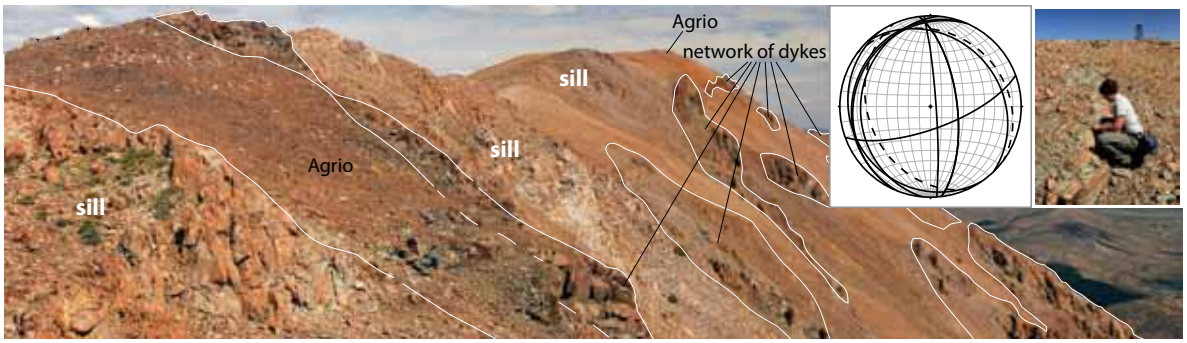

Figure 29: *Field relations at the summit of Cerro Negro (2520 m), looking towards the SSE (WP 250). The summit of Cerro Negro consists of a network of sills and numerous dykes, as well as local outcrops of Agrio limestones and shales (inset upper right). Stereogram (inset, equal area - lower hemisphere) shows the orientation of magmatic conduits and their relation to the country rock. Several contacts (solid lines) and bedding in the sediments (dashed lines) have been measured.*

Big parts of this central area are partly covered by talus slides and not accessible. Thus, the relationships between the crosscutting magmatic conduits are not clear. Only continuous dykes have been mapped in detail. These are consistently N-S oriented.

North of the summit of Cerro Negro and the central units, several subvertical plugs with discordant contacts (246/78 and 77/66) to the country rock of the Agrio Formation (bedding: 159/11) were mapped (Figure 30). These plugs are andesitic in composition, have big amphiboles and are slightly greener than the surrounding intrusions.

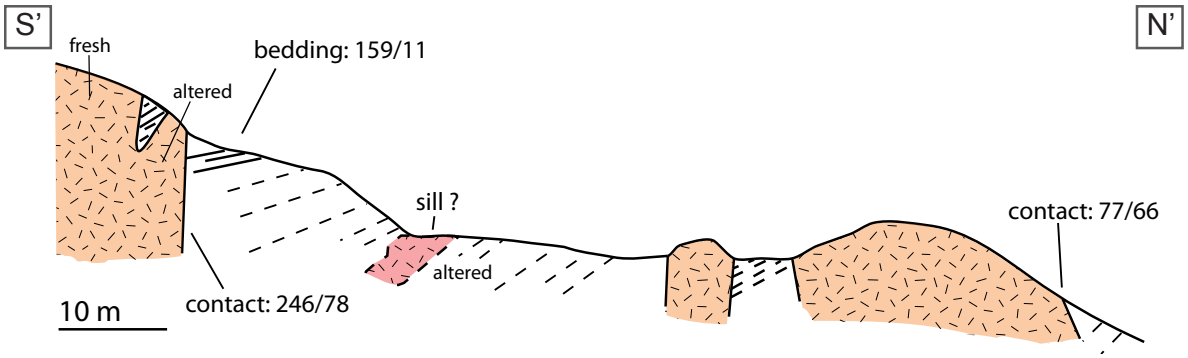

Figure 30: *Schematic cross-section through magmatic plugs with subvertical-vertical contacts (dykes: orange, sill: red) to Agrio limestones located north of the main Cerro Negro units (WP 194-195).*

South of the summit of Cerro Negro and the central units, crosscutting relationships between magmatic conduits were observed (Figure 31). A network of N-S oriented dykes crosscuts a deformed sill (SS_2) that is concordant with the bedding of Mulichinco (256/16). The sill belongs to a series of sills on the southwestern flank of Cerro Negro that will be described in the following section.

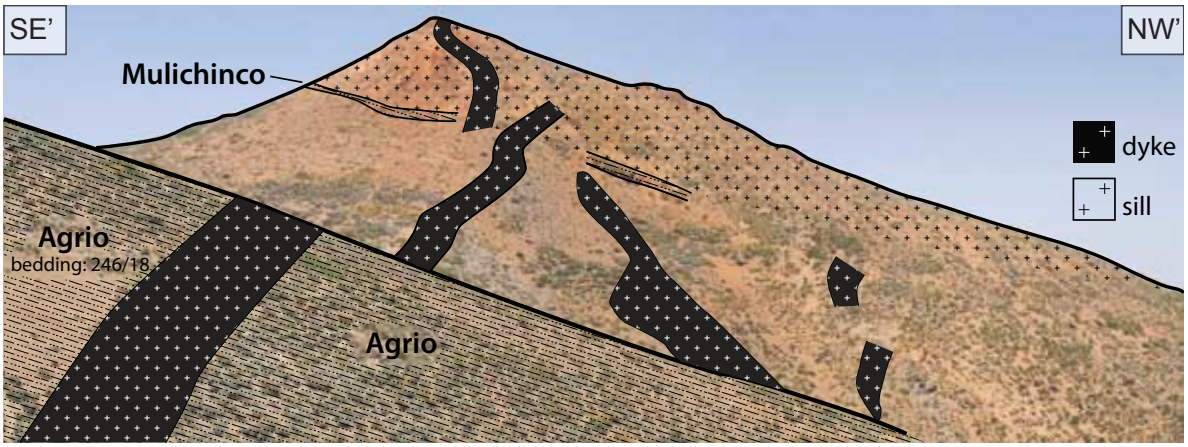

Figure 31: *Crosscutting relationships of magmatic conduits seen from WP 209. A folded sill (SS_2 - strictly concordant to bedding of the sediments of the Mulichinco Formation) is cut by a series of subvertical dykes (black).*

Southern sills

Two thick sills (SS_1, SS_2) that follow topography dominate the eastern and southeastern flank of Cerro Negro (Figure 32). Several contacts (upper and lower) to Lower Agrio limestones and Mulichinco Formation have been measured. All of these are concordant with local variations.

SS_1 – At the northernmost point of SS_1 that dominates the eastern flank of Cerro Negro (WP 33) the contact is marked by a chilled margin. The orientation of the contact (64/35) and the overlying baked shaly limestones (37/32) is roughly concordant. A few metres towards the Southeast the contact (46/46) is locally discordant to the bedding (88/55) in the Agrio shales. Overall, the bedding in these shales is highly variable, whereas the orientation of the sill is more constant.

At the southernmost tip of SS_1 (WP 245), the contact to the Agrio limestones above is very concordant (83/66). This sill is contained in the Lower Agrio Formation, below the Avilé Member. The lower, roughly concordant contact (36/46) to Agrio shales (69/29) is well exposed at WP 214 and can be followed for approximately 2 km.

SS_2 – The second thick sill (SS_2) is located SSE of the summit of Cerro Negro. It crops out between the Mulichinco Formation to the West and the Lower Agrio limestones to the East. In fact, the sill seems to be emplaced at the boundary between these units. Both, the lower and upper contact have been observed. The lower contact (Figures 33, 34; WP 270) to Mulichinco shales is concordant and dips moderately (102/24). The lower contact of SS_2 remains concordant for over 2 km. The upper contact of SS_2 (Figure 34; WP 269) to Lower Agrio shales is very sharp, steep (87/76) and locally discordant.

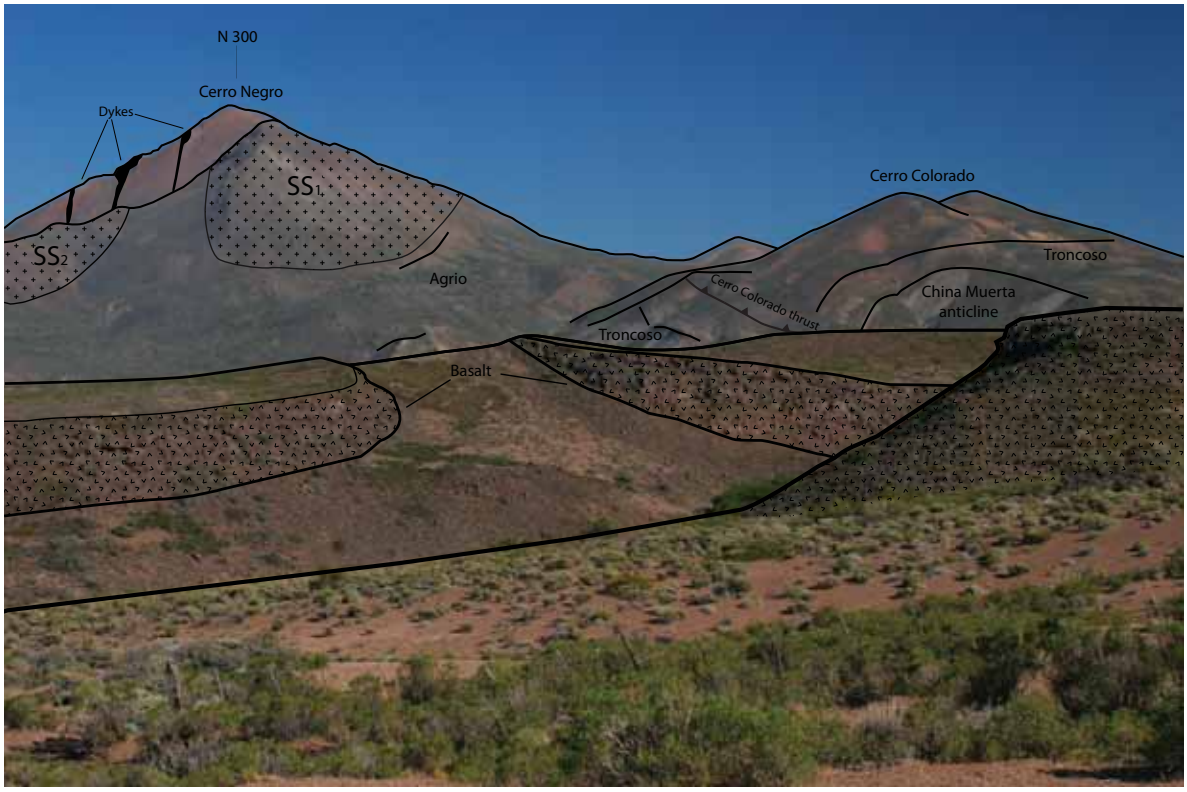

Figure 32: *View from WP 16 towards NNW onto the two folded sills (SS_1 and SS_2) on the southeastern flank of Cerro Negro (left). The trace of the Cerro Colorado thrust and the China Muerta anticline are visible (right). In the foreground there are basalts erupted by Tromen volcano.*

Figure 33: *Lower contact of SS_2 to Lower Agrio shales at WP 270.*

At the southern foot of Cerro Negro the same sill (SS_2) is 15 m thick and its lower concordant contact (240/41) to Agrio shales is visible. This sill is strongly altered and crosscut by a roughly N-S trending dyke (WP 227). These crosscutting relationships have been previously observed further north (WP 209; Figure 31), suggesting that the network of N-S trending dykes is more or less continuous and crosscutting SS_2 at several localities.

SS_3 – is located on the western flank, where it is emplaced in the Agrio Formation. As SS_1 and SS_2, this sill is andesitic in composition. The bedding in the Agrio shales (248/44) is concordant to the upper contact (250/46) of the sill and can be followed for more than 1 km (WP 208; Figure 35).

From structural observations in the country rock and the magmatic conduits we infer that all sills have been folded. SS_1 is on the eastern limb of a wide N-S oriented anticline. SS_3 represents the western limb of the same structure. The surrounding sedimentary units, as well as SS_2 have been also folded in this open anticline. This major structure will be described in the structural section as the Cerro Negro anticline (Figure 45). Following this anticline towards the North, it also folds the flat-lying sub-circular sill (NS_1). SS_2 is located in a lower stratigraphic level than SS_1 and SS_3. NS_1 is in the same stratigraphic level as SS_1 and SS_3.

All sills (NS_1, NS_2, SS_1, SS_2, SS_3) are stratigraphically located in the Lower Agrio or Upper Mulichinco Formations. The contacts between the sills and the country rock are often locally discordant (Figure 27). Overall, the contacts of NS_2, SS_1, SS_2, SS_3 are more concordant than those of NS_1. The contact planes are often marked by chilled margins, where the sediments have been baked by the heat from the magma, and thus appear darker in colour (Figure 24).

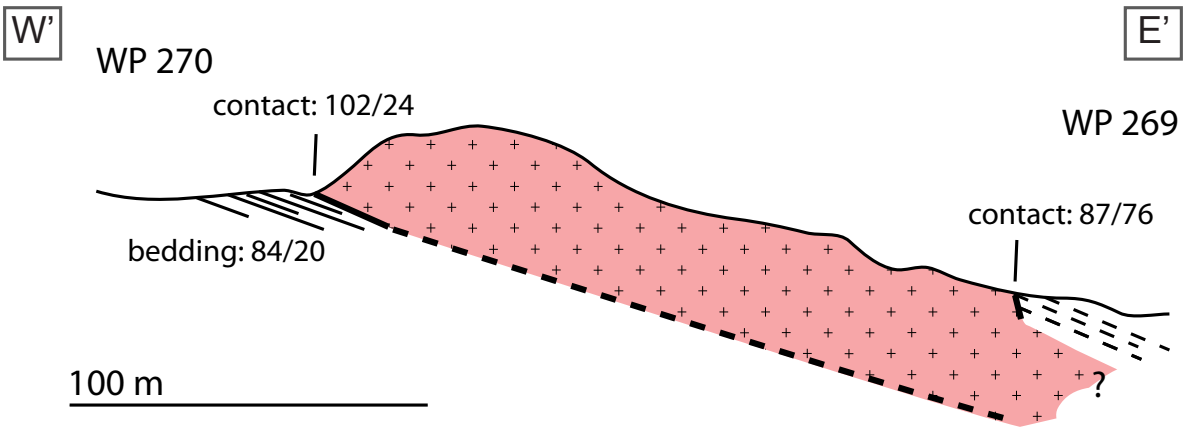

Figure 34: *Drawing illustrating the field relations between SS_2 and its lower, concordant contact to Mulichinco shales (WP 270) and upper, locally discordant contact to Lower Agrio shales (WP 269).*

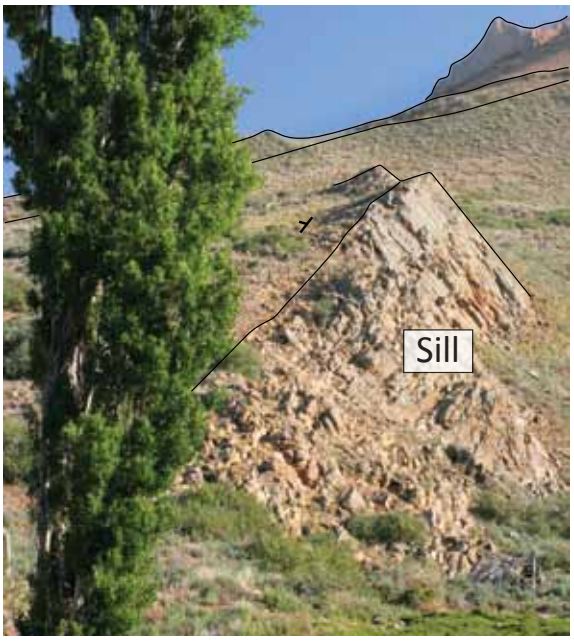

Figure 35: *Concordant upper contact of SS_3 to Agrio limestones (bedding indicated) observed at the SSW flank of Cerro Negro (WP 208).*

Furthermore, the grain size becomes smaller close to the contact.

SD – A thick, long dyke of andesitic composition was mapped in the central southern part of the field area. It is surrounded by the Mulichinco Formation and is locally in contact with Vaca Muerta shales. The roughly 6 km long magmatic conduit is oriented N-S and leads towards the central units of Cerro Negro (Figure 36). In its northern continuation several thin dykes (central unit) with the same orientation crosscut SS_2 (Figure 31). Their relation to the thick dyke (SD) is unclear, as no connectivity between the conduits has been observed. Their N-S orientation, however, suggests that they belong to the same network.

The field relations of the magmatic conduits are illustrated in cross-sections C-C' and D-D' (Figures 21c, 21d). Field observations indicate that the network of N-S oriented dykes is located in the centre of the Cerro Negro anticline. In other words, the dykes are limited to the hinge zone of the N-S oriented anticline (Figures 44, 45).

Cerro Colorado – It was previously mapped by *Zöllner and Amos* (1973) and assigned to the continental sediments of the Rayoso Formation, probably because of its striking colours. In fact, magmatic rocks orange to dark red in colour are exposed over most of the mountain. Except for the top, most of this hill is covered by eroded material, and the relation of the magmatic conduit that is exposed at the top of Cerro Colorado to the country rock and tectonic structures is not clear. No clear contacts between the intrusion and the surrounding Rayoso and Huitrín Formations were found. The bedding in the underlying Troncoso sandstone (close to the contact) is 119/32. Structurally, the intrusion is in the hanging wall anticline of the Cerro Colorado thrust, described in the structural part of this report (Figures 44, 45).

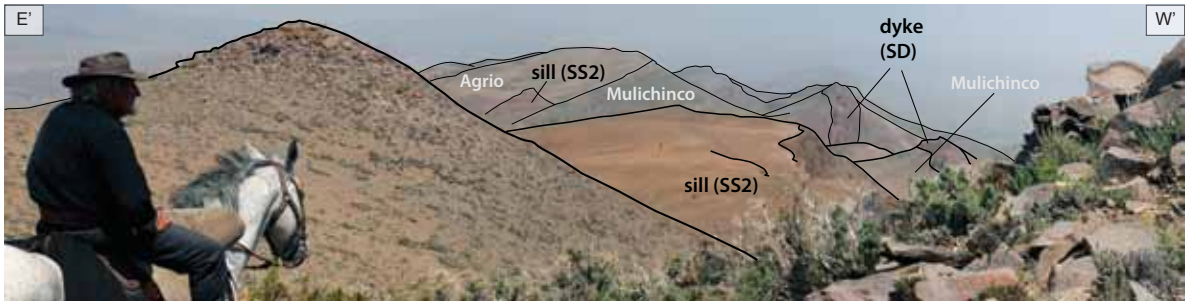

Figure 36: *View from the foot of Cerro Negro towards the South. The central dyke can be followed in the landscape for several kilometres.*

Structural observations

Throughout the field area, anticlinal and synclinal structures, as well as thrusts are predominantly N-S orientated (Figure 37). The most prominent folds and thrust faults will now be described. Tectonic structures (Figures 20a, 20b) will be described from east to west within these sectors:

Northern part

Cerro Negro anticline, Tricao Malal syncline, series of anticlines and synclines towards the West

Cross-section A-A' (Figure 21a)

Central part

China Muerta anticline, Cerro Colorado thrust, Cerro Negro anticline

Cross-sections B-B' and C-C' (Figures 21b-c)

Southwestern part

Series of synclines (SWs_1-SWs_4) and anticlines (SWa_1-SWa_3), Rio Curí Leuvú thrust.

Cross-section D-D' (Figure 21d)

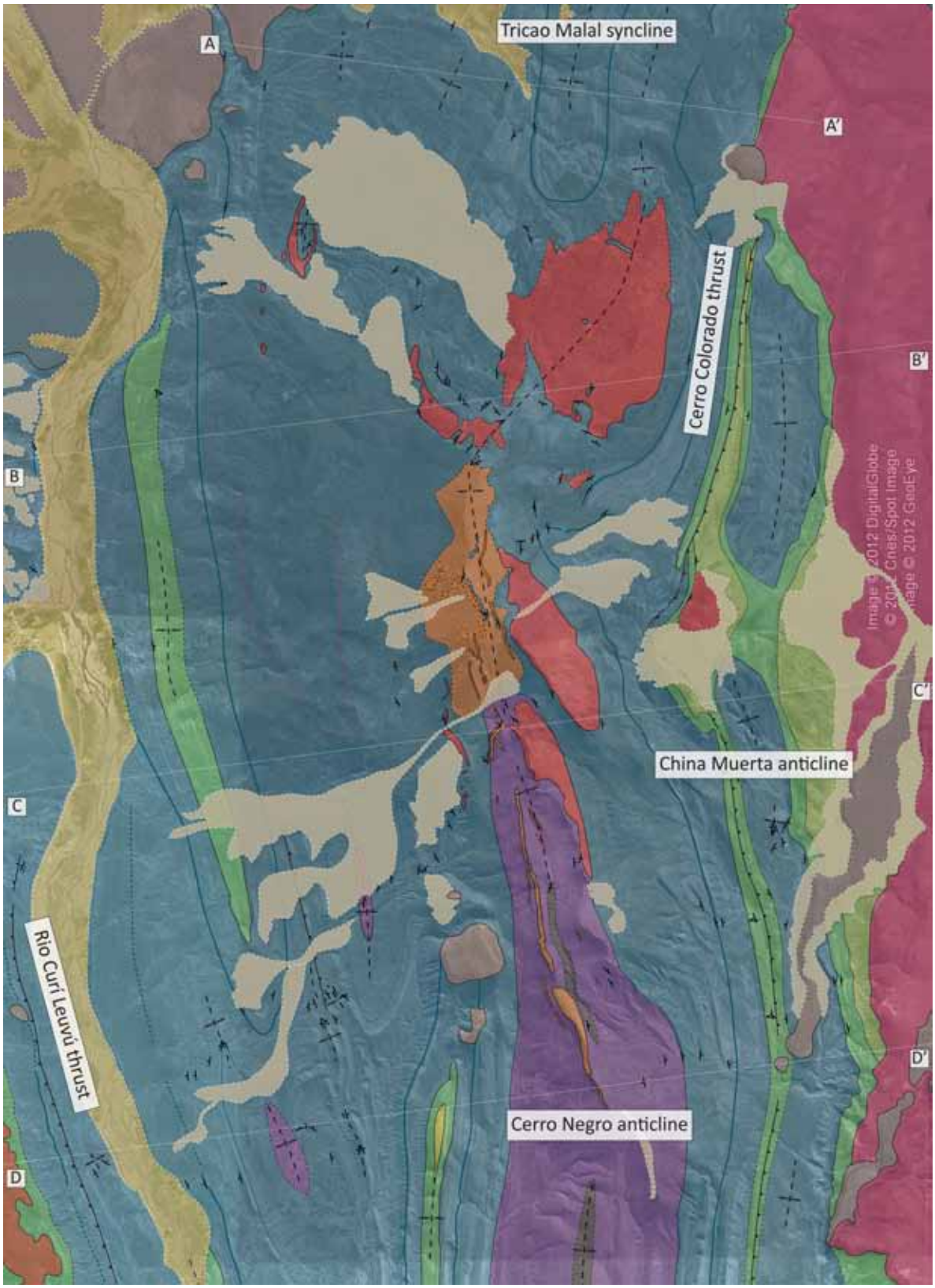

Figure 37: *Overview map showing the location of faults and folds. The locations of cross-sections are indicated (A-D). For bedding data and map legend refer to main geological map (Figures 20a, 20b). For cross-sections (A-D) refer to Figure 21a-d.*

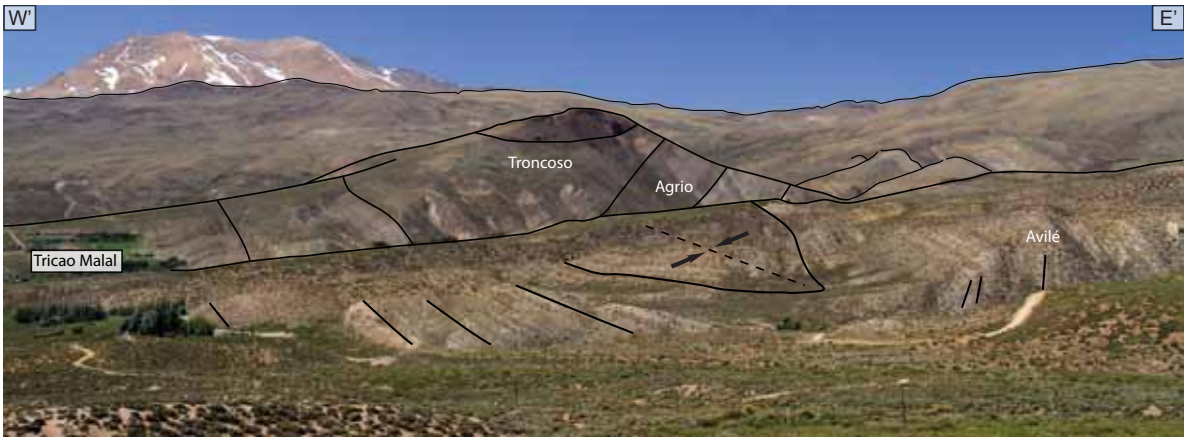

Figure 38: *View onto the slightly asymmetric syncline at the village of Tricao Malal. The structure folds the Agrio and Huitrín Formations, which are locally unconformably overlain by a thin layer of basalt.*

Northern part – A series of tight anticlines and synclines with similar wavelengths (ca. 1.5 km) was observed in the northern part. From east to west the first structure is the Cerro Negro anticline that has a short wavelength. Westwards, it is followed by the Tricao Malal syncline (Figure 38), another tight, slightly asymmetric structure with N-S orientation. It crops out at the southern entrance to the village of Tricao Malal, where it folds the Agrio Formation. Folding is well marked by the prominently banked Avilé sandstones. According to *Guerello* (2006) it also contains the Troncoso sandstones and Upper Huitrín gypsum, which are capped by a thin layer of basalt. On the western fold limb the bedding was measured (74/44). The eastern limb dips slightly steeper towards the West.

In the northwestern part, towards the Rio Curí Leuvú, the Tricao Malal syncline is followed by a series of tight anticlines and synclines within the Agrio shales. All of the folds have short wavelengths. Their orientation varies from N-S to NNE-SSW. The structures in this part of the field area are illustrated in cross-section A-A' (Figure 21a), which has been constructed strictly perpendicular to the strike and has a slightly different orientation compared to the cross-sections towards the South.

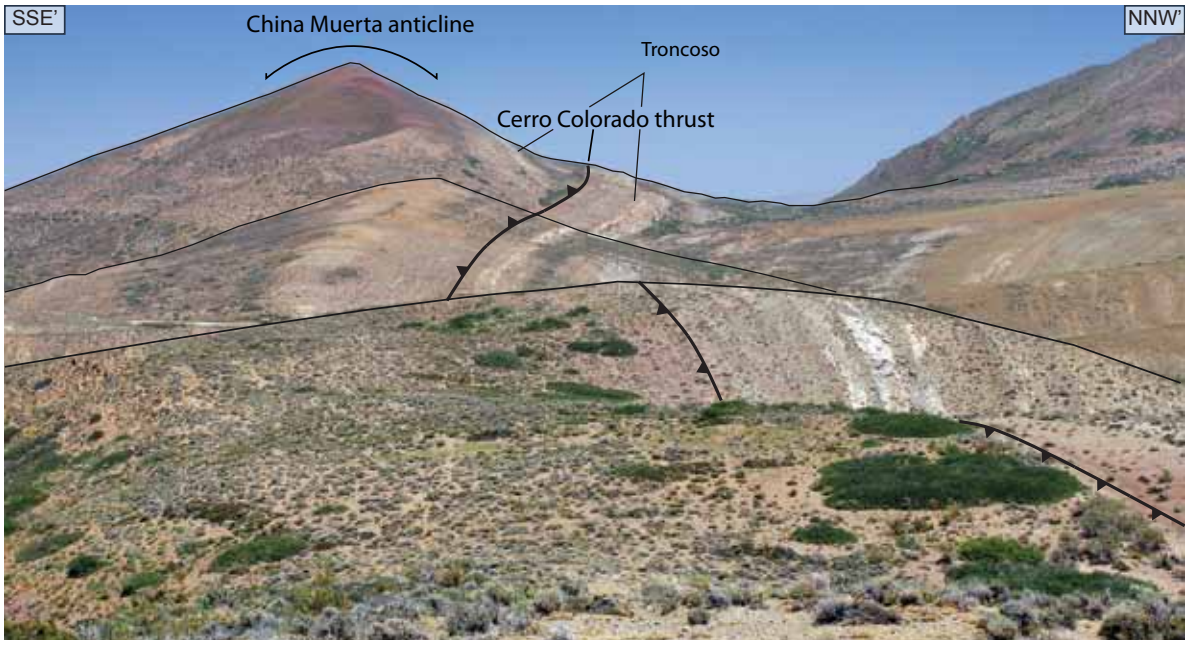

Figure 39: *View onto the China Muerta anticline at Cerro Colorado. The anticline is located in the hanging wall of the N-S oriented Cerro Colorado thrust that doubles the Troncoso sandstones.*

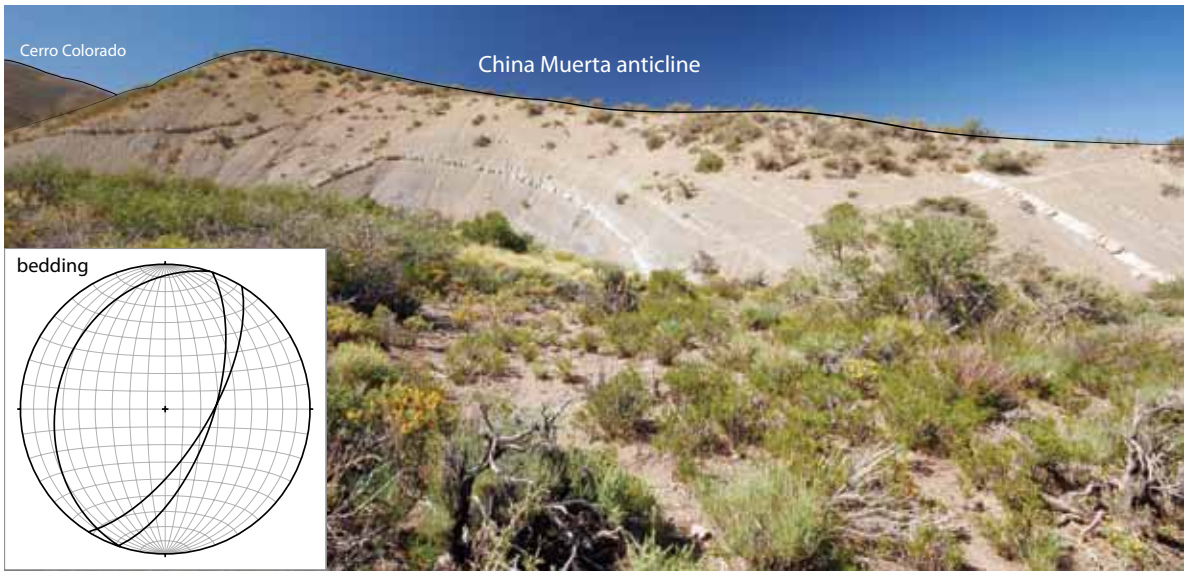

Figure 40: *Upper Agrio shales folded in the China Muerta anticline located in the hanging wall of the Cerro Colorado thrust. Observed SSE of Cerro Colorado (WP 120), looking towards the North. Stereogram (inset, equal area - lower hemisphere) shows bedding in Agrio limestones in both fold limbs. The fold axis is oriented NNE-SSW.*

Central part – Moving southwards, the China Muerta anticline is exposed along the eastern margin of the field area. The west verging anticline is located in the hanging wall of the Cerro Colorado thrust. It folds the Agrio and Huitrín Formations. Furthermore, the small magmatic intrusion at Cerro Colorado is restricted to the China Muerta anticline (Figures 32, 39, 43).

South of Cerro Colorado, the China Muerta anticline folds the shaly limestones of the Upper Agrio Formation. The orientation of the fold axis is NNE-SSW (Figure 40).

On the eastern limb of the China Muerta anticline a series of outcrop-scale reverse faults affect the banked sandstones of the Troncoso Member (Figure 41). The faults run roughly parallel to the bedding.

Striated fault planes were observed in Troncoso sandstones in a dry riverbed (Figure 42; WP 108). These small-scale structures result from normal faulting, indicated by the subvertical striations espe-

Figure 41: *Fault in Troncoso sandstones SSE of the China Muerta anticline in the hanging wall of the Cerro Colorado thrust (WP 147). Stereogram (inset, equal area - lower hemisphere) shows orientation of fault planes (solid lines) and bedding (dashed lines).*

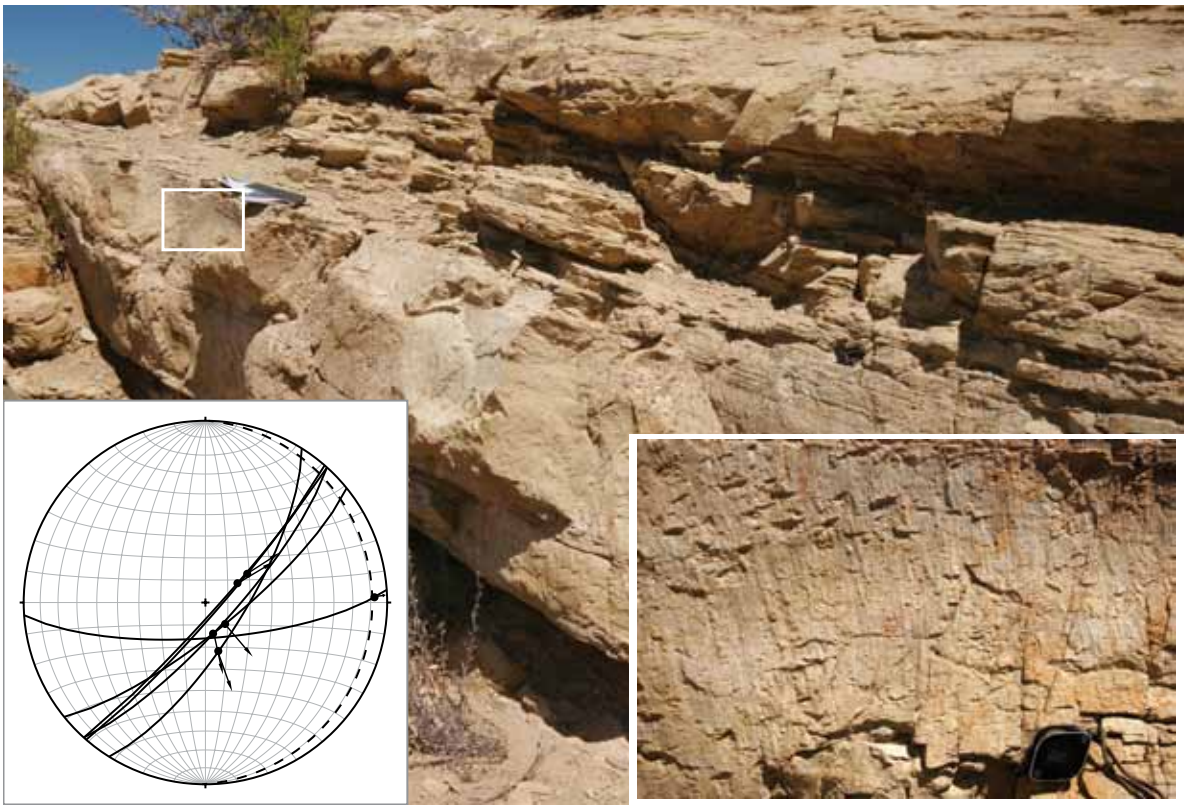

Figure 42: *Faulted sandstones close to the hinge of the China Muerta anticline (WP 108, looking towards WNW). Striations were observed on the surface of the fault plane on the footwall (detail, bottom right) indicating normal sense of movement. The hanging wall of the normal fault is removed. Stereogram (inset bottom left, equal area - lower hemisphere) shows bedding in Troncoso sandstones (dashed line), fault planes measured along the riverbed (solid lines) and striations (dots). Arrows indicate the motion of the hanging wall. Data are compatible with local extensional domains in the China Muerta anticlinal hinge.*

cially on the footwall fault plane (inset Figure 42). On a bigger scale, local extensional domains are located close to the hinge zone of the China Muerta anticline. The orientation of the fault planes is parallel to the NNE-SSW oriented axis of the China Muerta anticline.

The Cerro Colorado thrust is oriented N-S and verges towards the East. It can be followed along the eastern margin of the study area for roughly 25 km. It is best visible on the western flank of Cerro Colorado, where it offsets and doubles the Troncoso sandstone of the Upper Member of the Huitrín Formation (Figures 32, 43). The gypsum of the Upper Huitrín Formation acts as a detachment surface. Here, the China Muerta anticline in the hanging wall of the Cerro Colorado thrust is accessible. The trace of the thrust seems to be mostly covered at Cerro Colorado and its relation to the small

Figure 43: *Field relations at the western flank of Cerro Colorado, viewing towards ESE. The Cerro Colorado thrust offsets Troncoso sandstones. Gypsum of the Upper Huitrín acts as detachment surface. Cerro Colorado itself is built of a small magmatic plug that is heavily eroded. Thus, the field relations of the magma conduit to the country rocks are not entirely clear. The intrusion seems to be contained in the China Muerta anticline.*

intrusion is not entirely clear, but seems to bend around it (Figure 43). South of Cerro Colorado the fault trace is present, but it is less pronounced than in the North. This is to due the almost vertical bedding of the Troncoso sandstones and the overall outcrop conditions. Very local outcrops of Huitrín gypsum were observed along the fault trace (WP 116, 143, 146).

From the summit of Cerro Negro (2520 m) a good overview over the field relations in the central to southern part can be obtained (Figure 44). From East to West, there is the China Muerta anticline in the hanging wall of the west-verging Cerro Colorado thrust. These are followed by two sills (SS_1 and SS_2) that build the eastern flank of Cerro Negro, a central N-S trending dyke (SD) that is located at the hinge of the wide Cerro Negro anticline. The same anticline folds the two sills that crop out locally towards the West. A series of short wavelength anticlines and synclines deform the sediments in the West towards the east-vergent Rio Curí Leuvú thrust.

A wide, central anticlinal structure dominates the centre of the mapping area. The measurements at the summit of Cerro Negro (Figure 29) together with those E and W of the mountain illustrate this. The Cerro Negro anticline is best observed from the southern foot of Cerro Negro looking towards the North (Figure 45). Based on field relations magmatic bodies belonging to the same structure have been identified (and are coloured in different shades of grey). The southern sills (SS_1, SS_2 and SS_3) have been folded. SS_1 and SS_3 belong to the same conduit. SS_2 crops out almost continuously.

Dykes (black) strike N-S and are located close to the hinge of the anticline. Locally, dykes crosscut the folded sills. Towards the South, the Cerro Negro anticline folds the Mulichinco Formation with Vaca Muerta shales in the core. The field relationships at this location are illustrated in cross-section C-C' (Figure 21c).

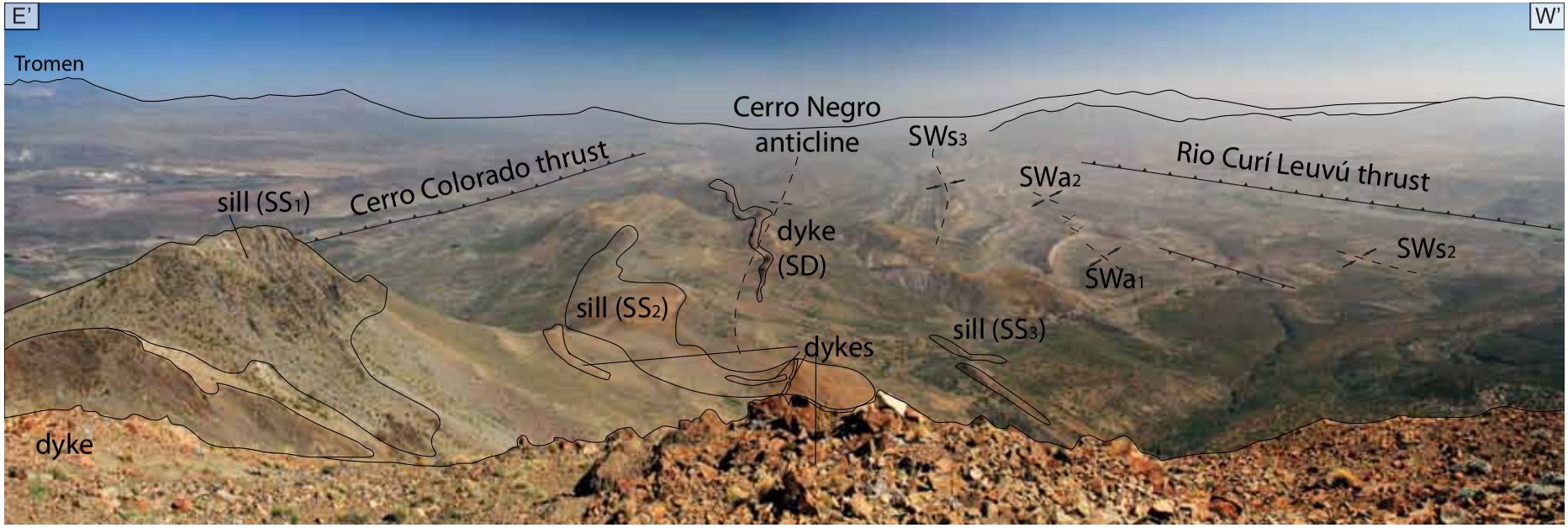

Figure 44: *Overview over the central to southern part of the field area. View from the summit of Cerro Negro towards the South. The Cerro Colorado thrust (west-verging) and Rio Curí Leuvú thrust (east-verging) are the main thrusts in the field area. A series of tight anticlines and synclines folds the Early Cretaceous sedimentary units. Two sills are folded in an anticline. Sediments and SS_2 are crosscut by N-S striking dykes that are restricted to the Cerro Negro anticlinal hinge. Fold axes and traces of the magmatic intrusions are indicated.*

Figure 45: *The main Cerro Negro intrusive body consists of a network of sills and dykes. Two thick sills have formed in a central anticline. The N-S oriented dykes (perpendicular to the shortening direction) are close to the hinge and locally crosscut the folded sills. Crosscutting field relationships between the sills (different shades of grey), and the network of subvertical dykes (black) can be seen on the southern flank of Cerro Negro (2520 m).*

Southwestern part – South of the village of Los Menucos, close to the Rio Curí Leuvú, a series of tight N-S and NNE-SSW oriented synclines (SWs_1-SWs_4) and anticlines (SWa_1-SWa_3) crop out (Figure 46). These are all within the Agrio limestones and shales. Two of the anticlinal cores (SWa_1, SWa_2) contain the fossiliferous sandstone of Mulichinco. Three synclines (SWs_1, SWs_2, SWs_3) have the Troncoso sandstone in their core. All folds have short wavelengths and locally there are drastic changes over several metres (Figure 47). The field relations and structural styles in this part of the field area are illustrated in cross-section D-D' (Figure 21d).

SWs_1 is a tight syncline and one of the few places where the gypsum of the Huitrín Formation is preserved. To the West, it is followed by an open anticline (SWa_1) that folds the Agrio and Mulichinco Formations. Close to the western limb of SWa_1 a series of small-scale anticlines and synclines with very short wavelengths fold the Agrio shales. West of SWa_1 a west-verging thrust was observed (Figure 47).

Further towards the West, SWs_2 folds the Agrio limestones and Troncoso sandstone in a tight syncline. This structure can be followed towards the North, but field relations towards the South become unclear. In its southern continuation it is immediately followed by an anticline (SWa_2). The transition between the two is very short in wavelength. This illustrates how abrupt changes in folding and faulting can take place in shaly lithologies.

SWa_2 is an anticline in the Agrio and Mulichinco Formations that is relatively open in the South (WP 126) and becomes very tight towards the North. Its very tight hinge zone is preserved at WP 127 (Figure 48).

Further towards the West, there is a tight syncline that is partly covered by the riverbed of the Rio Curí Leuvú (SWs_3). Then, there is another anticline (SWa_3) at WP 167 (Figure 49), directly east of the Rio Curí Leuvú thrust.

The Rio Curí Leuvú thrust marks the western edge of the field area. This important structure is within the Agrio Formation and doubles the Avilé sandstones. The trace of the thrust can be followed along the Ruta Provincial 41 for approximately 15 km to the West of the riverbed of Rio Curí Leuvú (Figures 50, 51).

In an outcrop north of Los Menucos (WP 170-172), the thrust can be observed from several angles (Figure 51). In fact, at this location the trust is not a simple plane, but a fault zone of several hundred metres. Locally, Avilé sandstones are folded close to the thrust plane and form a tectonic mélange. As further north (Figure 50), the east-verging thrust is contained in the Agrio Formation and doubles the prominent Avilé sandstones.

The westernmost syncline (SWs_4) is exposed in the southwestern corner of the field area, where it folds Troncoso sandstones and undifferentiated cover. Similar to all of the aforementioned structures in the Southwest, it trends NNW-SSE.

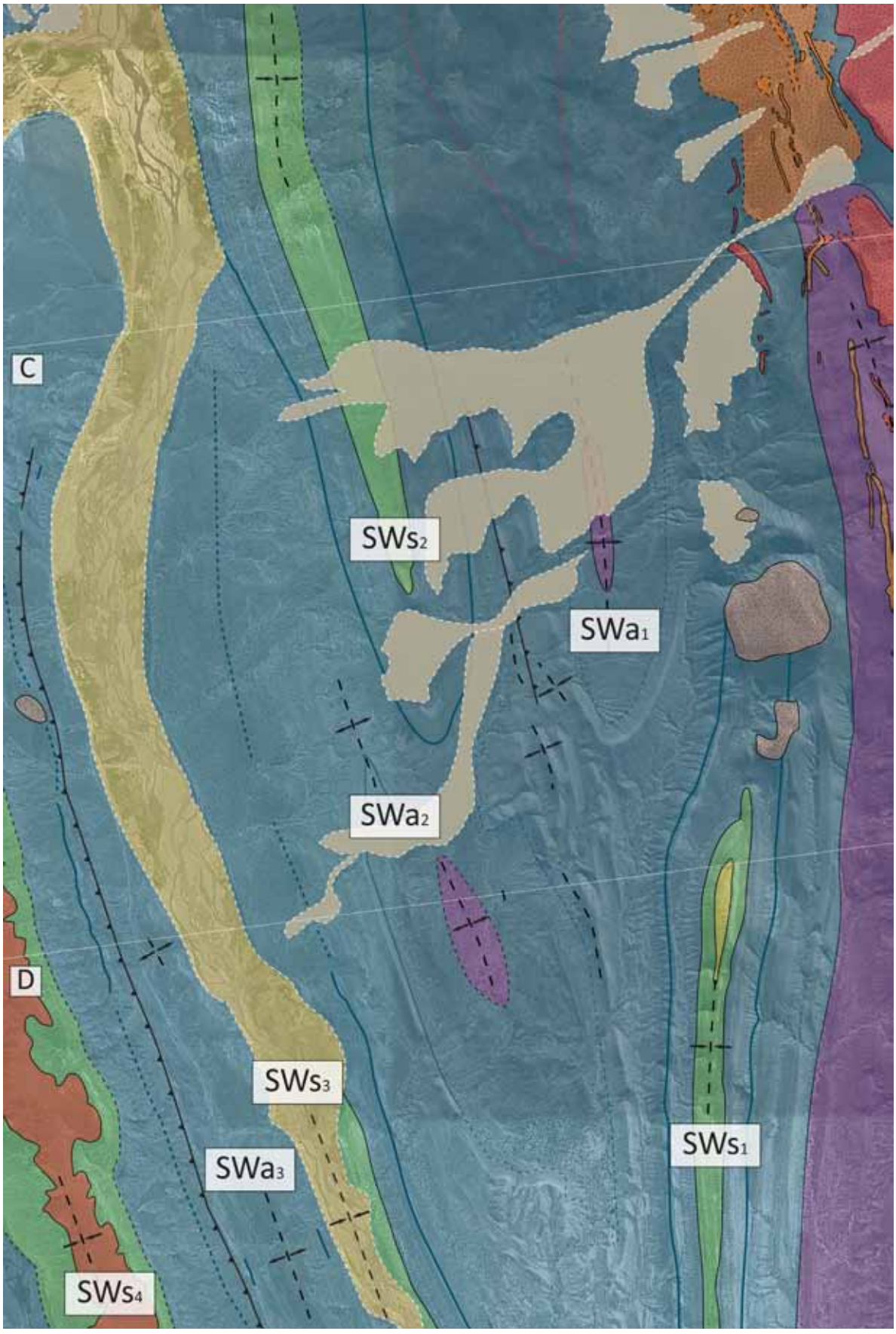

Figure 46: *Overview over the structures mapped in the SW part. The locations of cross-sections are indicated (A-D). For bedding data and map legend refer to main geological map (Figure 20a).*

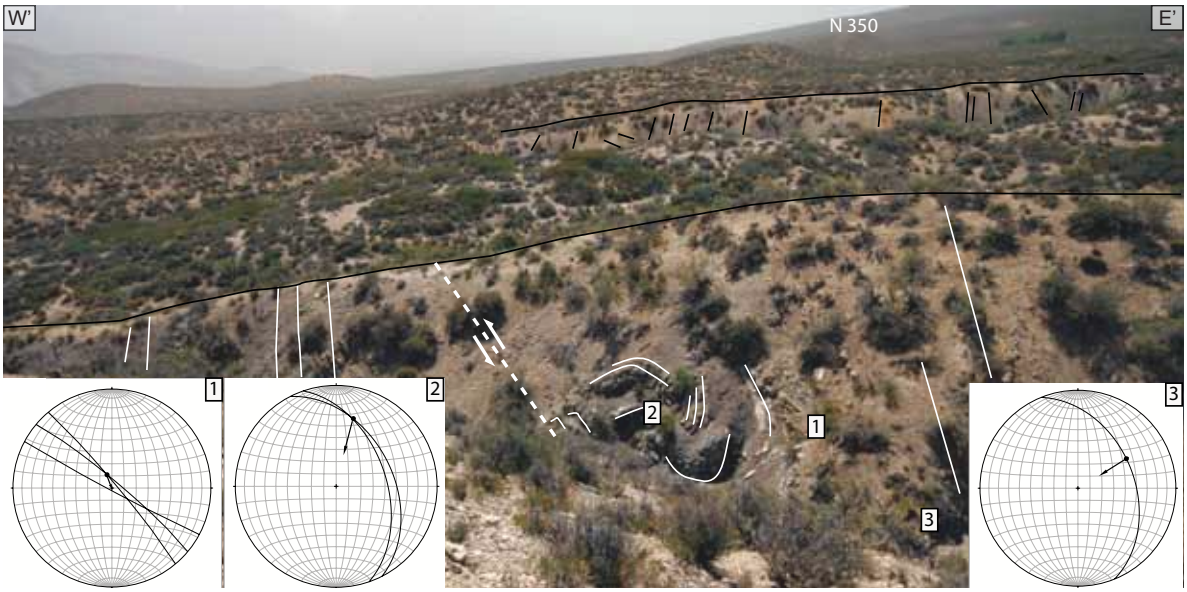

Figure 47: *Folded and faulted Agrio shales between SWa_1 and SWs_2, close to a local thrust. At this location (WP138) fault planes (solid lines) and striations (dots) were measured. Stereograms (insets, equal area - lower hemisphere) illustrate the measurements. Arrows indicate sense of motion. Data is consistent with west-vergent thrusting. The orientation of the thrust plane is estimated, as the plane is wavy and mostly covered.*

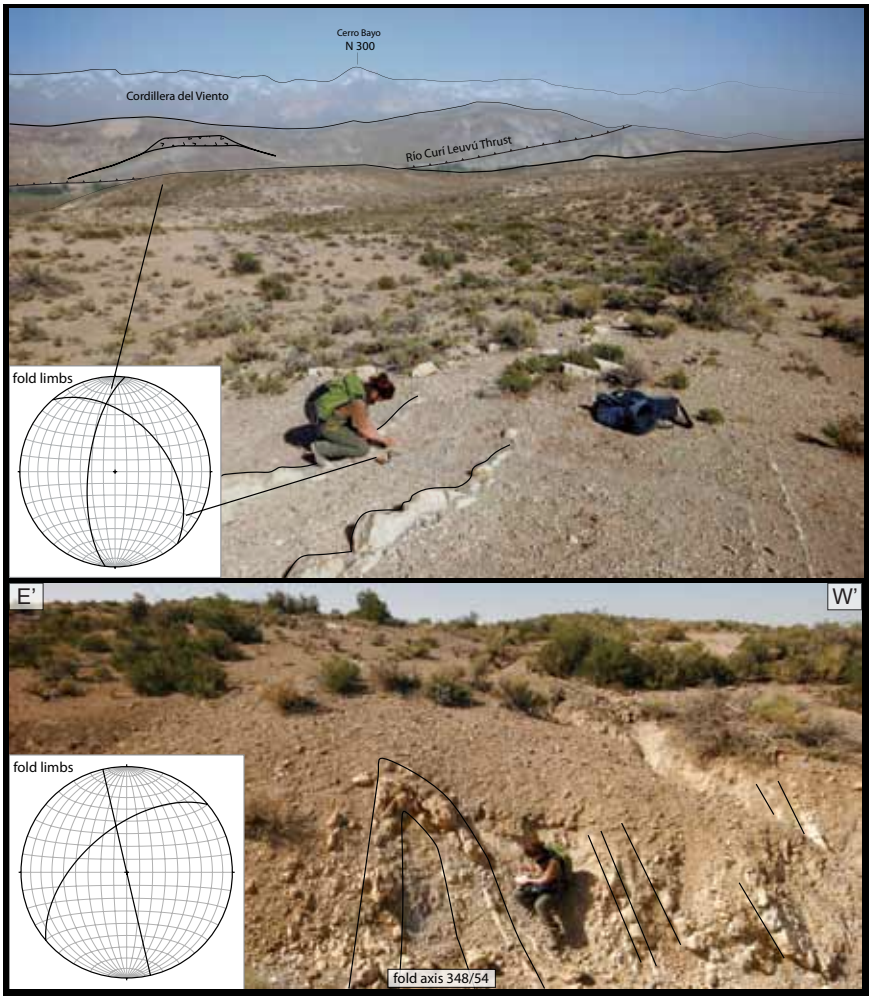

Figure 48: *Different views of SWa_2 folding Agrio limestones. Stereograms (insets, equal area – lower hemisphere) show bedding in both fold limbs. Relatively open anticline in Agrio limestones at WP 126 (top). The orientation of the fold axis is 353/30. The trace of the Rio Curí Leuvú thrust can be seen in the background. The same anticline becomes very tight towards the South (bottom). The hinge zone is preserved at WP 127. The orientation of the fold axis is 348/54.*

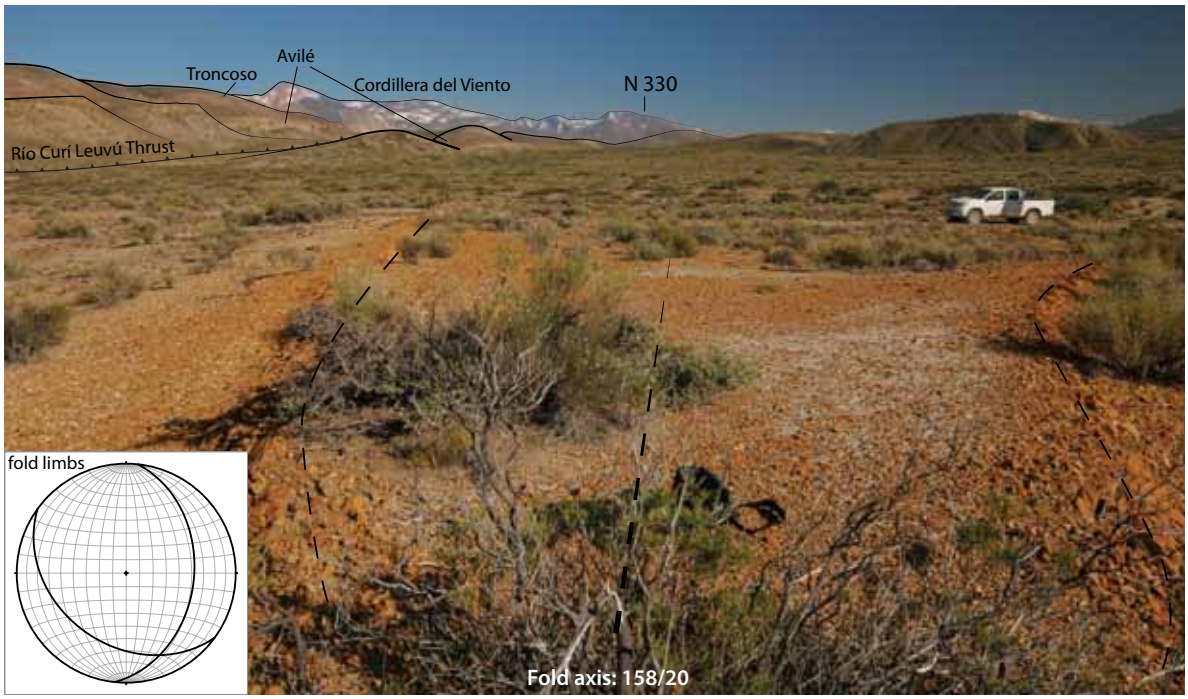

Figure 49: *SWa$_3$ at WP 167 incorporates the Agrio limestones in an isoclinal fold. Stereogram (inset, equal area – lower hemisphere) shows measurements from both fold limbs. Anticlinal axis (158/20) is marked. The Curí Leuvú thrust (upper left) doubles the Avilé sandstones. View towards NNW.*

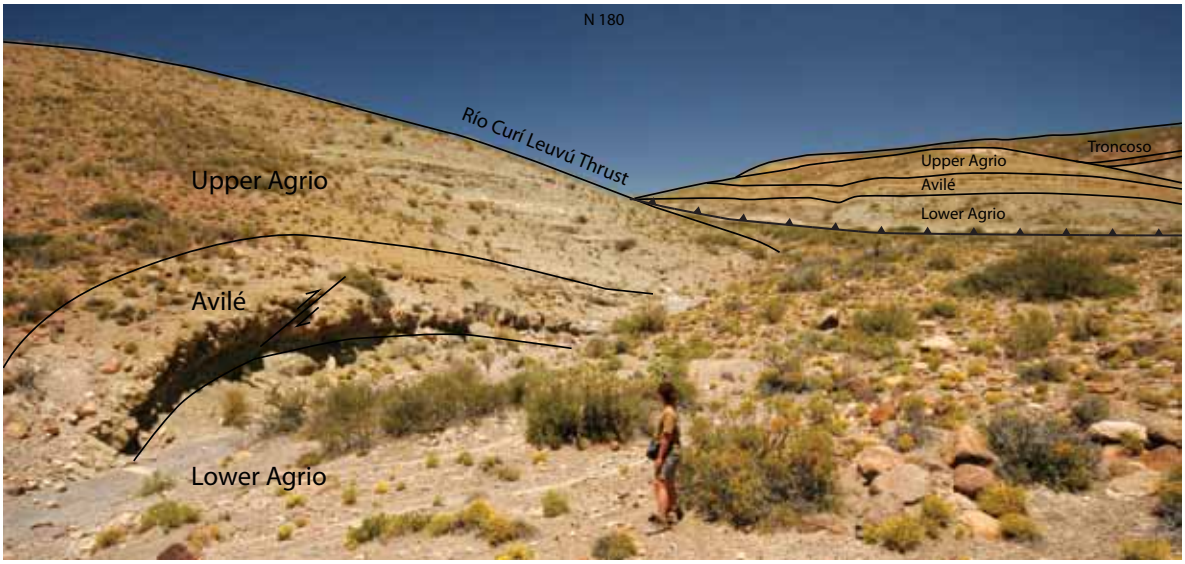

Figure 50: *Field relations east of Ruta Provincial 41, viewing towards SSW (WP 173). Folded Agrio Formation with small reverse fault in Avilé sandstones (foreground). The Rio Curí Leuvú thrust (centre) offset the Agrio Formation and doubles the sequence (background).*

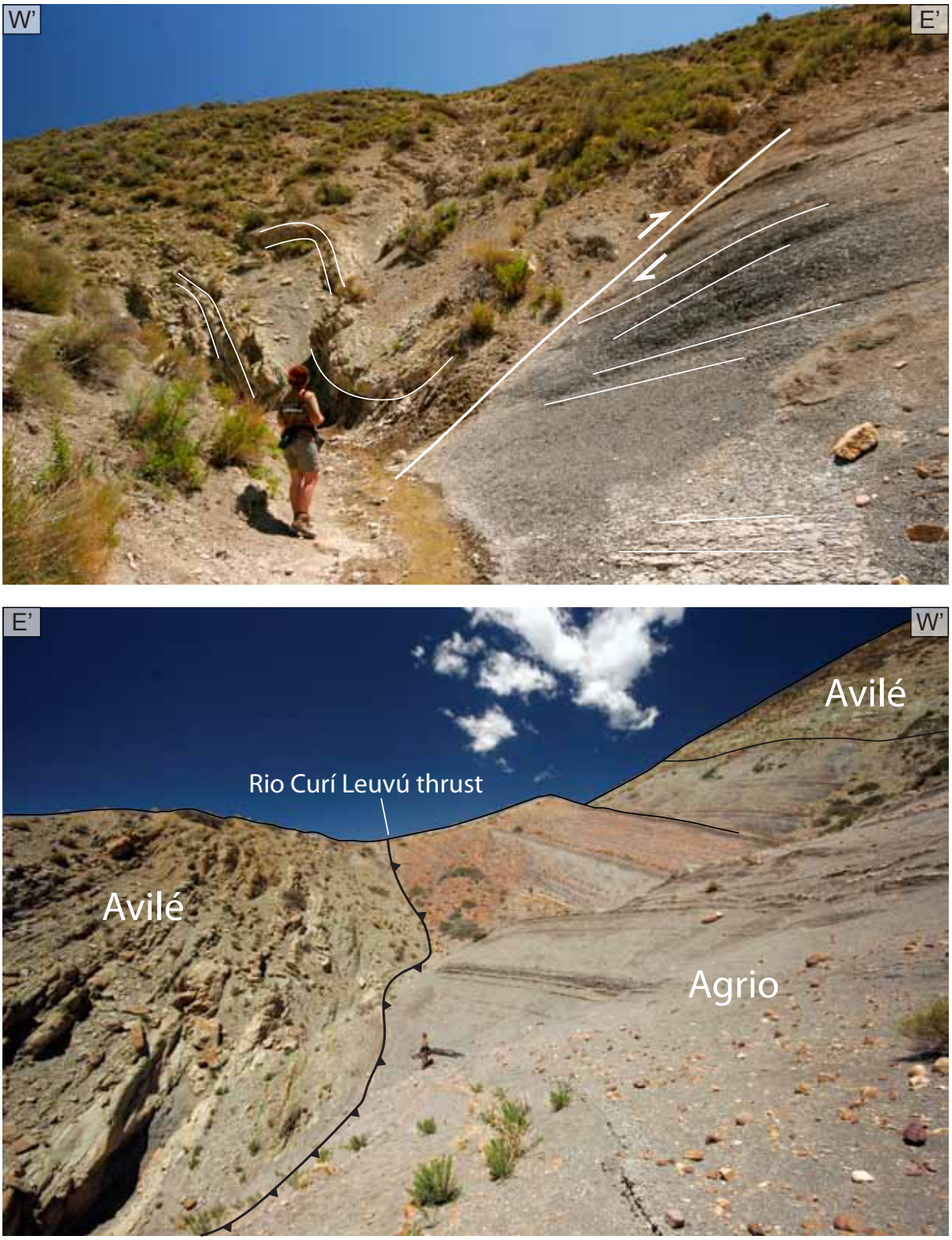

Figure 51: *The N-S oriented Rio Curí Leuvú thrust observed from different perspectives at WP 170-172. The thrust is east-verging and doubles the Avilé sandstone.*

Summary of the field observations

Field data were strategically collected from sedimentary rocks and their contact with magmatic intrusions. One problem incurred was the highly variable bedding in shaly sediments over relatively small distances. Thus, multiple measurements were taken and the most reliable chosen. The field relation between magmatic conduits and sediments is not always clear on outcrop scale. To discriminate between sills and dykes several contacts and the overall structure need to be taken into account. On a local scale, the sills observed were discordant, even though they are concordant overall (Figures 23-35). This is partly due to their intrusion into shaly sediments. The contact planes are often marked by thin chilled margins, where the sediments have been baked by the heat from the magma, and thus appear dark in colour (Figure 24).

Several upper and lower contacts of sills were mapped and could be followed over long distances. The thickness and orientation of dykes made it generally easy to follow them (Figure 36). We consider our field observations and measurements as being robust and are confident in the reconstruction of the structure of the Cerro Negro intrusive complex (Figures 19, 20, 21a-d).

The structure of the Cerro Negro

The plumbing system of Cerro Negro consists of a network of sills and dykes that pierce through sediments. Based on detailed structural field observations several links between different units have been observed (Figures 19, 21a-d):

NS_1 – this is a flat-lying sill that interacts with the topography. Several upper contacts (Figures 23, 24, 27) and one clear lower contact (Figures 25, 26) were measured. Stratigraphically, NS_1 is contained in the Lower Agrio shales and limestones. Our structural observations on the western side and central part of NS_1 suggest that the sub-circular body is connected to the more local patches in the Southwest and that only a thin layer of Agrio limestones covers the upper contact. No clear relationship to the local patches of intrusion with sub-vertical contacts south of NS_1 can be derived from our observations. Measurements along the trace of the sill indicate that the sill has been gently folded in the Cerro Negro anticline.

NS_2 – this conduit is strikingly different in appearance from all other magmatic units. The magmatic rocks making up this sill are strongly altered and deformed in a tight anticline ovoid in shape on map view (Figure 19). None of the other conduits have been so strongly altered or folded. This may suggest that this intrusion is older and possibly different in composition than the others. This hypothesis is not resolved in our study and can only be tested with geochemical analyses and dating, which is beyond the scope of this study. Although the temporal and compositional characteristics of this sill and its relation to NS_1 are not known, this anticline (together with structures further south) helps to constrain the geometry of the central western part, especially of the western unit (WU).

WU – the rocks of this unit are composed of an andesite groundmass with basaltic andesite xenoliths. Despite detailed surveying in the central western part, no contacts of this unit to sediments were observed. Satellite images suggest that the structure is folded similar to NS_2 further north and SWa_1 in the South. These observations

suggest that this magmatic intrusion corresponds to a sill in an eroded anticline. This cannot be said with certainty, as we do not have direct field observations. The link between the WU and other intrusions cannot be resolved from field observations. Comparing the macroscopic appearance of samples from the WU to the NS_2, they do not seem to correspond to the same unit.

SS_1 + SS_3 – both these sills crop out in the same stratigraphic level (Figure 21c). The field relations and measurements suggest that SS_1 and SS_3 represent both sides of the same sill that has been folded in the Cerro Negro anticline (Figures 21c, 45), of which the hinge has been eroded.

SS_2 – Stratigraphically, this sill is emplaced in the Mulichinco Formation close to the base of the overlying Agrio Formation. It crops out almost continuously and has also been folded in the Cerro Negro anticline. SS_2 is locally crosscut by a series of dykes (Figure 31), indicating the relative time of emplacement. SS_2 is andesitic-dacitic in composition (the most evolved sample comes from this unit).

All sills (NS_1, NS_2, SS_1, SS_2, SS_3, WU) have been emplaced in shales within Lower Agrio or at the base of Lower Agrio at the boundary to the Mulichinco Formation. From this we infer that there is a strong stratigraphic control on the emplacement level of the sills. This has been reported from other locations within the Neuquén Basin (*Rosello et al.*, 2002; *Gressier et al.*, 2010).

CU – Several units build the summit of Cerro Negro (Figures 29, 45). The conduits crop out as a sense network of N-S trending dykes, most probably a continuation of the dyke in the South (Figure 36, 44), some folded sills, but also thin layers of Agrio shales and limestones that were observed at the summit (Figure 29). The field relations here are very different from the rest of the field area. The density of the network of sills and dykes is unique, suggesting that the summit of Cerro Negro represents the centre of the Palaeo-Cerro Negro. Due to the steep slopes, the central units are not very well accessible, especially on the western flank of the mountain. Talus slides cover most of the central part. Thus, no clear intrusion geometry can be assigned to these units. They are, however, all constrained to a central Cerro Negro anticline. The dykes are restricted to the hinge zone of the anticline. This geometry has not been described in previous studies. On the contrary, the central units have always been mapped as a circular conduit, rather than a network of sills and dykes (*Zöllner and Amos*, 1973; *Kozlowski et al.*, 1996; *Leanza*, unpublished).

SD – This dyke is also located at the hinge of the Cerro Negro anticline and has a N-S orientation perpendicular to the direction of shortening (E-W). No direct observations between this conduit and the southern sills have been made. However, the orientation of this thick dyke is compatible with the orientation of the network of smaller dykes to the North. No deformation was observed in this conduit, which may be due to its location close to the anticlinal hinge. No crosscutting relations between this dyke and the folded sills have been observed.

Table 1: Waypoints (WP) and corresponding GPS coordinates

WP	°S	°W	m > N.N.	WP	°S	°W	m > N.N.	WP	°S	°W	m > N.N.	WP	°S	°W	m > N.N.	WP	°S	°W	m > N.N.	WP	°S	°W	m > N.N.
1	37.40021	70.23385	851	47	37.10256	70.31922	2113	94	37.19462	70.35028	1122	139	37.17475	70.35068	1212	184	37.18021	70.31099	1577	229	37.15400	70.33223	1476
2	37.25850	70.45705	1098	48	37.10227	70.31839	2071	95	37.19445	70.34619	1176	140	37.17488	70.35148	1197	185	37.17971	70.31105	1588	230	37.15655	70.33373	1416
3	37.13370	70.24388	1653	49	37.10089	70.31662	2035	96	37.19379	70.34634	1177	141	37.17575	70.35232	1192	186	37.17861	70.31136	1572	232	37.15790	70.33454	1401
4	37.12902	70.24136	1611	50	37.10037	70.31595	2023	97	37.19347	70.34612	1181	141	37.19305	70.37336	1041	187	37.17629	70.31162	1534	233	37.15918	70.33607	1367
5	37.13186	70.24734	1608	51	37.09980	70.31200	1998	98	37.19104	70.34696	1183	142	37.14641	70.27359	1445	188	37.17595	70.31181	1532	234	37.15917	70.33663	1358
6	37.09526	70.29472	1675	53	37.10009	70.31101	1977	99	37.18958	70.34809	1140	143	37.15213	70.28794	1457	189	37.17533	70.31038	1533	235	37.15986	70.34104	1321
7	37.10714	70.30706	1764	54	37.10088	70.31272	1975	100	37.18953	70.34874	1130	144	37.14677	70.28926	1475	190	37.17283	70.30897	1597	236	37.16127	70.34325	1298
8	37.10117	70.28899	1730	55	37.10075	70.31248	1971	101	37.19133	70.35385	1101	145	37.14764	70.28754	1461	191	37.17192	70.30737	1624	237	37.16305	70.34529	1282
9	37.10196	70.28541	1742	56	37.10190	70.31239	1947	102	37.19140	70.35545	1096	146	37.15706	70.28574	1433	192	37.17309	70.30688	1562	238	37.11072	70.32699	2189
10	37.11207	70.27539	1638	57	37.08032	70.31635	1572	103	37.19709	70.37132	1048	147	37.15652	70.28137	1391	193	37.17545	70.30428	1500	240	37.11542	70.32737	2275
11	37.15730	70.27649	1387	58	37.08092	70.31609	1595	104	37.17303	70.26961	1354	148	37.16511	70.28460	1354	194	37.10749	70.32789	2095	241	37.12213	70.33052	2506
12	37.14949	70.29112	1506	59	37.08195	70.31591	1637	105	37.17263	70.27067	1342	149	37.16131	70.28190	1367	195	37.10839	70.32811	2133	242	37.12286	70.33032	2496
13	37.06686	70.31892	1387	60	37.08174	70.31474	1633	106	37.17872	70.27040	1337	150	37.16229	70.28157	1369	196	37.10725	70.32629	2068	244	37.13873	70.30866	1814
14	37.05504	70.32287	1355	61	37.08118	70.31392	1640	107	37.15601	70.27568	1379	151	37.17737	70.28189	1329	197	37.10700	70.32446	2035	245	37.13832	70.30884	1826
15	37.05453	70.32263	1355	62	37.08064	70.30710	1647	108	37.16012	70.27871	1369	152	37.30181	70.24629	1308	198	37.10643	70.32461	2035	246	37.13851	70.31427	2071
16	37.19296	70.25350	1418	63	37.08058	70.30634	1640	109	37.16601	70.27971	1364	153	37.05352	70.33183	1326	199	37.10586	70.33050	2010	247	37.13540	70.31701	2227
17	37.18398	70.26096	1444	64	37.07976	70.30669	1637	110	37.18346	70.28824	1345	154	37.06130	70.32305	1371	199	37.10586	70.33050	2010	248	37.12957	70.32231	2371
18	37.08634	70.29804	1669	65	37.09075	70.30301	1785	111	37.17616	70.27916	1320	155	37.06801	70.32243	1426	200	37.10527	70.33197	1956	249	37.12754	70.32708	2523
19	37.07608	70.36232	1226	66	37.09093	70.31083	1810	112	37.16580	70.28983	1378	156	37.07909	70.32027	1513	201	37.10096	70.33618	1849	250	37.12808	70.32464	2438
20	37.09899	70.37928	1182	67	37.09059	70.31152	1812	113	37.16575	70.29030	1389	157	37.08050	70.31988	1522	202	37.10252	70.32703	1970	251	37.08674	70.32555	1658
21	37.13036	70.38467	1092	68	37.08210	70.31594	1642	114	37.16147	70.29638	1487	158	37.05383	70.34524	1298	203	37.10231	70.32628	1977	252	37.09389	70.32534	1762
22	37.18495	70.26009	1450	69	37.06138	70.36109	1234	115	37.16347	70.29277	1422	159	37.07740	70.36777	1216	204	37.10133	70.32490	1975	253	37.09683	70.32411	1866
23	37.11017	70.31019	1827	70	37.07910	70.35698	1284	116	37.16335	70.28237	1372	160	37.08604	70.36777	1249	205	37.10225	70.32459	2015	254	37.10152	70.32954	1826
24	37.11148	70.31056	1861	71	37.07913	70.35679	1299	117	37.15547	70.27993	1393	161	37.09963	70.35892	1453	206	37.10370	70.32442	2051	255	37.10047	70.33058	1774
25	37.11493	70.30791	1861	72	37.07867	70.35611	1295	118	37.15395	70.27988	1399	162	37.09745	70.35188	1552	207	37.13114	70.37871	1161	256	37.09848	70.33264	1722
26	37.11659	70.31654	1988	73	37.07930	70.35597	1257	119	37.15369	70.27954	1406	163	37.10011	70.35826	1471	208	37.14037	70.33317	1695	257	37.09647	70.33423	1630
27	37.11713	70.31873	2015	74	37.07940	70.35530	1262	120	37.15443	70.28122	1412	164	37.09451	70.36146	1359	209	37.13756	70.32657	1857	258	37.08969	70.33728	1521
28	37.11765	70.31933	2031	75	37.07930	70.35485	1273	121	37.15370	70.28178	1417	165	37.09994	70.37751	1181	210	37.13854	70.32583	1864	259	37.08547	70.33725	1493
29	37.11829	70.32066	2077	76	37.07919	70.35367	1292	122	37.18471	70.37287	1064	166	37.10625	70.39695	1188	211	37.13855	70.32335	1957	260	37.08498	70.33883	1451
30	37.11914	70.32111	2098	77	37.08034	70.35349	1282	123	37.18506	70.37139	1062	167	37.23612	70.36683	1003	212	37.13976	70.32110	1969	261	37.12658	70.29293	2053
31	37.11952	70.32263	2139	78	37.08148	70.35400	1289	124	37.18282	70.36957	1108	168	37.21956	70.37829	1042	213	37.13825	70.31884	2045	262	37.12735	70.29347	2043
32	37.11972	70.32267	2146	79	37.08213	70.35400	1297	125	37.18114	70.36840	1124	169	37.21766	70.37144	1003	214	37.13729	70.31647	2135	263	37.12868	70.29414	2023
33	37.11921	70.32352	2175	80	37.08259	70.35345	1319	126	37.18059	70.36778	1125	170	37.12172	70.39731	1121	215	37.14053	70.32198	1962	264	37.12596	70.29271	2033
34	37.11458	70.31883	1996	81	37.08333	70.35473	1346	127	37.17999	70.36831	1112	171	37.15843	70.39890	1086	216	37.14101	70.32459	1915	265	37.12537	70.29410	1968
35	37.11027	70.31452	1885	82	37.07875	70.35975	1245	128	37.17740	70.36946	1111	172	37.15789	70.39990	1083	217	37.14073	70.32523	1898	266	37.12074	70.29378	1895
36	37.11034	70.31410	1880	83	37.05802	70.36766	1221	129	37.17668	70.36473	1140	173	37.19532	70.38763	1031	218	37.14019	70.32523	1866	267	37.08540	70.28498	1799
37	37.11037	70.31375	1877	84	37.20285	70.37852	1010	130	37.17466	70.36022	1151	174	37.18258	70.29284	1368	219	37.13735	70.34084	1646	268	37.09037	70.28554	1779
38	37.11043	70.31341	1870	85	37.15956	70.44301	1232	131	37.17652	70.35494	1172	175	37.18227	70.29584	1385	220	37.12773	70.34287	1870	269	37.15542	70.31035	1667
39	37.11007	70.31291	1853	86	37.08006	70.35660	1268	132	37.17815	70.35245	1196	176	37.18227	70.29683	1390	221	37.12137	70.34461	1873	270	37.15671	70.31160	1725
40	37.10544	70.30901	1817	87	37.19862	70.37314	1017	133	37.17818	70.35219	1203	177	37.18275	70.29786	1398	222	37.12022	70.34831	1887	271	37.15748	70.31249	1747
41	37.10438	70.31074	1870	88	37.19877	70.37035	1104	134	37.17796	70.35181	1195	178	37.18564	70.30160	1459	223	37.11554	70.35014	1789	272	37.15348	70.31848	1726
42	37.10505	70.31651	1967	89	37.19827	70.36913	1101	135	37.17795	70.35050	1204	179	37.18693	70.30199	1514	224	37.11130	70.34427	1814	273	37.15071	70.32177	1751
43	37.10516	70.31694	1980	90	37.19695	70.36510	1094	136	37.17794	70.35013	1211	180	37.18711	70.30179	1502	225	37.11138	70.34546	1804	274	37.15374	70.32115	1750
44	37.10480	70.31844	2029	91	37.19576	70.36175	1089	137	37.17759	70.34939	1219	181	37.18107	70.31057	1577	226	37.13365	70.34023	1778	275	37.16104	70.31882	1660
45	37.10361	70.32057	2068	92	37.19507	70.35466	1092	138	37.17487	70.34846	1243	182	37.18082	70.31103	1587	227	37.14538	70.32595	1716	276	37.16098	70.31667	1667
46	37.10313	70.32215	2070	93	37.19436	70.35141	1103	138	37.17487	70.34846	1243	183	37.18048	70.31092	1586	228	37.15194	70.33144	1529				

Sample description and petrography

The subvolcanic rocks of the Cerro Negro intrusive complex were characterised as (hornblende) andesites based on qualitative petrographic observations of minerals and textures and especially based on their major element geochemistry. A full list with sample locations can be found in Table 1.

In hand-specimen all samples are fine-grained, mesocratic and consist of plagioclase and one or more mafic minerals, mostly of amphibole of variable size and colour. The variance in colour (grey-green to orange-red) is due to variations in composition, degree of weathering and grain size. Some samples have dark, inclusions consisting of hornblende. In thin section, all samples contain phenocrysts of plagioclase (plag), hornblende (hbl), orthopyroxene (opx), clinopyroxene (cpx), Fe-Ti oxides as well as minor amounts of secondary biotite (bt) and chlorite (chl) growing at the expense of plagioclase and pyroxene. Accessory phases include zircon (zr), and apatite (ap) (Figure 52). In general, being intermediate in composition (chemically more evolved than basalts), andesites have lower solidus and liquidus temperatures than basalts. The presence of primary hornblende and possibly biotite indicates that magmas contained some H_2O, i.e. were hydrous. All samples display a plagioclase-pyric texture, where plagioclase is the most abundant mineral and shows oscillatory zoning. Additionally, most samples show signs of weak hydrothermal alteration, possibly the result of interaction of the magma with the surrounding shales and limestones.

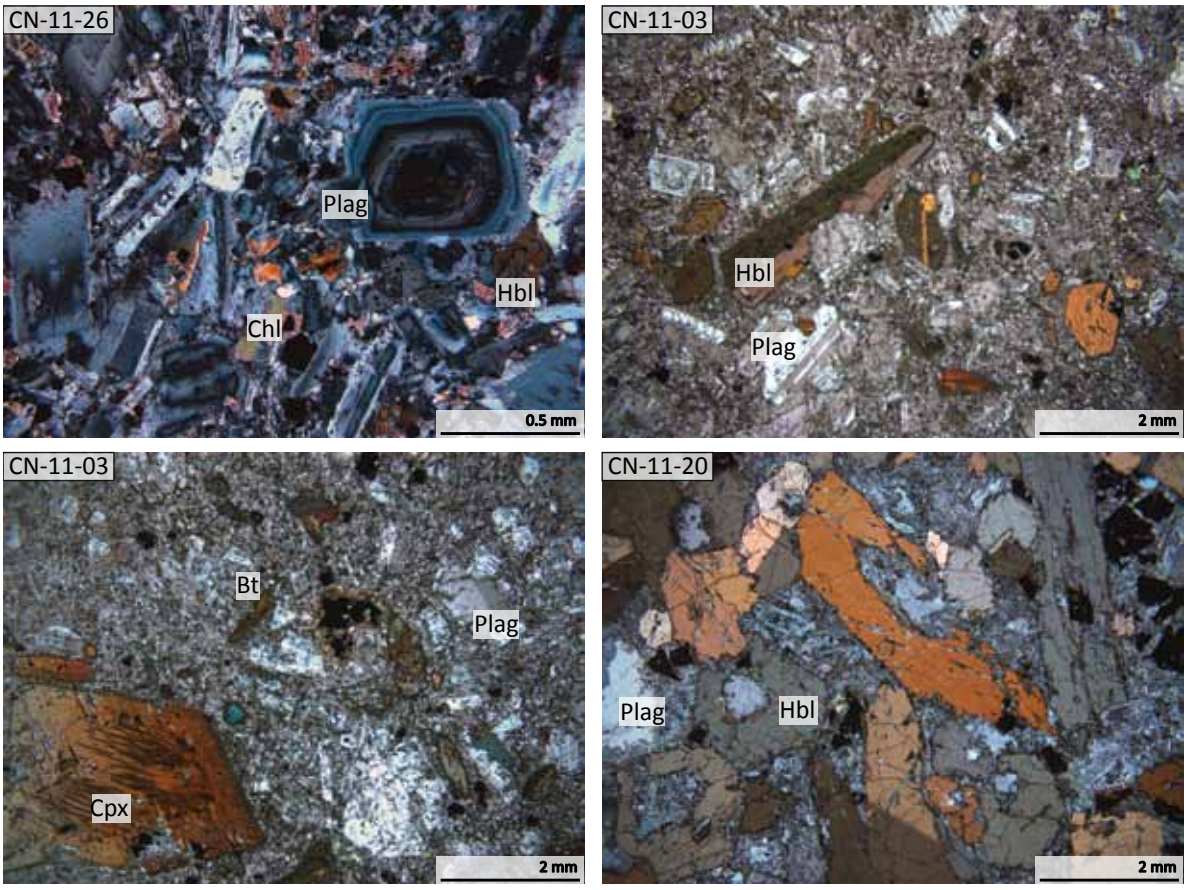

Figure 52: *Representative thin sections of subvolcanic rocks from Cerro Negro. The typical assemblage consists of plag + hbl + opx + cpx + Fe-Ti oxides ± ap, zr, ilm, secondary bt, chl. Sample CN-11-26: WU, sample CN-11-03: SS$_1$, sample CN-11-20 dyke from CU.*

Thin sections have been grouped into units based on their field relations and macroscopic appearance. Representative samples (underlined) from each unit are described in the following. PPL denotes plane-polarised light and XPL stands for cross-polarised light.

Northern sills (NS)

Samples: **NS_1**: CN-11-01, CN-11-07, CN-11-08, **NS_2**: CN-11-09, CN-11-12

Sample CN-11-01 was collected from an andesitic sill (NS_1) in the northeastern part of the field area (Figure 53; WP 18), close to the contact to Agrio limestones. The sample contains zoned plagioclase phenocrysts and pyroxenes, Fe-Ti oxides, zircon and some yellow-brown radial chlorite is are most likely secondary. Secondary phases have grown at the expense of plagioclase. These are calcite or sericite that are possibly due to hydrothermal alteration. Especially pyroxene is strongly altered (Figure 53b). A fine-grained matrix made of plagioclase and alteration products (calcite, epidote, sericite) surrounds phenocrysts.

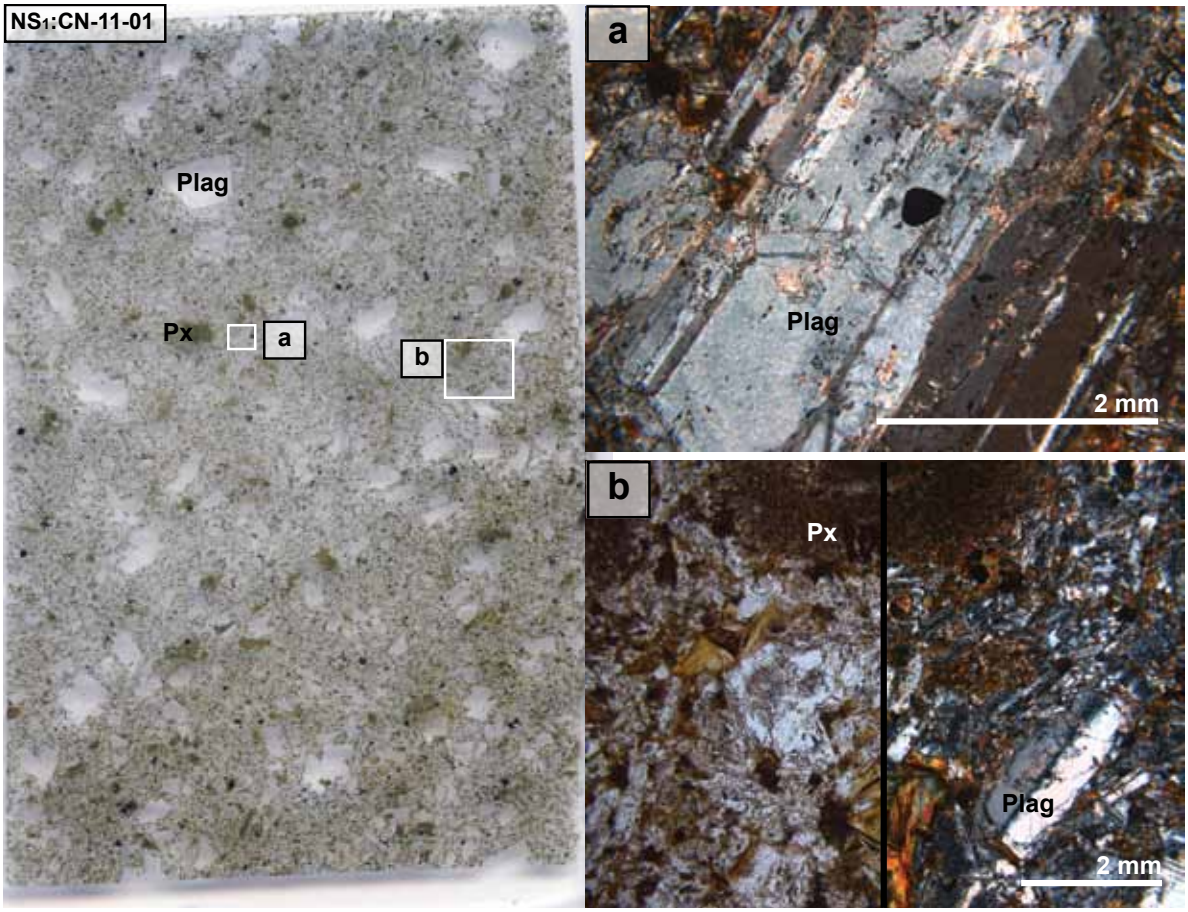

Figure 53: *Sample CN-11-01. Thin section (left) displays the typical assemblage of NS_1. It consists of plag + hbl + px + Fe-Ti oxides + zrn and secondary minerals.* ***a)*** *XPL: twinned and weakly zoned plagioclase transformed into probable hydrothermal calcite or sericite. Small euhedral grains of Fe-Ti oxides (opaque) are present in the fine-grained groundmass and also in phenocrysts.* ***b)*** *PPL/XPL: another alteration product, chlorite, is yellow to brown in colour and radial in shape. The most altered phase is pyroxene that is completely transformed into pseudomorphs of small opaque grains, most likely the iron originally contained in the pyroxene.*

Sample CN-11-12 was collected from a strongly altered sill (NS_2) in the northwestern part of the field area (Figure 54; WP 164), and is orange to light brown in appearance. The grain size is smaller and equigranular compared to the other samples. No euhedral minerals are present. The sample is largely replaced and contains remnants of plagioclase, amphibole and pyroxene, as well as Fe-Ti oxides. Most likely secondary phases make up big parts of the matrix.

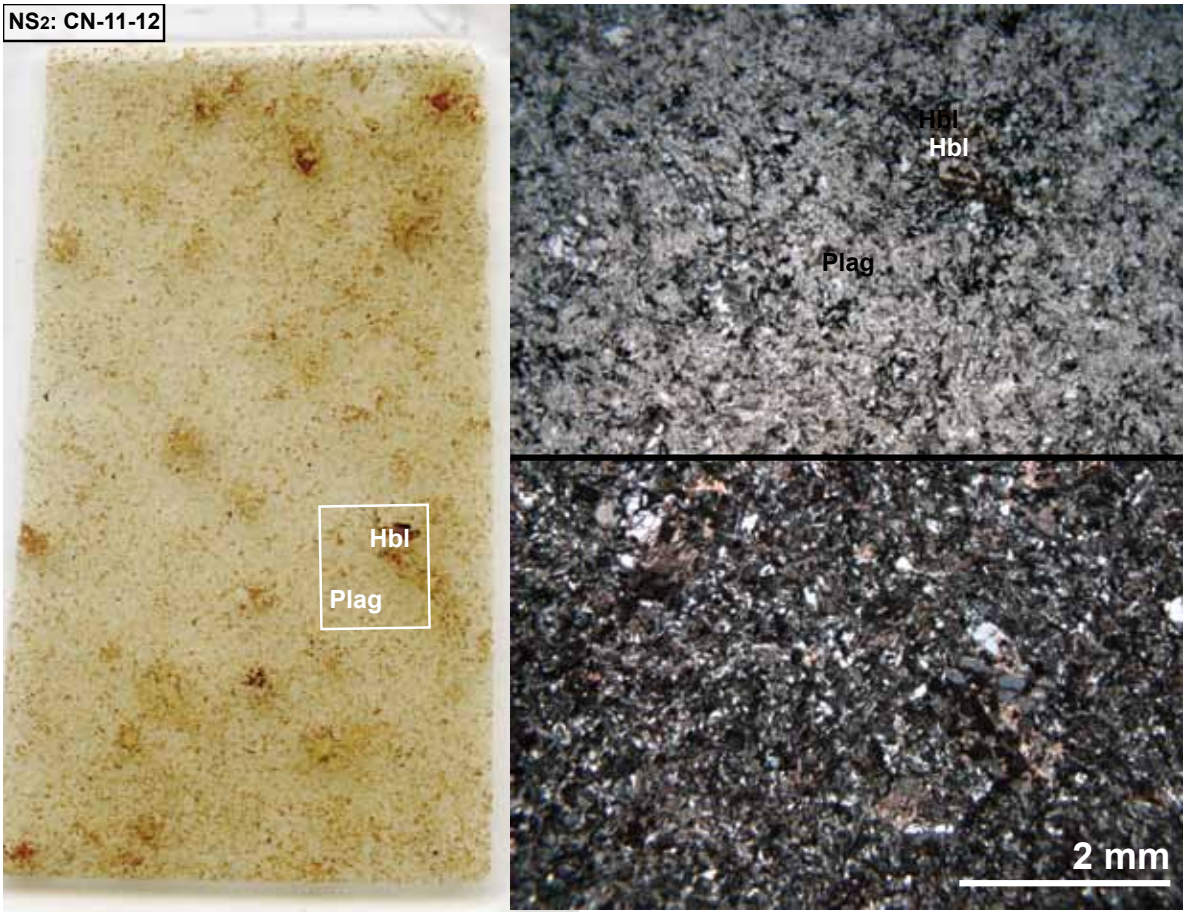

Figure 54: *Sample CN-11-12. Thin section (left) displays the grade of alteration of NS_2. It consists of remnants of plag + hbl + px + Fe-Ti oxides + secondary minerals. Micrograph (right) PPL (top right): fine-grained, equigranular matrix of plagioclase and remnants of hbl and secondary phases. XPL (bottom right): alteration products include biotite and chlorite. Most phases are completely transformed into pseudomorphs.*

Southern sills (SS)

Samples: **SS_1**: CN-11-03, CN-11-30, CN-11-31, CN-11-32, **SS_2**: CN-11-18, CN-11-19, CN-11-39, **SS_3**: CN-11-17

Sample CN-11-03 (Figure 55; WP 32) was collected from a sill (SS_1) on the eastern flank of Cerro Negro. It is andesitic in composition and contains phenocrysts of zoned plagioclase, dark brown-green hornblende, twinned orthopyroxene and clinopyroxene. All of them are in a fine-grained matrix. Accessory phases include zircon, sulfides (e.g. yellow tinted pyrite (FeS_2)), Ti-Fe oxides, such as shiny metallic ilmenite ($FeTiO_3$) and grey magnetite (Fe_3O_4) that were identified under reflected light. Pale-green chlorite was observed as thin alteration rims around clinopyroxene.

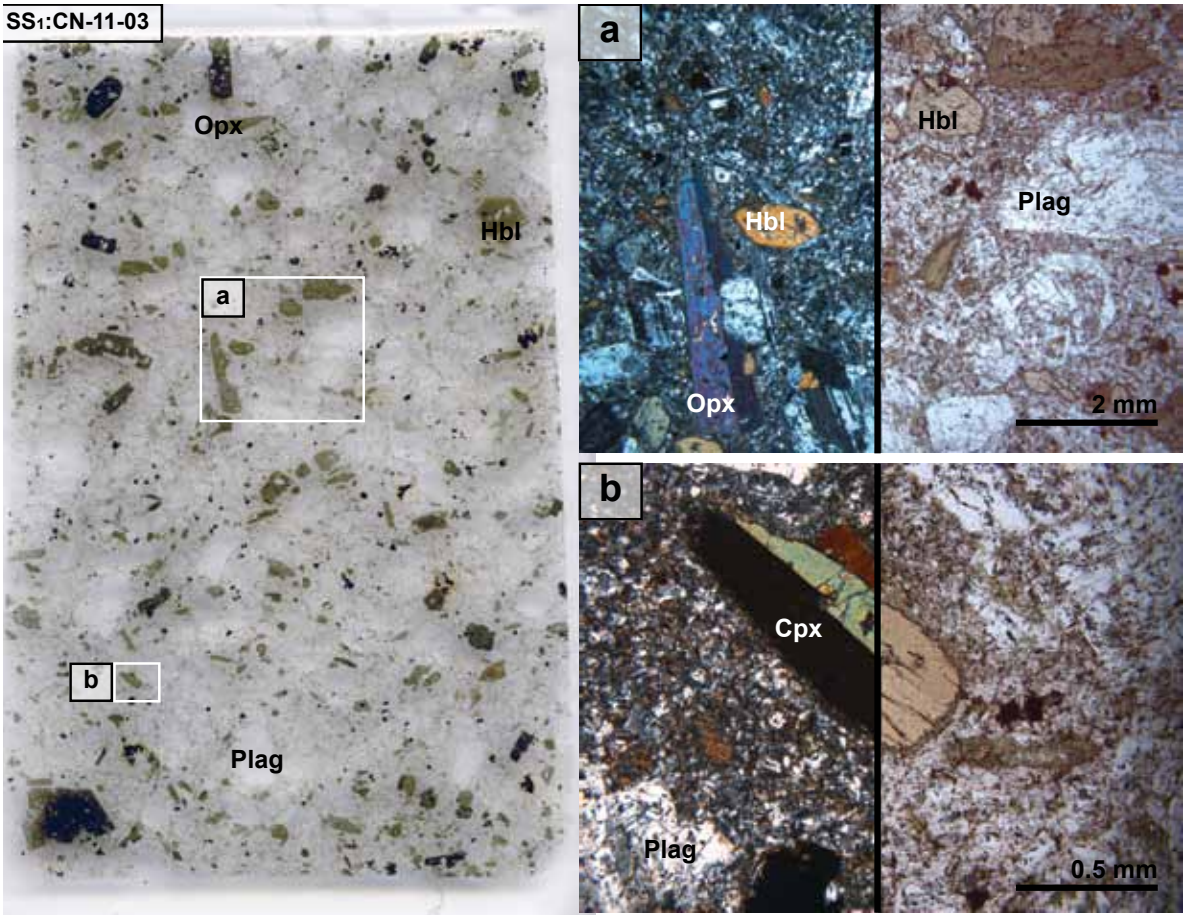

Figure 55: *Thin section (left) of sample CN-11-03 displays the characteristic mineral assemblage of SS_1: plag +cpx + opx + hbl + Fe-Ti oxides + zrn and secondary minerals.* ***a, b)*** *XPL/PPL: phenocrysts of twinned cpx and opx, hbl and weakly zoned plagioclase are surrounded by a fine-grained groundmass. Small euhedral grains of Fe-Ti oxides (opaque) are present. Phenocrysts are slightly altered as marked by thin alteration rims of chlorite around pyroxenes and calcite or sericite in plagioclase.*

Sample CN-11-18 (Figure 56; WP 212) was taken from a sill (SS_2) on the western flank of Cerro Negro. It contains phenocrysts of zoned and twinned plagioclase, dark brown-yellow hornblende, pyroxene, Fe-Ti oxides and abundant secondary minerals as biotite and chlorite. The latter are found in the matrix and also as rims around phenocrysts.

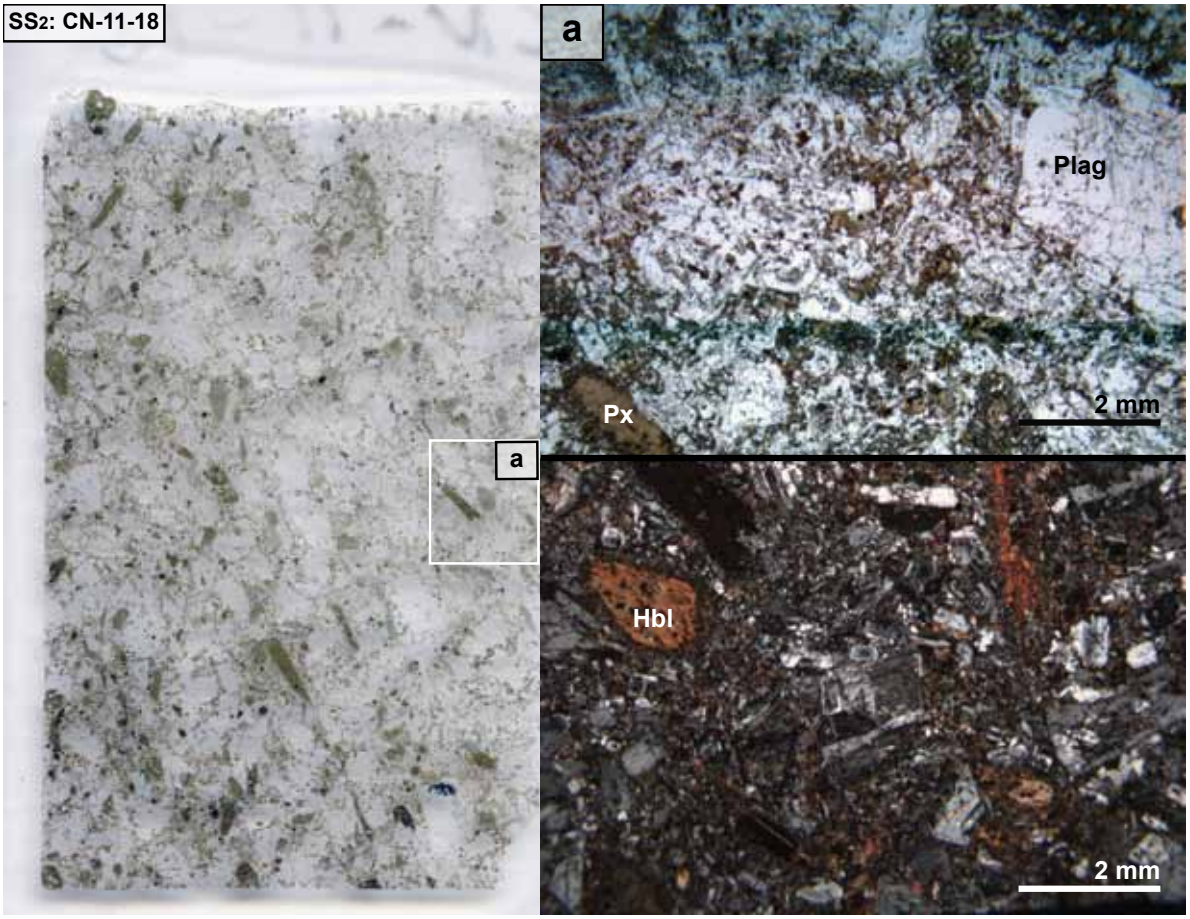

Figure 56: *Thin section (left) of sample CN-11-18 displays the characteristic mineral assemblage of SS_1: plag +cpx + opx + hbl + Fe-Ti oxides and secondary minerals.* ***a)*** *XPL/PPL: phenocrysts of twinned cpx and opx, hbl and weakly zoned plagioclase is surrounded by a fine-grained groundmass. Small euhedral grains of Fe-Ti oxides (opaque) are present. Phenocrysts are slightly altered as marked by thin alteration rims of chlorite around pyroxenes and calcite or sericite in plagioclase.*

Sample CN-11-17 was collected from SS_3, on the western flank of Cerro Negro (Figure 57; WP 208). It contains fine-grained enclaves of mainly plagioclase and minor hornblende and orthopyroxene, surrounded by a medium-grained matrix that consists of plagioclase, hornblende and twinned ortho- and clinopyroxene. Furthermore, small grains of Fe-Ti oxides and zircon are present in this sample.

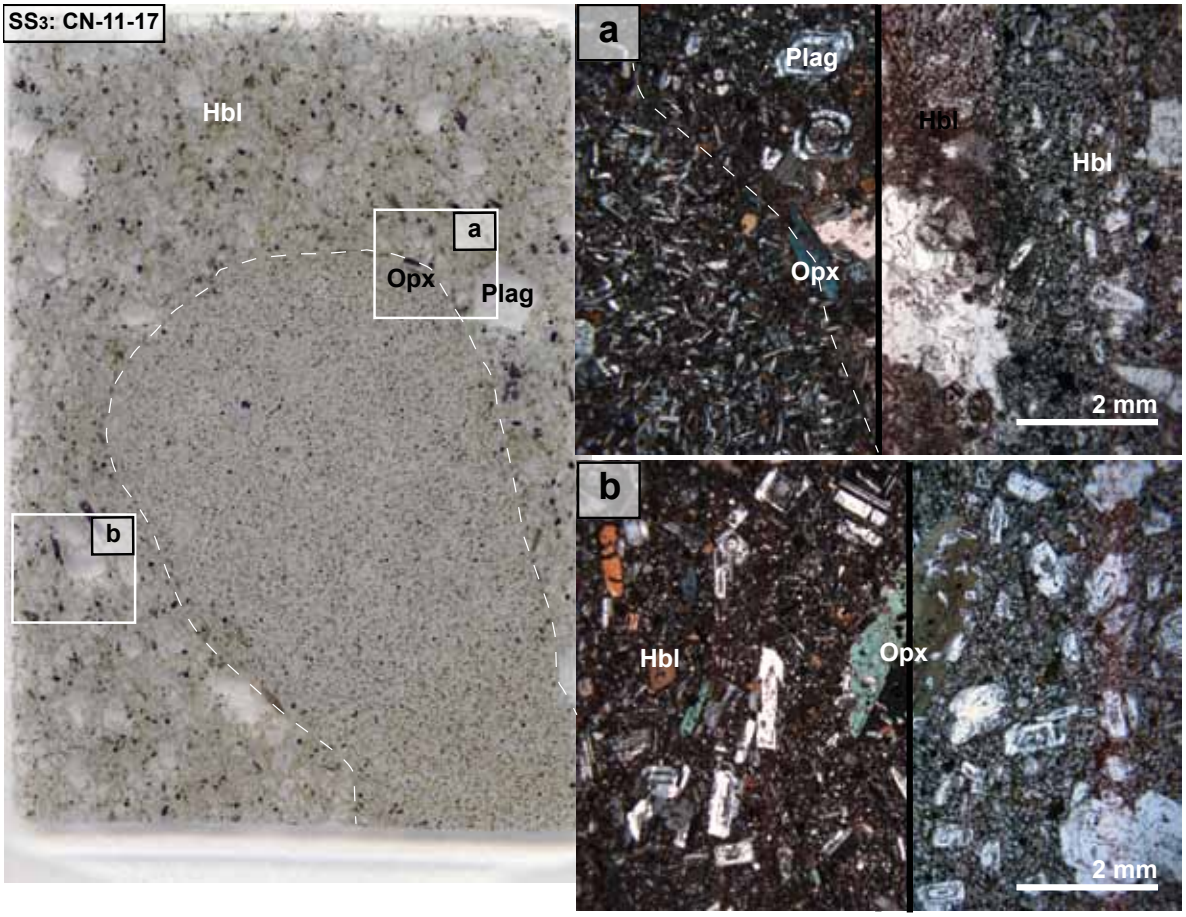

Figure 57: *Thin section (left) of sample CN-11-17 shows a fine-grained enclave in a medium-grained matrix. The characteristic mineral assemblage of SS_3 consists of plag +cpx + opx + hbl + Fe-Ti oxides + zrn and secondary minerals.* ***a)*** *XPL/PPL: fine-grained enclave made of plagioclase, hornblende and orthopyroxene phenocrysts at the contact to twinned clinopyroxe and orthopyroxene, hornblende and weakly zoned plagioclase that are surrounded by a fine-grained groundmass. Alteration is pronounced at the contact to the enclave.* ***b)*** *XPL/PPL: a twinned opx phenocryst shows poikilitic replacement textures.*

Central units (CU)

Samples: CN-11-14, CN-11-15, CN-11-20, CN-11-27, CN-11-28, CN-11-29

Sample CN-11-14 was collected from a small plug, which is part of a network of andesitic dykes north of the Central units (Figure 58; WP 194). Phenocrysts of plagioclase, hornblende, twinned ortho- and clinopyroxene are surrounded by a fine-grained matrix of mainly plagioclase, which is relatively fresh. Furthermore, small grains of Fe-Ti oxides and zircon are present in this sample.

Very thin alteration rims surround hornblende and pyroxene phenocrysts. Plagioclase phenocrysts are generally quite altered as well. Both observations indicate the effect of late alteration processes.

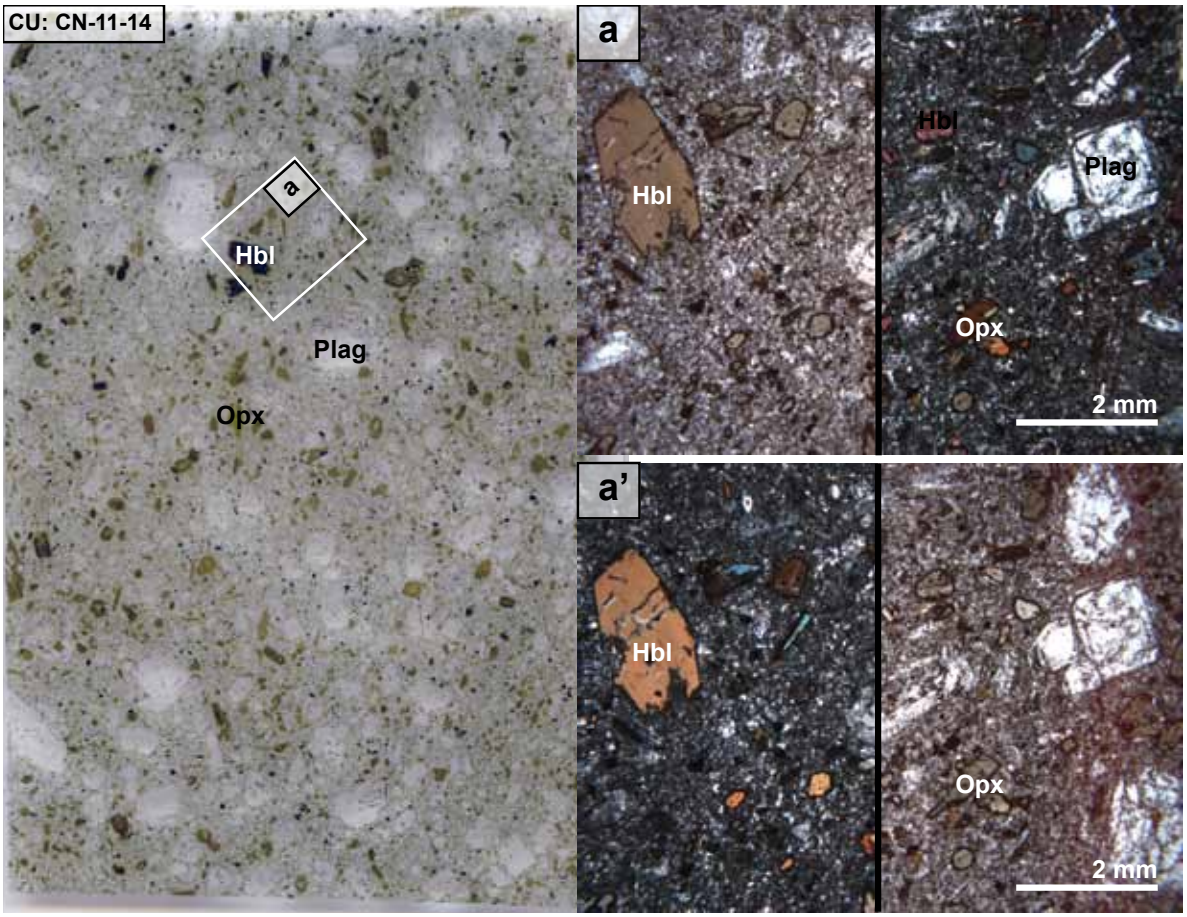

Figure 58: *Thin section (left) of sample CN-11-14 displays the mineral assemblage of the dykes of the CU: plag +cpx + opx + hbl + Fe-Ti oxides + zrn and secondary minerals.* ***a)*** *PPL/XPL: Relatively big hornblende phenocrysts, orthopyroxene, and weakly zoned plagioclase are surrounded by a fine-grained groundmass of plagioclase and small euhedral grains of Fe-Ti oxides (opaque). Secondary alteration products are also present. Phenocrysts are slightly altered. Thin alteration rims of chlorite surround pyroxenes, whereas plagioclase is locally replaced by calcite or sericite.*

Sample CN-11-20 was taken from a dyke south of the Central units that builds the summit of the Cerro Negro (Figure 59; WP218) and crosscuts SS_2 at two localities. Phenocrysts of twinned clinopyroxene and amphibole are surrounded by a fine-grained matrix of mainly plagioclase, which is relatively altered. The phenocrysts are surrounded by very thin alteration rims. Additionally, sulfide melt inclusions trapped along grain boundaries were observed. Plagioclase phenocrysts are smaller than in the other samples. Mafic enclaves consisting of more or less euhedral minerals (cpx, hbl) are made of bigger crystals than the surrounding groundmass. Furthermore, the amount of Fe-Ti oxides is relatively high and mainly concentrated in the mafic enclaves. No zircon was found in this sample. Overall the enclaves look like they are in equilibrium with their surroundings.

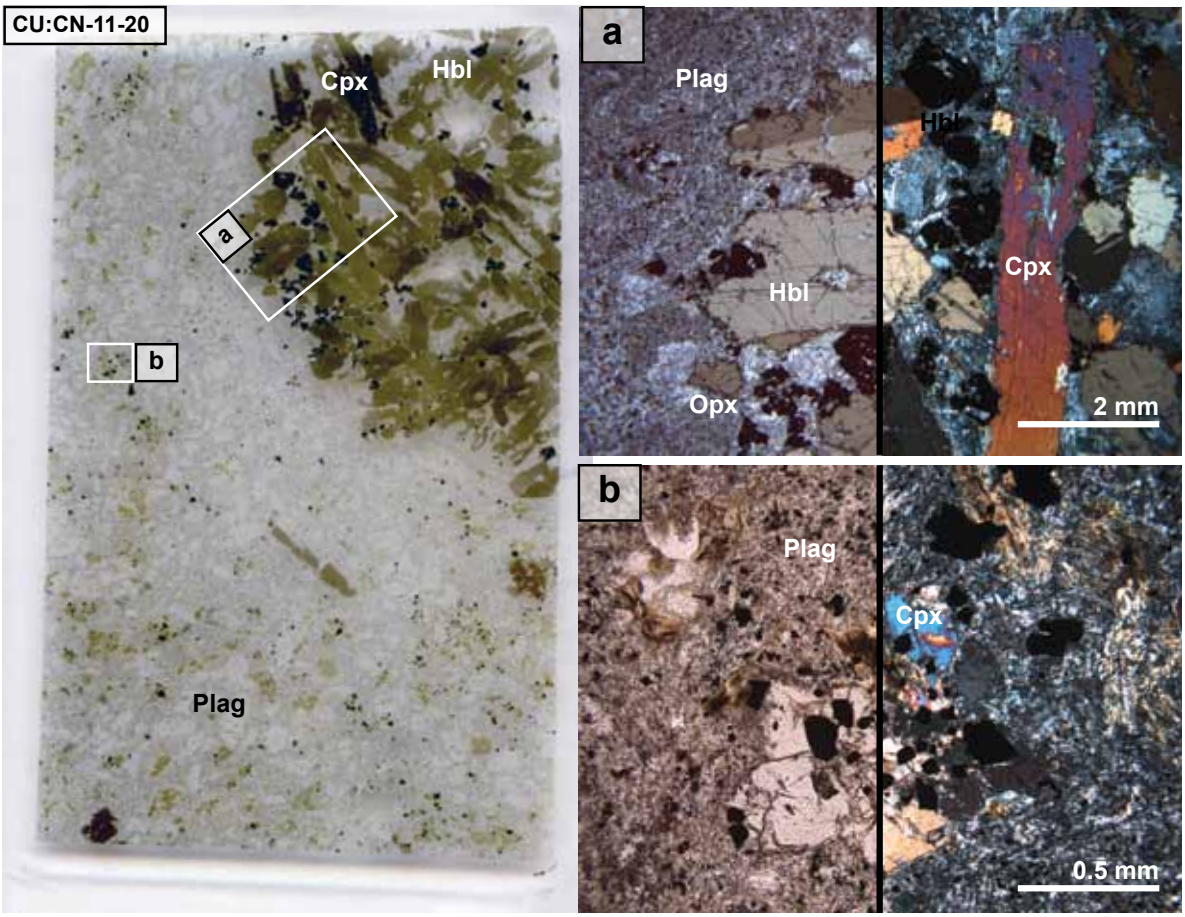

Figure 59: *Thin section (left) of sample CN-11-20 displays the characteristic mineral assemblage of the dykes of the CU that have mafic enclaves. These consist of mm-sized pyroxene and amphibole with abundant Fe-Ti oxides. The groundmass is made of plag +cpx + opx + hbl + Fe-Ti oxides + zrn, as well as secondary minerals.* ***a, b)*** *PPL/XPL: Relatively big hornblende phenocrysts, orthopyroxene, and weakly zoned plagioclase are surrounded by a fine-grained groundmass of plagioclase, small euhedral grains of Fe-Ti oxides (opaque), and secondary alteration products. Pyroxene phenocrysts are slightly altered and surrounded by thin alteration rims of chlorite.*

Western unit (WU)

Samples: CN-11-21a+b, CN-11-23, CN-11-25, CN-11-26

Sample CN-11-26 was collected from a conduit on the western side of Cerro Negro (Figure 60; WP225). Most of the sample consists of twinned and zoned plagioclase phenocrysts. Furthermore, this sample contains pyroxene that is strongly resorbed. The fine-grained groundmass is relatively altered and consists of an aggregate of plagioclase, Fe-Ti oxides and secondary chlorite, biotite and epidote. Other samples from this unit are similar in appearance, but show variable degrees of alteration. Additionally, samples CN-11-21a+b and CN-11-23 have fine-grained, altered enclaves consisting of plagioclase, pyroxene and oxides in a coarser-grained matrix made of the same phases.

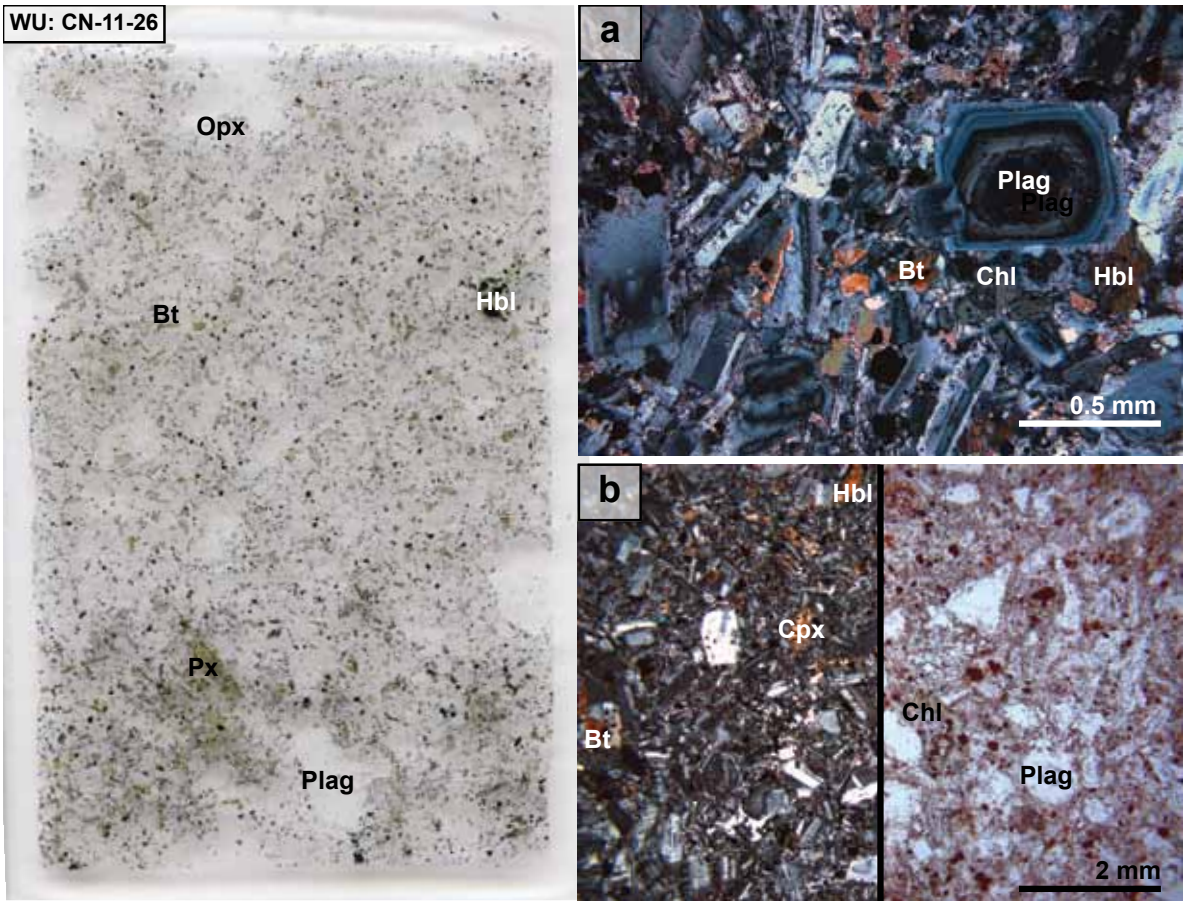

Figure 60: *Thin section (left) of sample CN-11-26 displays the characteristic mineral assemblage of the magmatic rocks collected on the western flank of Cerro Negro.* ***a)*** *XPL: minerals present are plag + hbl + cpx + chl + bt. Twinned and zoned plagioclase phenocrysts make up most of the sample. Additionally, pyroxene phenocrysts are strongly resorbed.* ***b)*** *XPL/PPL: the groundmass consisting of fine-grained plagioclase is relatively altered. Chlorite and biotite have been identified as secondary phases.*

Southern dyke (SD)

Sample: CN-11-13

This sample originates from a thick dyke (SD) south of Cerro Negro (Figure 61; WP 185) and consists of phenocrysts of twinned and zoned plagioclase, twinned hornblende, pyroxene, Fe-Ti oxides, secondary chlorite and biotite. Accessory zircon is present. Several plagioclase xenocrysts with alteration rims are also present. This suggests that xenocrysts were attacked by melt after mixing (Figure 61a). The groundmass consists of medium to fine-grained plagioclase and alteration products (calcite, sericite, epidote?). Several mafic enclaves containing xenocrystic material are present (Figure 61b).

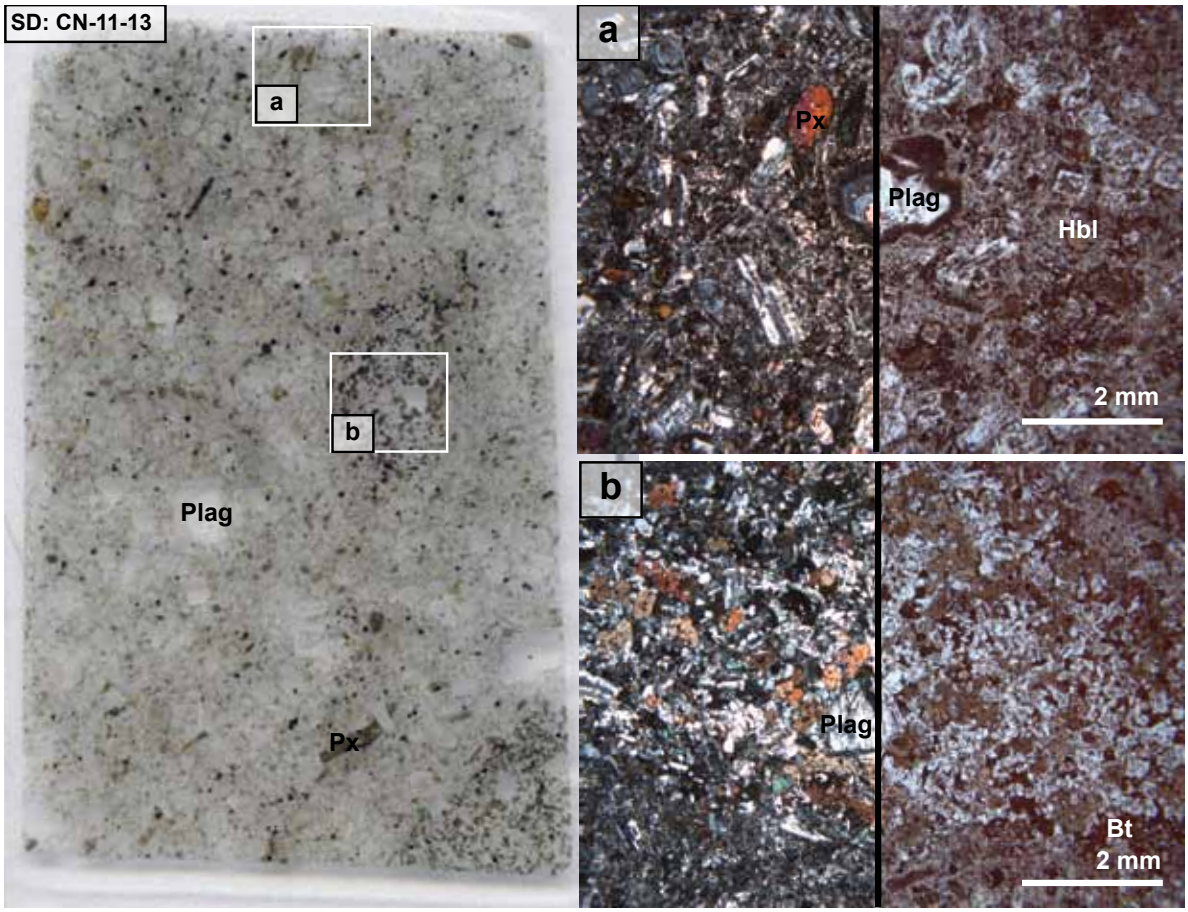

Figure 61: *Thin section (left) of sample CN-11-13 displays mineral assemblage of the SD: plag + hbl + px + Fe-Ti oxides + zrn + alteration products.* ***a)*** *XPL/PPL: corroded plagioclase xenocrysts with alteration rims suggest that xenocrysts were attacked by melt during mixing.* ***a, b)*** *XPL/PPL: the groundmass consists of medium to fine-grained plagioclase and alteration products (calcite, sericite, epidote?). Several mafic enclaves containing mafic xenocrystic material are present.*

Geochronology

A total of 20 analyses of zircon grains were obtained from multiple fractions in samples CN-11-01, CN-11-03, CN-11-13 and CN-11-14. Sample CN-11-20 did not yield any zircon. Samples CN-11-01 and CN-11-03 are from sills, whereas CN-11-13 and CN-11-14 are from dykes. The main motivation for dating the sills and dykes was to confirm and strengthen the observed crosscutting relationships, where at several localities dykes crosscut folded sills, and to resolve the mutual temporal relationship. The sample locations as well as U-Pb data for all analyses and sample characteristics and ages are provided in Table 2. Numbers behind grains refer to number of analysis in Table 2 and Figure 68. In general, the obtained zircon ages are relatively consistent and can be interpreted as a reliable indicator for the age of the Cerro Negro magmatic rocks. Some difficulties arose from the small sample sizes, especially when dating single grains. Both multigrain fractions and single grains were analysed. The latter rule out the possibility of obtaining mixed ages by combining primary magmatic and xenocrystic grains that might have been picked up by the magma on its way up. Single grain measurements, however, are less precise, as the available amounts of Pb are close to those of the blank, and the blank correction has an increasingly pronounced effect with decreasing sample size. Moreover, small amounts of Pb in samples also affect negatively the counting statistics. A few zircon grains have been lost during sample handling.

Sample characteristics and morphology of zircon grains

Sample CN-11-01 was collected from an andesitic sill in the northwestern part of the field area (WP 18), close to the contact to Agrio limestones.

At this locality, the sill is locally discordant and mineralisation has been observed at the contact. The zircon grains from sample CN-11-01 are pale pink and display three morphologies (Figure 62): (a) clear, long prismatic, uneven surfaces, locally affected by resorption, (b) clear, subrounded, uneven surfaces with gas or melt inclusions, locally affected by resorption, and (c) clear, short prismatic, uneven surfaces, inclusion-free, strongly affected by resorption and corrosion. The grains range from 200-300 µm in size and are overall more strongly resorbed than zircon grains from other samples.

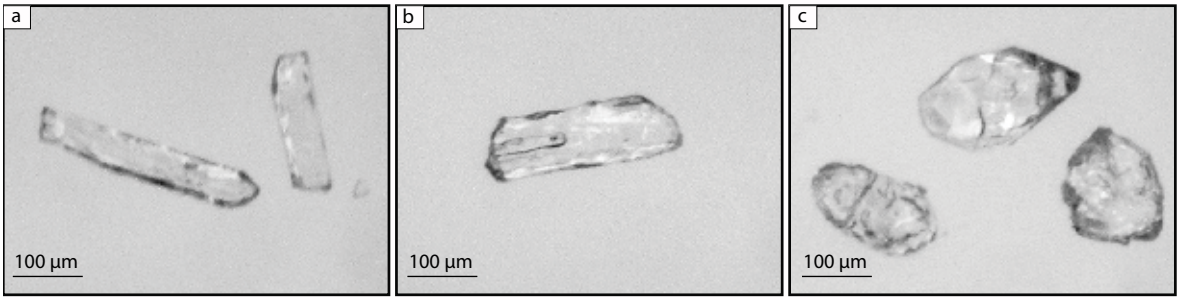

Figure 62: *Different zircon morphologies present in sample CN-11-01 after annealing and partial dissolution:* ***(a)*** *clear, long prismatic, uneven surfaces, locally affected by resorption,* ***(b)*** *clear, semi-prismatic, uneven surfaces with fluid or melt inclusions, locally affected by resorption, and* ***(c)*** *clear, short prismatic, uneven surfaces, inclusion-free, strongly affected by resorption.*

Three single grains (1-3) and a fraction of two grains (4) have been analysed. The Concordia diagram for this sample (Figure 68) displays the four data points (1-4), which are concordant. Three of them overlap, giving a Concordia age of 11.681 ± 0.053 Ma. The fourth data point (4) indicates a slightly older age (12.031 ± 0.67 Ma).

Sample CN-11-03 has been collected from an andesitic sill on the eastern flank of Cerro Negro (WP 32), close to the contact with Agrio limestones. It yielded different zircon morphologies (Figure 63): (a) clear, short, inclusion-free prisms, (b) clear prisms with fluid or melt inclusions, (c) clear, broken, inclusion-free prisms, and (d) clear, long, inclusion-free prisms. The size of the zircon grains ranges from 150 µm in fraction (a) to 400 µm in the other fractions.

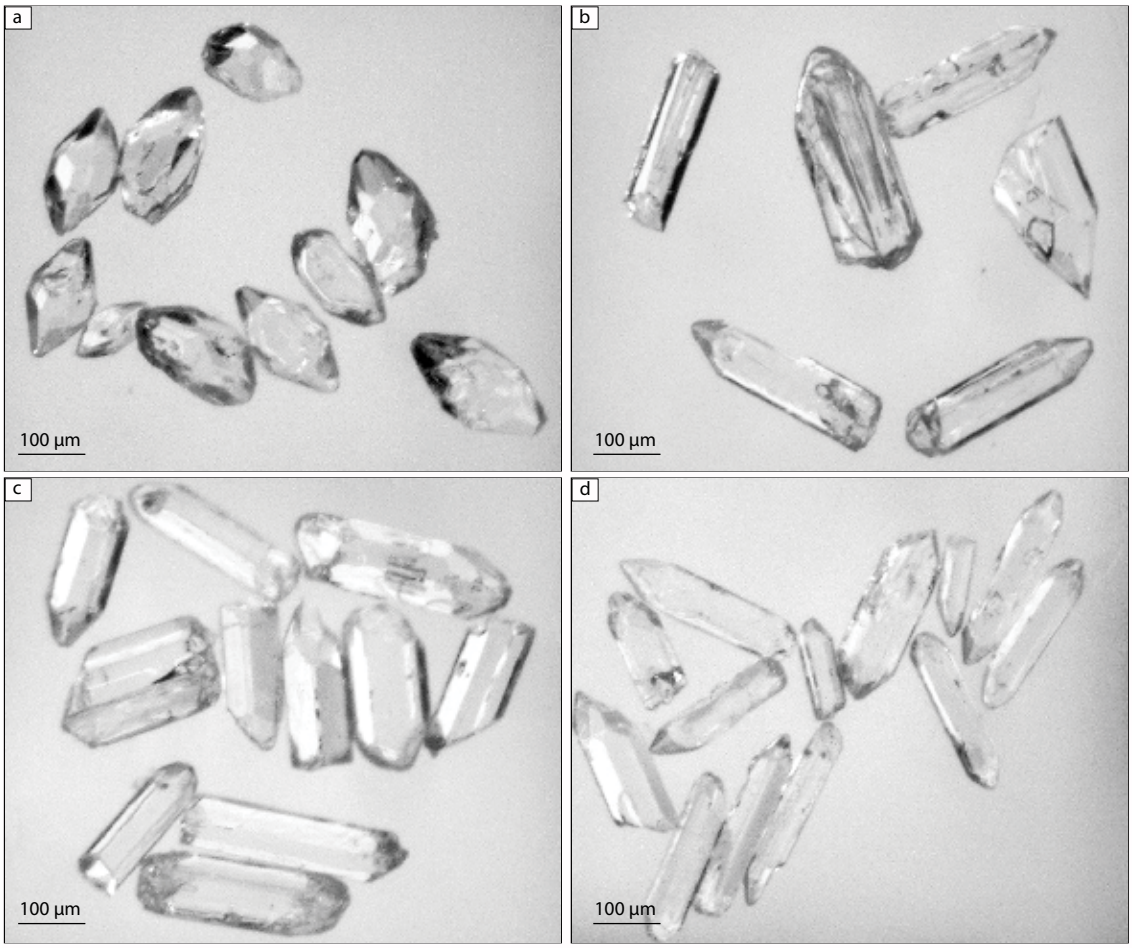

Figure 63: *Different zircon morphologies present in sample CN-11-03 after chemical abrasion:* ***(a)*** *clear, short, inclusion-free prisms, (b) clear prisms with gas or melt inclusions,* ***(c)*** *clear, broken, inclusion-free prisms and* ***(d)*** *clear, long, inclusion-free prisms.*

CL images of a selection of zircon grains similar to fractions (b)-(d) show well developed oscillatory zoning and two of the grains observed in thin section display sector zoning. Cores are not evident except perhaps in the grain shown in Figure 64a. Quantitative SEM analysis of several inclusions revealed the presence of K-feldspar, albite and apatite inclusions showing that the zircons started growing in the magma at an advanced stage of crystallisation.

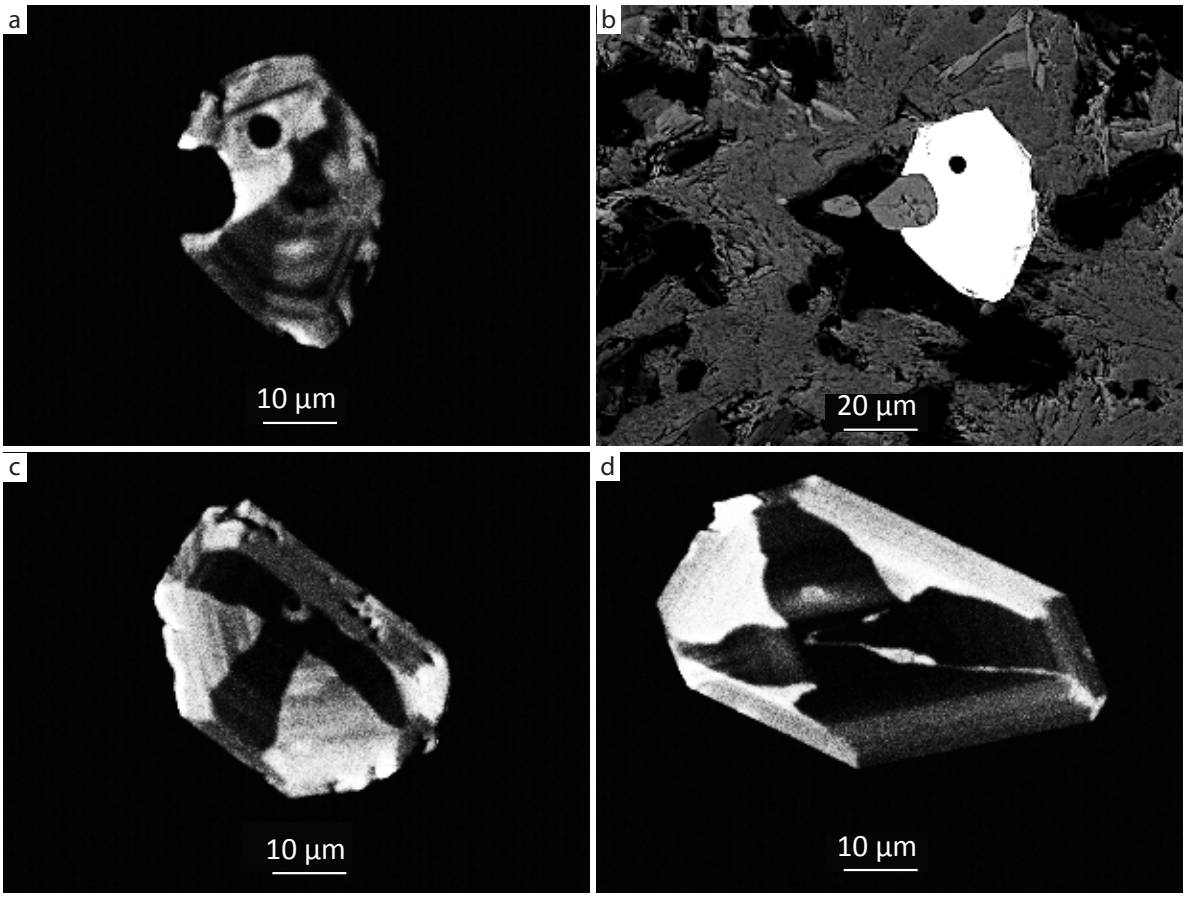

Figure 64: *CL* ***(a, c, d)*** *and BSE* ***(b)*** *images of zircon grains from sample CN-11-03. Oscillatory and sector zoning are visible in CL images.*

A first set of four multigrain fractions resulted in two concordant analyses (7, 8) indicating an age of about 11.4 Ma, and two discordant analyses (9, 10) with older apparent ages (Figure 68). To verify the reason for the heterogeneity three single grains were analysed (5, 6, 11). Because of the small amount of Pb present, the precision is very reduced, but single grain analyses confirm nonetheless the pattern. Two points (5, 6) are overlapping the concordant analyses (7, 8), and one grain (11) yielding an older age. The pattern suggests mixing of a magmatic population with traces of xenocrystic material. A discordia line defined by all seven analyses has an upper intercept at about 1400 Ma, indicating derivation of the xenocrysts from Mesoproterozoic crust. The lower intercept age of 11.56 ± 0.18 Ma is identical to the Concordia age of 11.483 ± 0.074 Ma defined by the most precise data points alone (7, 8). The latter is interpreted to represent the most reliable age, also as the amount of common Pb is smallest.

Sample CN-11-13 originates from a dyke south of Cerro Negro (WP 185). The zircon grains in sample CN-11-13 have two distinct morphologies: (a, b) clear, long, inclusion-free prisms, (c) clear, broken prisms with gas or melt inclusions. The biggest grains are up to 500 µm in size (Figure 65).

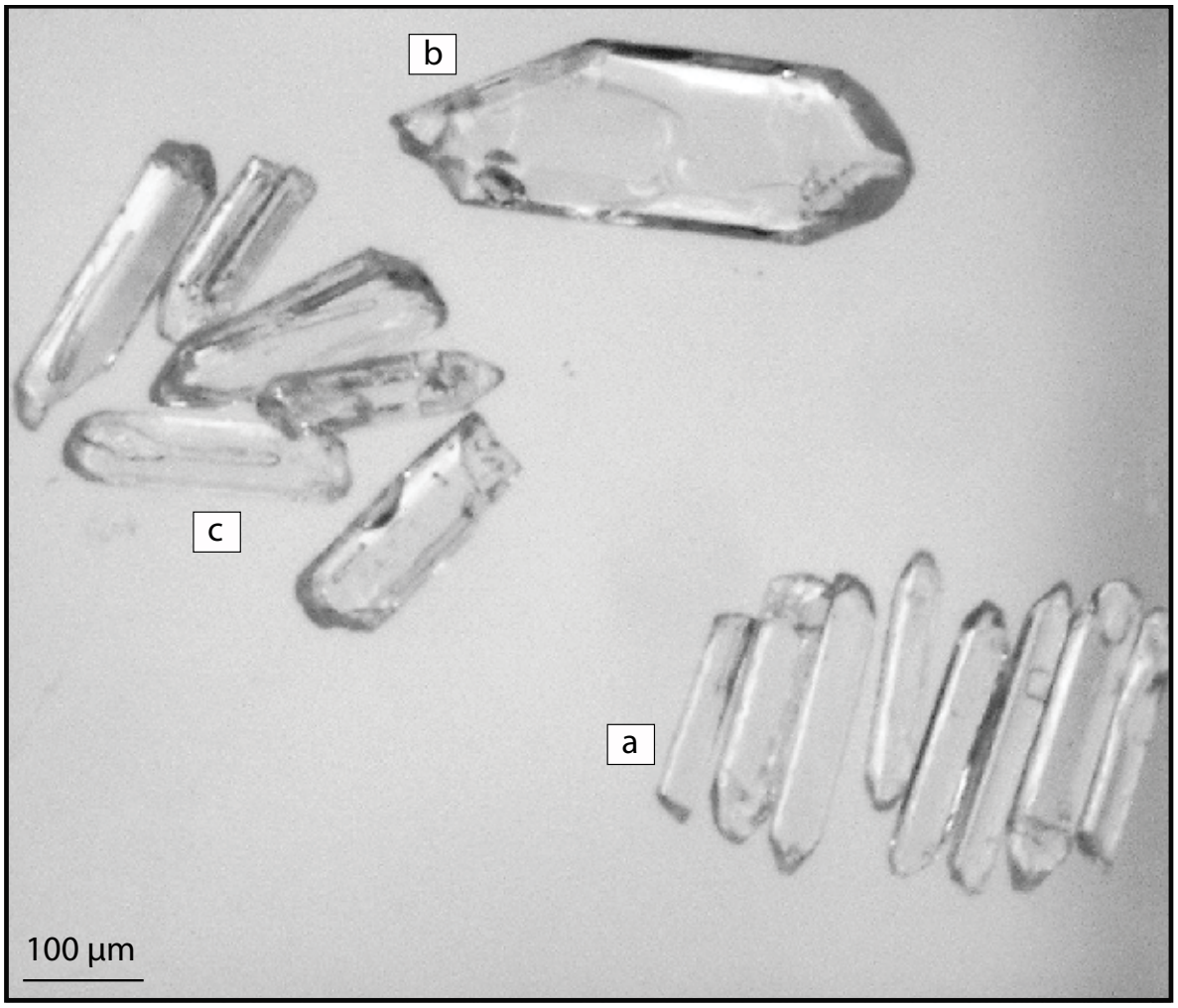

Figure 65: *Three different zircon morphologies present in sample CN-11-13 after chemical abrasion:* ***(a, b)*** *clear, long, inclusion-free prisms,* ***(c)*** *clear, broken prisms with gas or melt inclusions.*

Cathodoluminescence of prismatic crystals shows well-developed growth zoning and no evidence of cores (Figure 66). The zoning patterns are due to fluctuating trace element concentrations in the parent magma and indicate that the grains are primary magmatic.

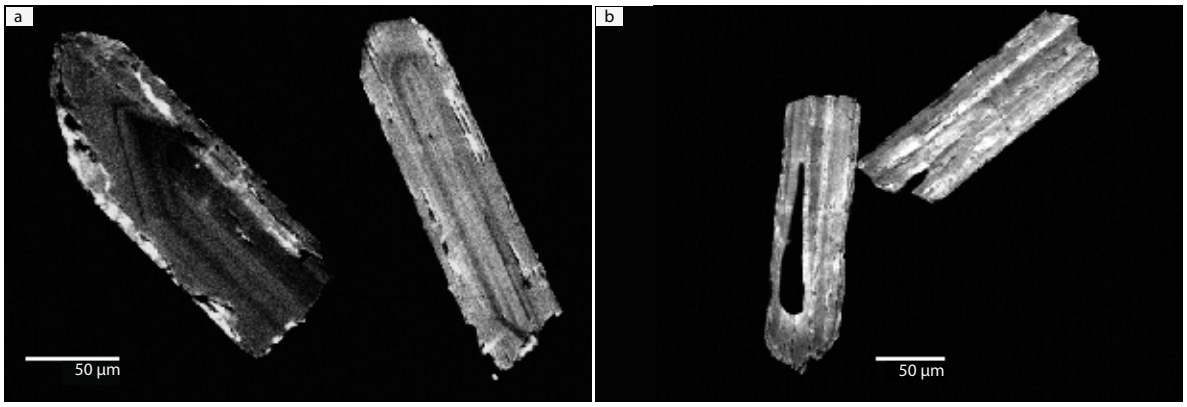

Figure 66: ***(a)*** *CL image of zircon grains with oscillatory zoning from sample CN-11-03, note edges from polishing.* ***(b)*** *CL image of zircon grains with inclusions from sample CN-11-13.*

Data collected from this sample show a variation in age from 9.03-13.18 Ma. All data points are concordant, but only three points (15, 16, 17) with small precision overlap. Unfortunately, the quality of the analyses and their Pb 206/204 ratios are low, especially the analyses giving the oldest and youngest dates. The high amount of common Pb may be related to contamination during sample handling. It is therefore not quite evident whether the apparent age variation reflects heterogeneity of the population or whether it is affected by some analytical biases. The best analyses are points 13 and 14. Data point 14 with the best Pb 206/204 ratio gives a Concordia age of 11.514 ± 0.082 Ma, which is considered the best estimate for emplacement of the dyke (Figure 68). Data point 13, obtained from a single grain, has a similar Pb 206/204 ratio, and good precision. It gives a Concordia age of 10.922 ± 0.098 Ma. The best age estimate of 11.5-10.9 Ma is based on these two points (13, 14).

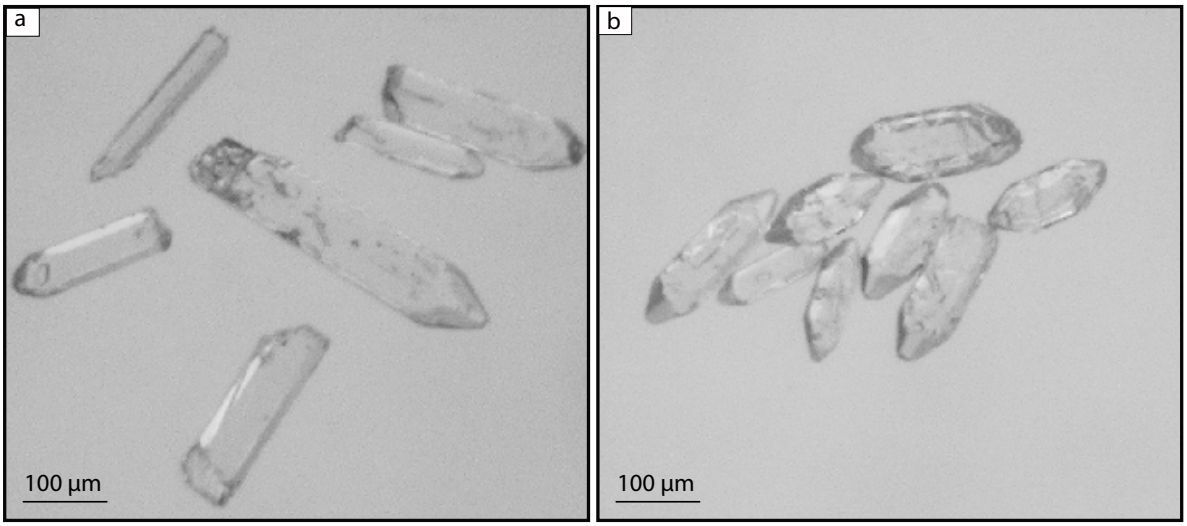

Figure 67: *Two different zircon morphologies present in sample CN-11-14 after chemical abrasion:* ***(a)*** *clear, long, prismatic grains with smooth surfaces, inclusions and corrosion at edges after chemical abrasion and* ***(b)*** *clear, short, prisms with irregular surfaces and inclusions.*

Sample CN-11-14 has been collected from a small plug, which is part of a network of andesitic dykes north of the Cerro Negro summit (WP 194). The sample yielded zircons with two morphologies (Figure 67): (a) clear, long, prismatic grains with smooth surfaces and inclusions (and subsequent corrosion at the edges after chemical abrasion) and (b) clear, short prisms with irregular surfaces and inclusions. The average size of these grains ranges from 200-400 µm.

Data obtained from three fractions (18-20) are concordant, but not overlapping. A Concordia age for all three points cannot be calculated due to the slight variations in age ranging from 11.35-11.51 Ma. Some of these variations may be due to analytical factors. The short-prismatic crystals (20) are slightly older than the long prisms (19), possibly indicating the presence of some cores. Analysis 19 has the highest precision and defines a Concordia age of 11.504 ± 0.046 Ma, whereas analysis 18 gives a Concordia age of 11.39 ± 0.05 Ma based on a single grain. A compromise age of 11.42 ± 0.14 Ma was calculated from these points (18, 19) (Figure 68), and is considered to date magmatic crystallisation of the plug.

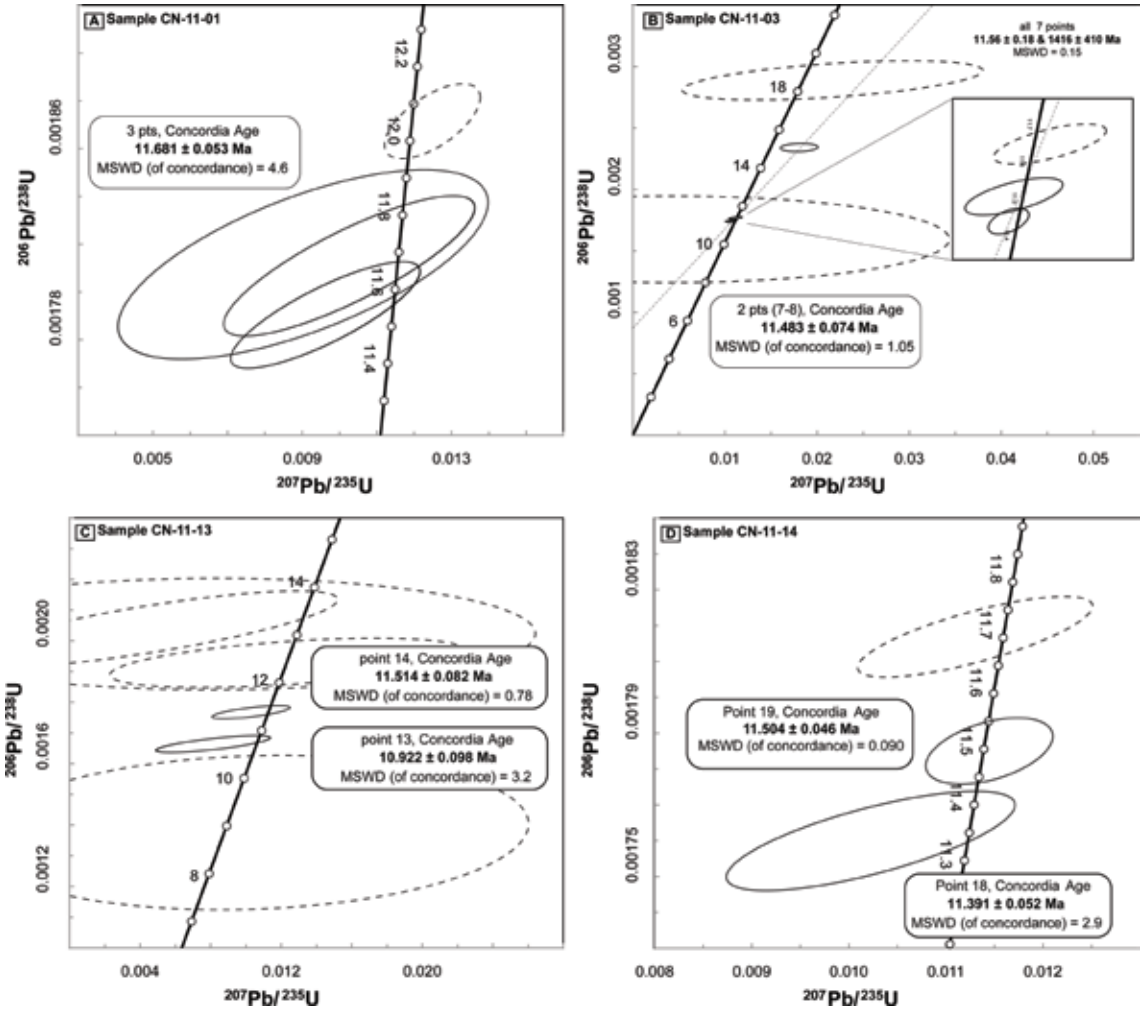

Figure 68: *Concordia plots for zircons from sills (CN-11-01, CN-11-03) and dykes (CN-11-13, CN-11-14) from the Cerro Negro Magmatic Complex. Ellipses indicate the 2σ uncertainty. Dashed ellipses were not used for Concordia age calculation. MSWD = mean square of weighted deviates.*

Zircon was chosen for dating, as it is one of the most robust phases. Inheritance of zircon grains was observed in one sample (CN-11-03, Figure 68), but accounted for by grouping zircon grains accordingly and by running multiple analyses of euhedral populations. Thus, we are confident that our final ages were not biased by dissolving inherited grains together with primary magmatic grains. We consider the absolute ages obtained from different zircon populations as robust indicators for the time of magma emplacement.

Table 2: Zircon U-Pb data, Cerro Negro intrusive complex

No.	Properties	Weight	Pbt	U	Th/U	Pbcom	Pbcom	206/204	207/235	2 sigma	206/238	2 sigma	rho	207/206	2 sigma	207/235	206/238	2 sigma
		[ug]	[ppm]	[ppm]		[ppm]	[pg]			[abs]		[abs]			[abs]	[Ma]	[Ma]	[abs]
	(a)	(b)	(b)	(b)	(c)	(d)	(d)	(e)	(f)	(f)	(g)	(f)	(f)	(g)	(f)	(f)	(g)	(f)
	Sill CN-11-01																	
1	1 gr, clear, resorbed	5	0.17	99	0.25	0.00	1.1	69.7	0.0097	0.0020	0.00178	0.00002	0.82	0.0397	0.0080	9.8	11.55	0.11
2	1 gr, clear, incl., broken prism, resorbed	1	0.62	392	0.00	0.00	1.1	58.2	0.0104	0.0027	0.00180	0.00002	0.83	0.0418	0.0105	10.5	11.68	0.15
3	1 gr, clear, resorbed	3	0.14	76	0.49	0.00	1.1	41.6	0.0091	0.0040	0.00180	0.00003	0.66	0.0368	0.0157	9.2	11.68	0.20
4	2 gr, clear, long broken prims	5	0.48	238	0.65	0.00	1.4	120.7	0.0126	0.0010	0.00186	0.00001	0.63	0.0490	0.0038	12.7	12.06	0.08
	Sill CN-11-03																	
5	1 gr, clear, broken prism	1	15	174	0.00	15.31	17.0	19.5	0.0094	0.0331	0.00131	0.00053	0.02	0.0523	0.1843	9.5	8.55	3.39
6	1 gr, clear, incl, broken prism	1	3	86	1.31	3.10	5.0	20.3	0.0046	0.0245	0.00163	0.00028	0.00	0.0205	0.1106	4.7	10.57	1.80
7	> 10 gr, clear, broken prisms	45	0.17	86	0.67	0.00	1.0	434.6	0.0112	0.0002	0.00176	0.00000	0.50	0.0462	0.0008	11.3	11.45	0.03
8	6 gr, clear prisms, incl	27	0.16	86	0.57	0.00	1.4	198.5	0.0113	0.0005	0.00177	0.00001	0.64	0.0462	0.0020	11.4	11.52	0.04
9	10 gr, clear, short prisms	32	0.19	86	0.51	0.03	3.0	122.4	0.0118	0.0006	0.00180	0.00001	0.66	0.0476	0.0023	11.9	11.66	0.04
10	> 10 gr, clear, long prisms	36	0.66	99	0.42	0.42	17.0	49.5	0.0186	0.0016	0.00235	0.00003	0.12	0.0573	0.0050	18.7	15.24	0.17
11	1 gr, clear, broken prism, partly resorbed	1	2	133	0.00	1.47	3.4	25.4	0.0222	0.0132	0.00288	0.00013	0.50	0.0558	0.0320	22.3	18.68	0.82
	Dyke CN-11-13																	
12	6 gr, clear, long euhedral prisms	10	3.04	69	21.62	2.31	24.7	21.3	0.0106	0.0127	0.00148	0.00020	0.11	0.0521	0.0619	10.7	9.03	1.29
13	1 gr, clear, pale pink, broken prism, partly resorbed	1	1	656	0.40	0.00	2.0	52.3	0.0085	0.0026	0.00167	0.00002	0.75	0.0370	0.0110	8.6	10.83	0.14
14	5 gr, clear, incl.	10	0.29	96	0.90	0.09	2.9	54.8	0.0106	0.0018	0.00177	0.00002	0.70	0.0435	0.0070	10.7	11.48	0.11
15	1 gr, clear, broken prism	1	0	119	0.53	0.00	1.2	30.1	0.0127	0.0082	0.00192	0.00006	0.48	0.0479	0.0300	12.8	12.49	0.41
16	1 gr, clear, incl, long euhedral prism	1	2	116	0.75	1.50	3.5	22.7	0.0084	0.0148	0.00202	0.00014	0.00	0.0303	0.0533	8.5	13.08	0.93
17	1 gr, clear, broken prism	12	0.39	28	0.00	0.35	6.1	25.6	0.0049	0.0086	0.00203	0.00010	0.78	0.0177	0.0301	5.0	13.18	0.63
	Dyke CN-11-14																	
18	1 gr, clear, incl, prism	1	2	952	0.70	0.00	1.4	92.1	0.0103	0.0012	0.00175	0.00001	0.73	0.0426	0.0048	10.4	11.35	0.071
19	6 gr, clear, incl, long euhedral prisms	8	1.31	486	0.53	0.40	5.2	102.3	0.0115	0.0005	0.00177	0.00001	0.45	0.0470	0.0021	11.6	11.51	0.047
20	8 gr, clear, incl, short euhedral prisms	9	0.34	180	0.49	0.00	1.9	114.8	0.0113	0.0010	0.00180	0.00001	0.76	0.0456	0.0037	11.4	11.71	0.058

a) main features of analyzed zircons. All zircons treated with chemical abrasion (Mattinson, 2005). incl=inclusions

b) weight and concentrations are known to better than 10%, except for those near and below the ca. 1 ug limit of resolution of the balance.

c) Th/U model ratio inferred from 208/206 ratio and age of sample

d) Pbc = total common Pb in sample (initial + blank)

e) raw data, corrected for fractionation and spike

f) corrected for fractionation, spike, blank (206/204=18.3; 207/204=15.555) and initial common Pb (based on Stacey and Kramers, 1975); error calculated by propagating the main sources of uncertainty.

* calculated with measured Pb_{com} values from corresponding sample

g) 206/238 age corrected for 230Th (Schärer, 1984).

Major and trace element geochemistry

Major element compositions are listed in Table 3 and overlap with typical andesite compositions, displaying moderate SiO_2 (53-63 wt%), elevated Na_2O (3.2-5.2 wt%), low to moderate TiO_2 (0.58-1.0 wt%), CaO (4.8-7.8 wt%), K_2O (0.57-1.76 wt%) and low to moderate MgO contents (1.97-4.24 wt%). The ratios K_2O/Na_2O (0.11-0.51) and Al_2O_3/Na_2O (3.4-5.5) are low.

The data were plotted into the **T**otal **A**lkali and **S**ilica diagram (TAS) after *Le Maitre* (2002) to classify the different types of volcanic rocks. After recalculating the analyses to volatile-free (H_2O- and CO_2-free) compositions, the sum of the Na_2O and K_2O contents (total alkalis, TA) and the SiO_2 content (S) were plotted in Figure 69. The analysed rocks range from basaltic andesites to andesites and are classified as medium-K andesites of the calc-alkaline series. The Cerro Negro magmatic samples were divided into groups based on field relationships.

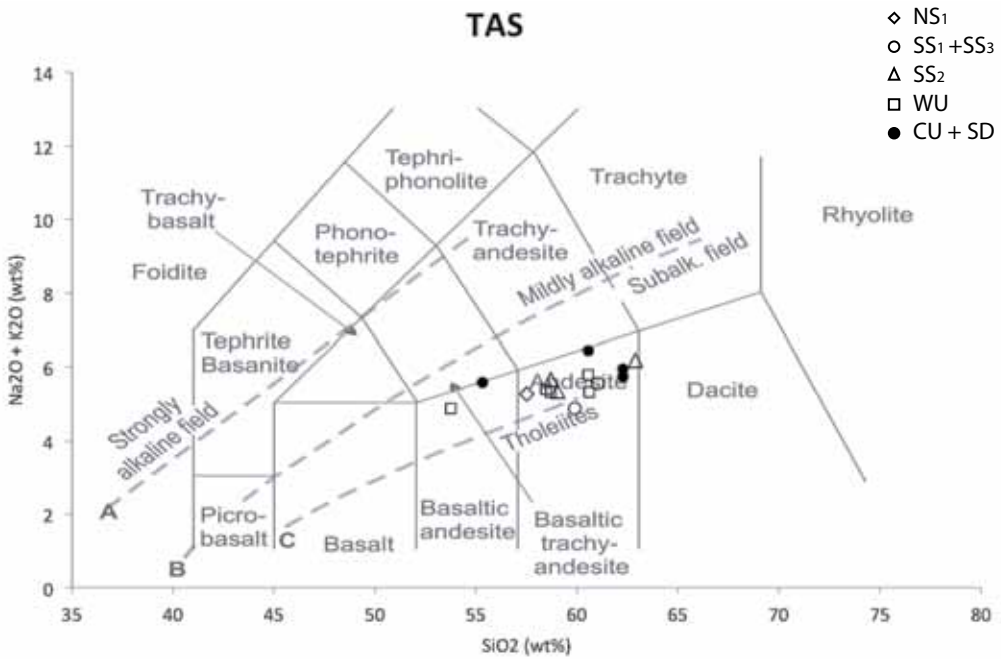

Figure 69: *Total Alkali vs. Silica diagram (Le Maitre, 2002) for all analysed Cerro Negro samples. Black filled dots represent dykes (CU, SD) shapes with no filling represent different suites of sills (NS_1, NS_2, SS_1+SS_3, SS_2).*

The rrace element contents are listed in Table 4. The trace element patterns normalised to primitive mantle (PM) after *McDonough and Sun* (1995) are shown in Figure 71. The sequence of major and trace elements used in the diagrams reflect the incompatibility of the elements in basaltic melts. The resulting diagram for 10 samples from the Cerro Negro Complex shows strongly negative Nb-Ta anomalies, and mildly to strongly positive Pb-anomalies. All but one sample show moderately positive Sr-anomalies and negative Ti-anomalies. Primitive mantle-normalised trace element and chondrite-normalised rare earth element (REE) patterns for selected samples are shown in Figures 71 and 72 (*McDonough and Sun*, 1995). The patterns in the REE diagram are essentially parallel, they show enriched LREE compared to the HREE with La/Yb ratios of 3.4-6.6. All patterns are parallel, with the exception of one sample (CN-11-17) showing a negative Ce anomaly.

Table 3: Major element data as wt% oxides for Cerro Negro magmatic rocks recalculated volatile-free

	CN-11-01	CN-11-03	CN-11-13	CN-11-14	CN-11-17	CN-11-18	CN-11-19	CN-11-20	CN-11-21A	CN-11-21B	CN-11-23	CN-11-25	CN-11-28A	CN-11-30	CN-11-26
SiO_2	57.52	61.02	62.27	60.56	62.88	58.72	59.05	55.33	58.48	53.78	60.55	58.72	62.26	59.88	60.61
Al_2O_3	18.77	17.87	17.77	17.89	17.14	18.02	17.87	18.61	18.10	17.81	17.36	18.13	17.47	18.23	17.73
Fe_2O_3	7.84	6.36	5.09	6.89	5.98	7.76	7.73	9.09	7.33	10.58	7.45	7.71	6.10	5.66	6.74
MnO	0.19	0.15	0.11	0.19	0.17	0.16	0.20	0.28	0.20	0.45	0.14	0.21	0.11	0.20	0.18
MgO	2.50	2.06	2.47	2.20	1.97	2.45	2.47	4.23	3.04	4.24	2.45	2.84	2.03	2.40	2.63
CaO	6.90	6.01	5.68	4.84	4.86	6.26	6.38	5.76	6.40	7.06	5.39	6.07	5.27	7.79	5.86
Na_2O	4.40	4.69	5.17	5.04	4.72	4.10	4.06	4.47	4.04	3.22	4.04	4.17	4.66	4.51	4.07
K_2O	0.87	0.87	0.57	1.40	1.48	1.56	1.29	1.10	1.35	1.65	1.76	1.14	1.28	0.37	1.25
TiO_2	0.78	0.65	0.66	0.66	0.58	0.70	0.69	0.95	0.76	1.00	0.66	0.78	0.59	0.70	0.67
P_2O_5	0.23	0.23	0.18	0.25	0.21	0.23	0.24	0.18	0.24	0.20	0.21	0.20	0.23	0.24	0.23
SO_3	BDL	0.08	0.01	0.08	0.01	0.03	0.01	0.01	0.05	0.00	0.00	0.01	BDL	BDL	0.03
Zr (ppm)	152.00	179.00	151.00	153.00	173.00	132.00	152.00	133.00	153.00	157.00	170.00	139.00	157.00	162.00	172.00
Total	100.00	100.00	100.00	100.00	100.00	100.00	100.00	100.00	100.00	100.00	100.00	100.00	100.00	100.00	100.00

Table 4: Trace element data as ppm for Cerro Negro magmatic rocks

	CN-11-01	CN-11-03	CN-11-14	CN-11-17	CN-11-20	CN-11-21A	CN-11-21B	CN-11-25	CN-11-28A	CN-11-30	P-B	JA-1 (1)	JA-1 (2)
Sc	9.97	8.33	7.47	9.68	20.66	15.26	23.65	9.95	6.90	9.60	0.00	22.18	22.45
Cr	1.72	2.22	1.57	4.04	17.12	4.56	6.69	4.49	2.38	5.23	0.00	5.44	5.16
Ni	1.90	2.79	2.73	4.06	19.38	7.71	12.19	4.32	2.82	4.52	0.01	1.89	1.85
Cu	6.44	9.93	20.58	11.78	28.15	10.89	18.64	18.75	5.03	7.72	0.00	43.66	45.62
Zn	78.19	372.19	90.87	78.74	77.85	62.30	123.75	62.57	48.13	45.53	0.00	105.13	111.89
Rb	15.55	19.60	19.82	10.33	34.52	12.95	44.45	12.85	14.73	7.46	0.00	8.35	8.93
Sr	443.08	377.20	407.57	228.08	410.54	401.83	409.26	333.51	387.19	529.12	0.03	233.03	236.09
Y	21.27	19.39	18.85	17.67	16.41	19.20	22.60	19.06	17.50	19.67	0.00	27.71	26.52
Zr	106.87	130.67	114.65	138.70	84.65	113.23	125.21	115.35	111.65	128.71	0.02	85.64	89.03
Nb	3.87	5.05	4.88	5.96	2.96	4.52	4.59	4.57	5.17	4.95	0.00	1.28	1.30
Cs	1.13	1.62	3.19	4.46	1.70	1.99	3.22	2.37	1.60	0.23	0.00	0.60	0.59
Ba	270.01	166.89	317.85	318.88	424.69	220.58	419.43	189.40	240.11	178.85	0.00	290.23	274.97
La	8.10	11.08	11.04	12.90	9.28	10.72	15.00	9.79	11.13	8.70	0.00	4.68	4.52
Ce	21.23	23.67	21.54	16.77	20.27	22.98	33.37	20.05	20.99	22.47	0.00	11.56	11.17
Pr	2.64	3.24	3.19	3.62	2.60	3.13	4.20	2.93	3.18	3.28	0.00	1.90	1.82
Nd	12.44	14.10	13.92	14.87	11.50	13.70	17.85	12.85	13.69	15.00	0.00	10.00	9.54
Sm	3.38	3.31	3.25	3.45	2.93	3.20	4.07	3.18	3.05	3.64	0.00	3.29	3.16
Eu	1.15	1.11	1.06	1.06	0.96	1.05	1.24	1.04	0.96	1.22	0.00	1.04	0.99
Gd	3.63	3.38	3.14	3.24	3.02	3.23	3.95	3.29	2.90	3.62	0.00	4.06	3.88
Tb	0.56	0.52	0.48	0.50	0.47	0.48	0.61	0.52	0.44	0.57	0.00	0.69	0.66
Dy	3.67	3.25	3.18	3.07	2.89	3.24	4.00	3.27	2.93	3.46	0.00	4.54	4.56
Ho	0.77	0.68	0.65	0.63	0.59	0.66	0.79	0.67	0.60	0.73	0.00	0.97	0.97
Er	2.32	2.06	1.97	1.93	1.72	1.94	2.32	2.04	1.79	2.15	0.00	2.90	2.90
Tm	0.34	0.31	0.29	0.29	0.25	0.29	0.33	0.30	0.27	0.33	0.00	0.44	0.43
Yb	2.33	2.14	1.97	2.02	1.67	1.98	2.27	2.08	1.86	2.21	0.00	2.86	2.85
Lu	0.37	0.34	0.31	0.32	0.26	0.31	0.34	0.33	0.29	0.35	0.00	0.43	0.44
Hf	2.73	3.19	2.72	3.49	2.22	2.59	3.05	2.85	2.71	3.39	0.00	2.78	2.99
Ta	0.26	0.34	0.34	0.44	0.23	0.32	0.29	0.33	0.36	0.38	0.00	0.14	0.17
Pb	3.33	16.01	18.22	5.39	2.31	4.79	11.44	2.78	5.86	2.73	0.00	5.45	5.19
Th	1.93	2.62	2.62	3.46	2.52	2.45	2.54	2.54	2.99	2.86	0.00	0.80	0.86
U	0.62	0.85	0.80	0.99	0.69	0.98	0.63	0.76	0.75	0.78	0.00	0.35	0.35

Discussion

The tectonic history of the Neuquén Andes has comprised recurrent periods of compression, extension and magmatism. These processes acted on different timescales and have overprinted each other. Therefore, the presented data do not give a complete and detailed reconstruction of magmatism and deformation in the region. On the scale of a single magmatic body, the present work is, however, the only detailed structural study of Cerro Negro to integrate field observations with absolute ages and geochemistry.

First, we will discuss the timing of sill and dyke emplacement based on crosscutting relations and absolute dating. This will be followed by the structural and temporal relationships between magma conduits and tectonic structures. Subsequently, some mechanical implications and consequences for the regional geology inferred from our observations will be discussed.

Timing of sill and dyke emplacement

Crosscutting relationships between dykes and sills have been observed at two localities (Figure 31) south of the central units, where dykes locally crosscut a folded sill – the opposite has not been observed. Furthermore, from the summit of Cerro Negro (Figure 44) we observed that a network of N-S oriented dykes crosscuts all other units, sedimentary as well as magmatic. This observation provides a relative chronology of magma emplacement and poses the question: do sills and dykes belong to two distinct magmatic systems with different times of emplacement? To test this, we have collected absolute ages and geochemical data from different units.

Geochronological data yielded more or less the same age for dykes and sills (approximately 11.0-11.5 Ma). No systematic age difference between the two distinct types of conduits has been observed. Thus, sills and dykes correspond to one subvolcanic system and have been emplaced in the same regional tectonic setting. The absolute ages obtained from different magma conduits show maximum variations of approximately 0.5 m.y. Thus, the magmatic system of Cerro Negro was active for this time period. Furthermore, as the magmatic conduits are thin sheet intrusions, their age of emplacement more or less corresponds to their time of solidification. In general, obtained zircon ages are relatively consistent and can be interpreted as a reliable indicator for the age of emplacement. Furthermore, the data collected with the ID-TIMS method complements an earlier work by Kay (2006), who reports an 40Ar/39Ar age of 11.70 ± 0.2 Ma based on one sample from the western foot of Cerro Negro.

The age of the resorbed grains is considerably older than the time of emplacement. With an age of about 1400 Ma, they most likely represent inherited grains derived from xenoliths originating from Mesoproterozoic crust.

Structural and temporal relationships between magma conduits and tectonic structures

The nature and interplay of tectonic and magmatic processes in the study area can be understood as the result of a number of complex interactions at different space and time scales, ranging from long-term regional to short-term local. Deformation has been active over a much longer time than magma emplacement.

Paleogene and Neogene compressional deformation has formed a number of synclines and anticlines in the Agrio fold-and-thrust belt (*Cobbold and Rossello,* 2003). It is generally accepted that compressional deformation has been active between the Early and Late Miocene (e.g. *Kozlowski et al.,* 1996; *Cobbold et al.,* 1999; *Cobbold and Rossello,* 2003; *Folguera and González Díaz,* 2006; *Folguera et al.,* 2007). Consequently, the Cerro Negro dated at approximately 11.0-11.5 Ma was emplaced during a period of regional compression (e.g. *Kozlowski et al.,* 1996; *Cobbold et al.,* 1999; *Cobbold and Rossello,* 2003; *Folguera et al.,* 2006; F*olguera and González Díaz,* 2006; *Galland et al.,* 2007b; *Folguera et al.,* 2008).

We observed two regional thrusts with opposite vergences and several local thrusts (Figures 44, 47). Normal faults have been observed only at one locality, where they are limited to the hinge of the China Muerta anticline (Figure 42). The orientation of these normal faults is parallel to the fold axis. Furthermore, dykes are also restricted to the hinge zone of anticlines. We did not observe a direct link between thrust ramps and magma pathways, as the magmatic system of Cerro Negro is not eroded deeply enough. On the other hand, magma conduits that have been offset by faults have not been observed either.

All sills are deformed and incorporated in a series of anticlines. These anticlines are wider compared to the anticlines that fold sedimentary rocks only. The change in wavelength with changing lithologies is clearly visible in map view (Figure 20a,b) and in cross-sections (Figure 21b-c). In the central part of the study area, the sills were also affected by folding. The deformational pattern changes from being tight, with short wavelengths in the North to open, long wavelengths in the centre, back to tight, short wavelengths in the South. This suggests that the magmatic conduits exerted some control on deformation.

The detailed structural study of the plumbing system of Cerro Negro has identified two geometries of intrusion: sills and dykes. All sills (NS_1, NS_2, SS_1, SS_2, SS_3) are folded into anticlines (e.g. Figures 21b-c, 45). With the exception of NS_2 (Figure 28) all of these anticlines are relatively open. It is inferred from our observations that E-W compression was active during and also after sill emplacement. This is best illustrated based on the observations at the eastern margin of NS_1 (Figure 27). At this locality mineralised veins most likely developed during or shortly after magma emplacement, when the magma was still hot, fluid-rich and interacted with the surrounding material. The orientation of these dilational veins at the contact to the folded sill indicates that magma emplacement took place during regional E-W shortening. The duration of compression after approximately 11.5 Ma cannot be inferred, but the substantial folding of sills suggests that the system remained compressive for some time.

Crosscutting relationships suggest that the sills are relatively older than the dykes (Figure 31). Absolute ages obtained for sills and dykes indicate similar ages for both types of conduits (Figure 68, Table 2), thus, their emplacement is considered to be almost coeval and also syntectonic. Hence, dykes and sills have both been emplaced during active shortening - the dykes possibly shortly after the sills. The orientation of the dykes (N-S), however, is against expectations (*Hubbert and Willis*, 1957; *Sibson*, 1998) perpendicular to the direction of regional shortening (E-W). How can such an incompatible orientation be explained? The solution we propose will be discussed in the next section.

Mechanical implications

Dykes are restricted to the hinge of the Cerro Negro anticline (Figure 45). This may be the reason that they show no deformation. Furthermore, their orientation is parallel to the axis of the Cerro Negro anticline (N-S). Local extensional domains were only observed in the hinge zone of the China Muerta anticline, showing that local tension is produced during folding (outer-arc stretching). We propose that a similar mechanism is valid for the Cerro Negro anticline, controlling the orientation of the dykes. This suggests that there is a structural control on the emplacement sites and orientation of the dykes.

Based on the aforementioned points we suggest the following model: the emplacement of sills is coeval with regional E-W compression that folded the sills into anticlines. As shortening continued, local N-S oriented tensional domains developed as a result of outer-arc stretching. These controlled the emplacement site and orientation of the dykes (Figure 70).

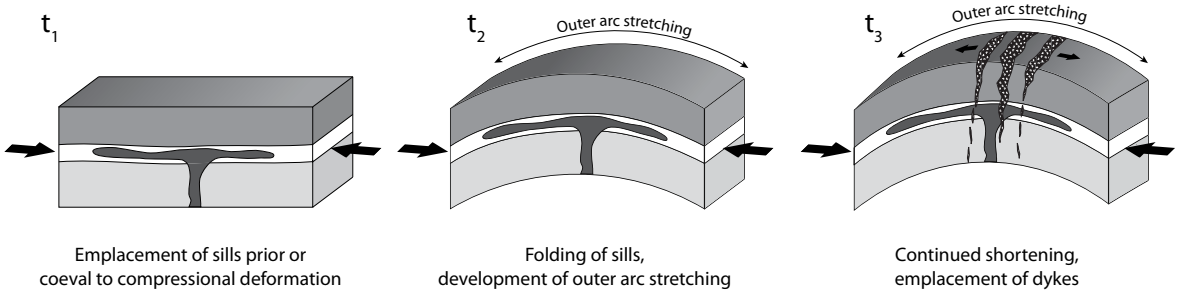

Figure 70: *Simplified sketch illustrating the structural controls on magma emplacement and the evolution of Cerro Negro. The emplacement of sills took place shortly before or coeval to regional E-W shortening (σ_3 is horizontal) 11.0-11.5 m.y. ago. As a result sills were folded in anticlines. Continued shortening gave rise to local tensional stresses (σ_3 is still horizontal, but N-S oriented) that developed under outer-arc stretching. These tensional domains controlled the N-S orientation of the sub-vertical dykes.*

A similar mechanism has previously been suggested for volcanoes occurring at the hinge zone of anticlines (*e.g. Tibaldi et al.*, 2008). These are thought to result from a combination of concurrent compression at the magma-filled core of the fold, and extension at the hinge zone, causing magma to ascend through a tear in the hinge zone.

Our observations are also consistent with the proposed vertical partitioning of magmatic systems in compressional settings (Figure 7, *Tibaldi*, 2008; *González et al.*, 2009), even though a vertical partitioning of the Cerro Negro magmatic system between deep compressional domains and shallow extensional domains has not been directly observed. The fact that we observed magmatic conduits with two geometries resulting from different states of stress, however, suggests that we were in fact close to such a transition.

On the contrary, the emplacement of dykes in local tensional domains with N-S orientation during E-W oriented regional shortening is not compatible with the observations at Tromen volcano (*Galland et al.*, 2007b), where the orientation of dykes is parallel to the direction of shortening (E-W). A possible explanation is that the load of the volcanic edifice itself influences the local stress field and resulting orientation of the dykes. This mechanism has been confirmed by laboratory experiments (*Marques and Cobbold*,

2002; *Galland et al.*, 2003; *Galland*, 2004; *Galland et al.*, 2007a) and geophysical observations (*Legrand et al.*, 2002). As Tromen is significantly larger in size than Cerro Negro, its weight may exert a first order control on the orientation of dykes. This effect has been previously pointed out by *Odé* (1957) based on observations at Spanish Peaks, Colorado, United States of America.

In fact, the experiments by *Galland et al.* (2007a) are able to reproduce tensional cracks with both orientations (parallel and perpendicular to shortening direction). The mechanism controlling the opposite orientation of the cracks that may act as dyke emplacement sites is not clear. To understand the underlying mechanism and to address the hypothesis of vertical partitioning of magmatic systems in compression, it may be important to introduce the weight of the volcanic edifice in the scaled laboratory experiments.

Correlation with regional geology: regional implications

The structural evolution of the study area is characterised by compressional deformation. As previously described, all sills are clearly folded into anticlines and have undergone significant deformation. Thus, the Cerro Negro does not postdate the youngest regional deformation in the area, as proposed by *Kay and Ramos* (2006); *Folguera et al.* (2007), who argue that Cerro Negro undeformed volcanics (11.7 ± 0.2 Ma) unconformably overlie Cretaceous strata. This leads the authors to the conclusion that regional shortening occurred between 15 Ma (based on the oldest K/Ar age of the Charilehue Formation (*Uliana et al.*, 1973; *Llambías et al.*, 1978)) and approximately 12 Ma, when Cerro Negro was active. We argue, instead, that deformation continued after the relatively short-lived emplacement of the sills about 11.0-11.5 Ma ago, as they have been folded substantially. It is not clear how long after emplacement compressional deformation remained active. The absolute age of the different conduits also constrains the lifetime of the magmatic system to less than 0.5 m.y.

Several authors argue that the tectonic regime switched to extensional after 12 Ma and has remained so until today (*e.g. Kozlowski et al.*, 1996; *Jordan et al.*, 2001; *Folguera et al.*, 2006; *Folguera et al.*, 2008; *Folguera et al.*, 2010). Moreover, based on previous regional studies, it has been suggested that Miocene deformation in the area is moderate and the amount of shortening rather weak (*e.g. Cobbold and Rossello*, 2003; *Kay and Ramos*, 2006; *Folguera et al.*, 2007). Our field observations and the resulting structural cross-sections (Figure 21a-d), however, show that significant E-W shortening has occurred during and after the emplacement of the Miocene Cerro Negro magmatic system, as recoded by the deformed sills of Middle Miocene age.

No effusive rocks originating from Cerro Negro have been observed. Instead, all contacts between magmatic conduits and country rock are intrusive. Upper and lower contacts of sills have been mapped at several localities. This is not in agreement with previous observations *(Zöllner and Amos*, 1973; *Kay*, 2006) that describe subaerial lava flows.

We suggest that lava flows, if they were present in the past, have been eroded due to uplift related to compressional deformation since 11 Ma. Overall, the erosion level suggests that there has been significant tectonic uplift. Alternatively, Cerro Negro may represent a subvolcanic system that never reached the surface. Additionally, observations at Cerro Colorado do not confirm the findings of *Zöllner and Amos* (1973), who assigned it to the Rayoso Formation. Most of this

mountain is made of magmatic rocks that show no clear relationship to the surrounding sediments of the Huitrín and Rayoso Formations.

Constrains from major and trace element geochemistry

Fractional crystallisation can be displayed in major element plots (Figure 71). Variation diagrams are used to investigate the chemical changes that accompany magma differentiation. In order to show the variation between individual samples, their relationships to each other and to make trends visible, all major element data were plotted in variation diagrams. Different elements can provide hints for the crystallisation of specific minerals e.g. plagioclase (decreasing Al_2O_3 and Sr). MgO in wt% was plotted along the x-axis, as it serves as an index of advancing fractional crystallsation (Mg decreases with increasing fractionational crystallisation). The variation in the MgO content is a consequence of the breakdown of magnesian-bearing phases during partial melting or their removal during fractional crystallisation (*Rollinsson*, 1993).

The SiO_2 vs. MgO diagram shows a relatively steep negative trend, where SiO_2 increases with decreasing MgO,. This is characteristic of advancing fractional crystallisation involving the removal of Si-free minerals such as Fe-Ti oxides and also amphiboles and pyroxenes. Generally, samples CN-11-20 (dyke south of CU) and CN-11-21B (mafic enclave in andesitic matrix (21A)) represent outliers in all diagrams due to higher MgO contents compared to the other samples. The removal of Fe-Ti oxides (such as ilmenite and Ti-magnetite) is also reflected in the slightly decreasing TiO_2 and moderately decreasing Fe_2O_3 with decreasing MgO. The CaO vs. MgO plot is generally used together with Al_2O_3 and Na_2O as a measure of feldspar fractionation. CaO may have been removed by either calcic plagioclase, clinopyroxene, and/or amphibole. Similar to the Al_2O_3 vs. MgO diagram, the CaO vs. MgO diagram shows considerable scatter. The different units follow different trends. The samples from the WU indicate a clear trend of increasing CaO with increasing MgO contents. Together with the positive Sr-anomalies that represent a subduction signature, this diagram suggests other processes than simple fractional crystallisation, for example alteration. Na_2O behaves nearly constant with MgO contents with variations of about 1 wt%. With increasing degree of fractionation feldspars become Na-rich, and the Na_2O content of the residual melt will tend to decrease.

The P_2O_5 contents have relatively stable concentrations (0.175-0.245 wt%), and appear to slightly increase with decreasing MgO to the concentration of MgO ca. 2.2 wt%. After that, P_2O_5 decreases slightly, probably as a result of the removal of apatite. This in agreement with the petrography of the samples. Zirconium was plotted against SiO_2 as it provides an indication for the degree of alteration. Here, it shows a more or less positive trend, Zr increasing with increasing SiO_2. The scatter in this plot may also arise from the inheritance of zircon grains that were also found during zircon dating. Presence of xenocrystic zircon can cause deviations of Zr contents from the estimated differentiation trend. As observed in the thin sections, the degree of alteration is relatively low. There is, however, some scatter in the K_2O, Ca, Rb and LOI vs. MgO, which may reflect minor degrees of late alteration processes, possibly caused by weathering. Altogether, the major element compositions reflect trends toward an evolving magma composition, indicative of fractional crystallisation as represented by the removal of the observed phe-

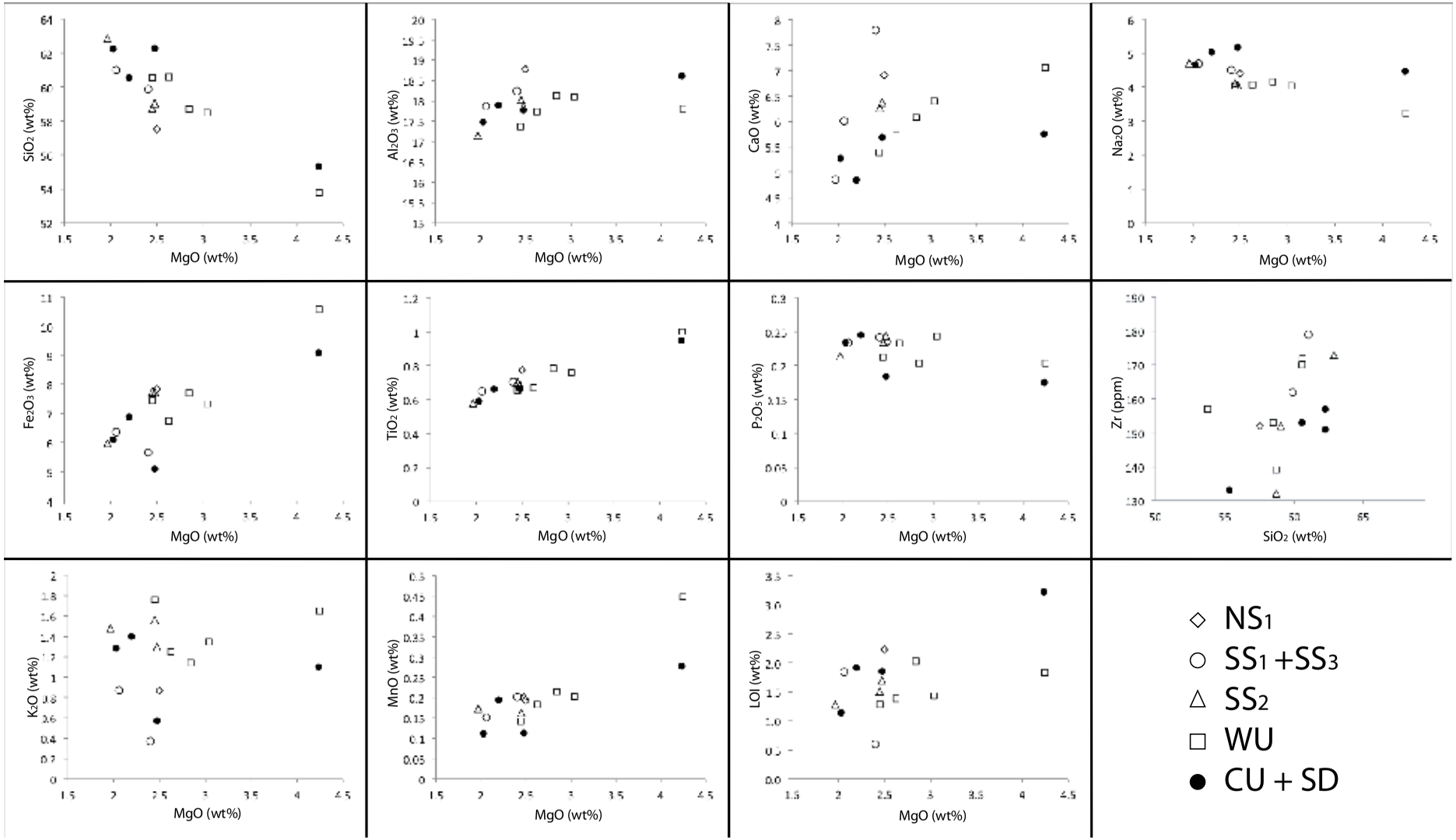

Figure 71: *Major element variation diagrams for Cerro Negro magmatic rocks. Major elements (wt%) plotted against MgO (wt%) and Zr (ppm) plotted against SiO_2.*

nocryst assemblages (px, hbl, plag, Fe-Ti oxides). This is in agreement with the textures observed in thin section, which show plagioclase as early phase, and pyroxenes and Fe-Ti oxides as late phases.

The trace element concentrations of igneous rocks result from a combination of different processes. These are (1) the degree of partial melting of the source region, (2) the enrichment of incompatible elements within the source region, (3) the degree of fractional crystallisation, (4) the degree of crustal contamination.

Negative Nb-Ta- and positive Pb-anomalies as shown in Figure 72 are common in subduction zone magmas (e.g. *Dostal et al.*, 1996; *Seghedi et al.*, 2001; *Dorais and Tubrett*, 2008). The resulting patterns are commonly referred to as "arc-type characteristics". However, such geochemical features are also common in the continental crust (e.g. *Rudnick*, 2005). The samples from the Cerro Negro area are located in a back-arc setting.

There is some scatter in Pb contents and the positive anomalies in the primitive mantle-normalised trace element patterns could reflect interaction with the continental crust (e.g. *Rudnick*, 2005) or a source signature from subduction-fluid overprinted mantle wedge. Further evidence (e.g. Sr-Nd-Hf isotope compositions) is needed to differentiate between different processes and to trace the origin of the signature. The lack of Eu-anomalies may suggest the absence of plagioclase fractionation in the deeper crust, but fractionation at more shallow levels and because of the suppression of plagioclase crystallisation due to higher water contents in the magma.

In general, considering the trace element plots, the following has been observed: a) incompatible and immobile trace elements like the high-field-strength elements (HFSE; Zr, Nb, Ta, Hf) show positive correlations with increasing differentiation possibly indicating the fractionation of amphibole and Fe-Ti-oxides, b) the incompatible but mobile trace elements like K, Rb, Ba, Pb,

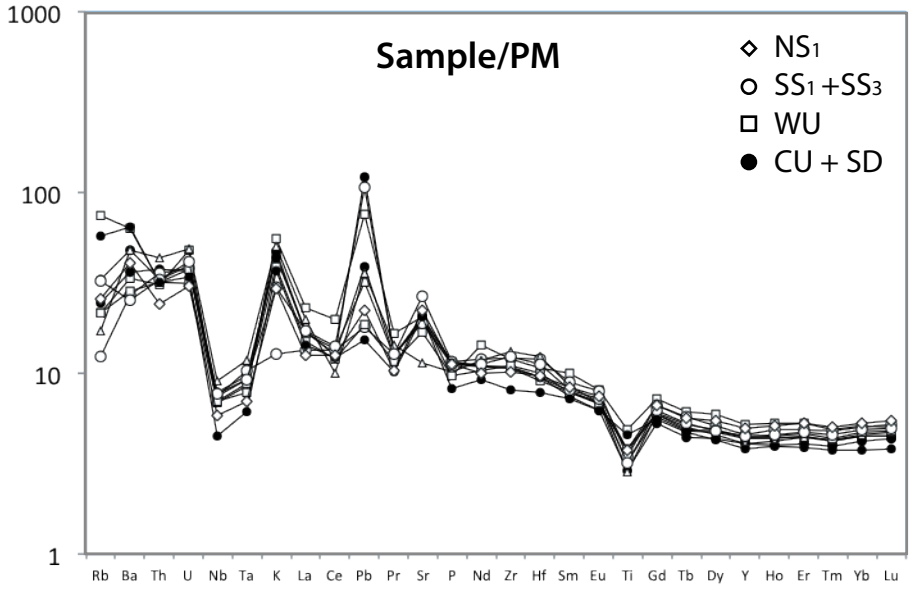

Figure 72: *Primitive mantle (PM)-normalised trace element diagram for Cerro Negro magmatic rocks. PM normalisation values after McDonough and Sun (1995). Filled circles represent dykes, open shapes represent different sills.*

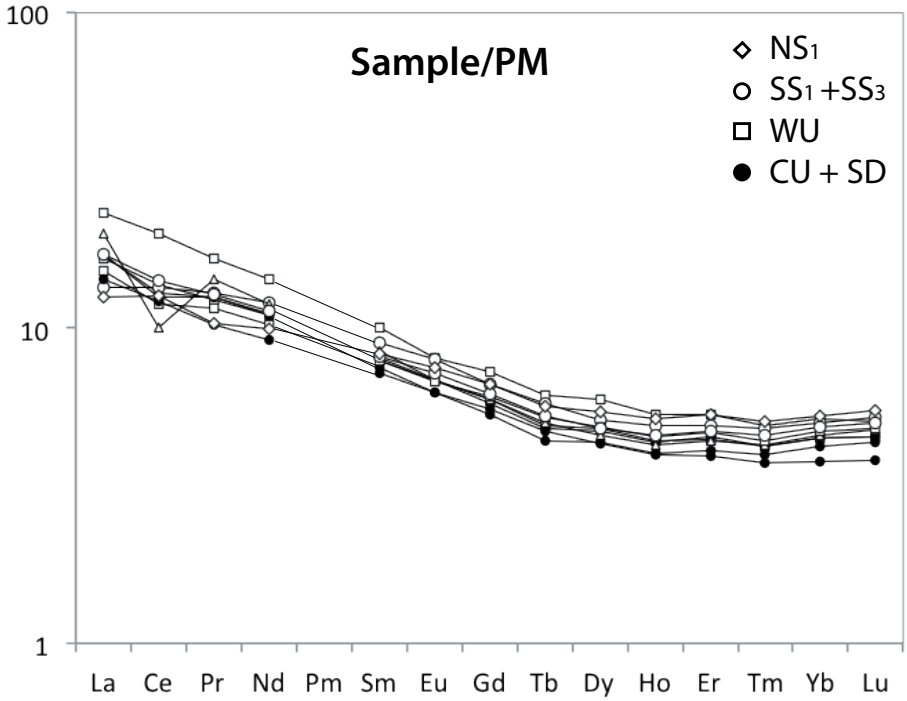

Figure 73: *Primitive mantle (PM)-normalised REE diagram for Cerro Negro magmatic rocks. PM normalisation values after McDonough and Sun (1995). Filled circles represent dykes, empty shapes represent different sills.*

Cs, U (Sr too, but Sr is commonly compatible with plagioclase) are more scattered and trends are not well defined or non-existent. This suggests that mobile incompatible elements may have undergone different (selective) enrichments due to the fluids derived from the subducted slab overprinting the mantle source. The scatter may result in the fact that andesites represent relatively evolved magmas that deviate from expected differentiation trends. This may be further enhanced by the assimilation of xenocrystic material.

Similar fractional crystallisation paths, smooth REE (Figure 73) and multivariate plots for all samples have been observed. The single negative Ce anomaly may be due to an analytical error or due to alteration. Ce is redox sensitive in fluids, possibly resulting in such a negative Ce anomaly. Overall, no systematic difference between dykes and sills has been observed, possibly indicating a similar source.

Conclusion

The present study of the Cerro Negro intrusive complex has provided:

- a detailed geological map and cross-sections with emphasis on magmatic conduits, their contacts to the surrounding sediments and tectonic structures,
- robust absolute ages for several conduits with distinct geometries,
- major and trace element data.

The integration of these allows us to draw the following conclusions:

1. The structure of the Cerro Negro consists of sills and dykes andesitic in composition.
2. Both, sills and dykes belong to the same magmatic system with a lifetime of approximately 0.5 m.y.
3. The sediments of the Agrio fold-and-thrust belt surrounding the intrusions are intensely folded into synclines and anticlines and offset by regional thrust faults.
4. There is robust evidence for the emplacement of the Cerro Negro intrusive system made of sills and dykes coeval with regional Middle Miocene compressional deformation.
5. We infer a stratigraphic control on the emplacement level of sills. There is a structural control on the emplacement of sills in anticlines, whereas the dykes are restricted to the hinge zone of anticlines.
6. The change in deformation patterns (different wavelengths) is due to the presence of shallow magmatic bodies.
7. We suggest that the emplacement of dykes at the hinge zone of anticlines (perpendicular to shortening direction) during horizontal compression resulted from outer-arc stretching.
8. We have documented the first robust evidence for substantial Middle to Late Miocene shortening in the area.

The integration of field observations with geochronological and geochemical data from magmatic bodies is the key to understand the evolution of shallow magmatic systems emplaced in a shortening crust.

The petrographic observations and geochemical data collected only allow preliminary conclusions at this stage. Being beyond the scope of this study, it may be required to collect more trace and major element data on all 42 samples. Isotopic data may be useful to characterise the source of the magma and to resolve the interconnectivity of different conduits. Furthermore, it may be interesting to date

zircon populations from several more conduits. For example data on NS_2 may answer the question of whether this conduit is more deformed because it is older and underwent several stages of deformation.

In summary, the Cerro Negro intrusive complex represents an eroded shallow magmatic system that has been emplaced during active shortening in the Agrio fold-and-thrust belt in the Middle Miocene. Sills were substantially folded during and after their emplacement. Consequently, regional shortening occurred after 11 Ma. This study represents the first robust evidence of strong shortening during the last 11 Ma in the region. Furthermore, our observations lead to the hypothesis that there is a structural control on magma emplacement and a vertical partitioning of the magmatic system between compressional and local extensional domains.

We provide a new dataset that improves our understanding of shallow magmatic systems coeval with compressional deformation. It may, together with other integrated studies, resolve some of the contrasting observations and interpretations in the Neuquén Andes.

References

Allmendinger, R. W., T. E. Jordan, S. M. Kay, and B. L. Isacks (1997), The evolution of the Altiplano-Puna Plateau of the Central Andes, Annu Rev Earth Pl Sc, 25(1), 139-174.

Armijo, R., R. Rauld, R. Thiele, G. Vargas, J. Campos, R. Lacassin, and E. Kausel (2010), The West Andean Thrust, the San Ramon Fault, and the seismic hazard for Santiago, Chile, Tectonics, 29.

Assumpção, M., and M. Araujo (1993), Effect of the Altiplano-Puna plateau, South America, on the regional intraplate stresses, Tectonophysics, 221(3–4), 475-496.

Barazangi, M., and B. L. Isacks (1976), Spatial distribution of earthquakes and subduction of the Nazca plate beneath South America, Geology, 4(11), 686-692.

Best, M. G. (2003), Igneous and Metamorphic Petrology, 2nd ed., Blackwell Science Ltd, Oxford.

Bracaccini, O. (1970), Rasgos tectónicos de las acumulaciones mesozoicas en las provincias de Mendoza y Neuquén, República Argentina, Revista de la Asociación Geológica Argentina, 25(2), 275-284.

Branquet, Y., and B. V. de Vries (2001), Effects of volcanic loading on regional compressive structures: new insights from natural examples and analogue modelling., Cr Acad Sci Ii A, 333(8), 455-461.

Burns, W. M., T. E. Jordan, P. Copeland, and S. A. Kelley (2006), The case for extensional tectonics in the Oligocene-Miocene Southern Andes as recorded in the Cura Mallin basin (36°-38°S), Geological Society of America - Special Papers, 407, 163.

Capitanio, F. A., C. Faccenna, S. Zlotnik, and D. Stegman (2011), Subduction dynamics and the origin of Andean orogeny and the Bolivian orocline, Nature, 480(7375), 83-86.

Cas, R. A. F., Wright, J. V. (1987), Volcanic successions, modern and ancient. A geological approach to processes products and successions, Allen & Unwin, London.

Cembrano, J., and L. Lara (2009), The link between volcanism and tectonics in the southern volcanic zone of the Chilean Andes: A review, Tectonophysics, 471(1–2), 96-113.

Charrier, R., L. Pinto, M. P. Rodríguez, T. Moreno, and W. Gibbons (2007), Tectonostratigraphic evolution of the Andean Orogen in Chile, The Geology of Chile (Moreno, T.; Gibbons, W.; editors). The Geological Society, 21-114.

Chiu, J. M. (1992), Seismicity and tectonics in Jujuy province, northwestern Argentina, Tectonics, 11(5), 934-959.

Clavero, J. E., R. S. J. Sparks, M. S. Pringle, E. Polanco, and M. C. Gardeweg (2004), Evolution and volcanic hazards of Taapaca Volcanic Complex, Central Andes of Northern Chile, J Geol Soc London, 161(4), 603-618.

Cloos, H. (1923), II. Die „Batholithen“ des Bayrischen Waldes und der Pfahl, Geologische Rundschau, 14(1), 12-20.

Cobbold, P. R., and E. A. Rossello (2003), Aptian to recent compressional deformation, foothills of the Neuquén Basin, Argentina, Marine and Petroleum Geology, 20(5), 429-443.

Cobbold, P. R., M. Diraison, and E. A. Rossello (1999), Bitumen veins and Eocene transpression, Neuquén Basin, Argentina, Tectonophysics, 314(4), 423-442.

Condon, D. J., and S. A. Bowring (2011), Chapter 9 A user's guide to Neoproterozoic geochronology, Geological Society, London, Memoirs, 36(1), 135-149.

Corfu, F. (2004), U-Pb age, setting and tectonic significance of the anorthosite-mangerite-charnockite-granite suite, Lofoten-Vesteralen, Norway, J Petrol, 45(9), 1799-1819.

Corfu, F., J. M. Hanchar, P. W. O. Hoskin, and P. Kinny (2003), Atlas of zircon textures, Rev Mineral Geochem, 53, 469-500.

Corti, G., G. Moratti, and F. Sani (2005), Relations between surface faulting and granite intrusions in analogue models of strike-slip deformation, J Struct Geol, 27(9), 1547-1562.

D'Lemos, R. S., M. Brown, and R. A. Strachan (1992), Granite magma generation, ascent and emplacement within a transpressional orogen, J Geol Soc London, 149(4), 487-490.

Davis, D. W., C. E. Blackburn, and T. E. Krogh (1982), Zircon U-Pb Ages from the Wabigoon-Manitou Lakes Region, Wabigoon Subprovince, Northwest Ontario, Can J Earth Sci, 19(2), 254-266.

Davis, D. W., I. S. Williams, and T. E. Krogh (2003), Historical development of zircon geochronology, Rev Mineral Geochem, 53, 145-181.

Delpino, D., and M. Deza (1995), Mapa geológico y de recursos minerales de la provincia del Neuquén.

Dorais, M. J., and M. Tubrett (2008), Identification of a subduction zone component in the Higganum dike, Central Atlantic Magmatic Province: A LA-ICPMS study of clinopyroxene with implications for flood basalt petrogenesis, Geochem Geophy Geosy, 9(10), Q10005.

Dostal, J., C. Dupuy, and P. Dudoignon (1996), Distribution of boron, lithium and beryllium in ocean island basalts from French Polynesia: implications for the B/Be and Li/Be ratios as tracers of subducted components, Mineral Mag, 60(401), 563-580.

Dulski, P. (2001), Reference materials for geochemical studies: New analytical data by ICP-MS and critical discussion of reference values, Geostandard Newslett, 25(1), 87-125.

Ferré, E. C., O. Galland, D. Montanari, and T. J. Kalakay (2012), Granite magma migration and emplacement along thrusts, Int J Earth Sci (Geol Rundsch), 1-16.

Folguera, A., V. A. Ramos, and D. Melnick (2002), Partición de la deformación en la zona del arco volcánico de los Andes neuquinos (36-39 S) en los últimos 30 millones de años, Rev Geol Chile, 29(2),

227-240.

Folguera, A., T. Zapata, and V. A. Ramos (2006), Late Cenozoic extension and the evolution of the Neuquén Andes, Geological Society of America - Special Publication, 407, 267.

Folguera, A., V. A. Ramos, R. L. Hermanns, and J. Naranjo (2004), Neotectonics in the foothills of the southernmost central Andes (37°-38°S): Evidence of strike-slip displacement along the Antinir-Copahue fault zone, Tectonics, 23(5), TC5008.

Folguera, A., V. A. Ramos, T. Zapata, and M. G. Spagnuolo (2007a), Andean evolution at the Guañacos and Chos Malal fold and thrust belts (36°30S–37°S), Journal of Geodynamics, 44(3–5), 129-148.

Folguera, A., G. Bottesi, T. Zapata, and V. A. Ramos (2008), Crustal collapse in the Andean backarc since 2 Ma: Tromen volcanic plateau, Southern Central Andes (36°40'–37°30'S), Tectonophysics, 459(1–4), 140-160.

Folguera, A., E. Rojas Vera, G. Bottesi, G. Zamora Valcarce, and V. A. Ramos (2010), The Loncopué Trough: A Cenozoic basin produced by extension in the southern Central Andes, Journal of Geodynamics, 49(5), 287-295.

Folguera, A., A. Introcaso, M. Gimenez, F. Ruiz, P. Martinez, C. Tunstall, E. G. Morabito, and V. A. Ramos (2007b), Crustal attenuation in the Southern Andean retroarc (38 degrees-39 degrees 30 ' S) determined from tectonic and gravimetric studies: The Lonco-Luan asthenospheric anomaly, Tectonophysics, 439(1-4), 129-147.

Folguera, A. R., V.A., , and E. F. González Díaz, Hermanns, F (2006), Miocene to Quaternary deformation of the Guañacos fold-and-thrust belt in the Neuquén Andes between 37°S and 37°30'S, Geological Society of America Special Papers, 407, 247-266.

Forsythe, R. (1982), The Late Paleozoic to Early Mesozoic Evolution of Southern South-America - a Plate Tectonic Interpretation, J Geol Soc London, 139, 671-682.

Franzese, J. R., and L. A. Spalletti (2001), Late Triassic-early Jurassic continental extension in southwestern Gondwana: tectonic segmentation and pre-break-up rifting, Journal of South American Earth Sciences, 14(3), 257-270.

Galland, O. (2004), Interactions mécaniques entre la tectonique compressive et le magmatisme: expériences analogiques et exemple naturel, 432 pp, Université de Rennes, Rennes.

Galland, O., J. D. de Bremond d'Ars, P. R. Cobbold, and E. Hallot (2003), Physical models of magmatic intrusion during thrusting, Terra Nova, 15(6), 405-409.

Galland, O., P. R. Cobbold, d. A. de Bremond, J., and E. Hallot (2007a), Rise and emplacement of magma during horizontal shortening of the brittle crust: Insights from experimental modeling, J. Geophys. Res., 112(B6), B06402.

Galland, O., E. Hallot, P. R. Cobbold, G. Ruffet, and J. de Bremond d'Ars (2007b), Volcanism in a compressional Andean setting: A structural and geochronological study of Tromen volcano (Neuquen province, Argentina), Tectonics, 26(4).

Garbe-Schönberg, C.-D. (1993), Simultaneous determination of thirty-seven trace elements in twenty-eight international rock standards by ICP-MS, Geostandards Newsletter, 17(1), 81-97.

Gephart, J. W. (1994), Topography and subduction geometry in the central Andes: Clues to the mechanics of a noncollisional orogen, J. Geophys. Res., 99(B6), 12279-12288.

Glazner, A. F., and J. M. Bartley (1994), Eruption of alkali basalts during crustal shortening in southern California, Tectonics, 13(2), 493-498.

González, G., J. Cembrano, F. Aron, E. E. Veloso, and J. B. H. Shyu (2009), Coeval compressional deformation and volcanism in the central Andes, case studies from northern Chile (23°S-24°S), Tectonics, 28(6), TC6003.

Govindaraju, K. (1994), 1994 Compilation of Working Values and Sample Description for 383 Geostandards, Geostandards Newsletter, 18(2), 1-158.

Gressier, J.-B., R. Mourgues, L. Bodet, J.-Y. Matthieu, O. Galland, and P. Cobbold (2010), Control of pore fluid pressure on depth of emplacement of magmatic sills: An experimental approach, Tectonophysics, 489(1–4), 1-13.

Groeber, P. (1929), Líneas fundamentales de la geología del Neuquén, sur de Mendoza y regiones adyacentes, Talleres gráficos del Ministerio de agricultura de la nación.

Guerello, R. (2006), Geología del sector norte de la fosa de Chos Malal, Provincia de Neuquén, 123 pp, Universidad de Buenos Aires, Buenos Aires, Argentina.

Guineberteau, B., J. L. Bouchez, and J. L. Vigneresse (1987), The Mortagne Granite Pluton (France) Emplaced by Pull-Apart Along a Shear Zone - Structural and Gravimetric Arguments and Regional Implication, Geol Soc Am Bull, 99(6), 763-770.

Guzmán, C., E. Cristallini, and G. Bottesi (2007), Contemporary stress orientations in the Andean retroarc between 34 S and 39 S from borehole breakout analysis, Tectonics, 26(3), TC3016.

Guzmán, S. R., I. A. Petrinovic, and J. A. Brod (2006), Pleistocene mafic volcanoes in the Puna Cordillera Oriental boundary, NW-Argentina, Journal of Volcanology and Geothermal Research, 158, 51-69.

Hamilton, W. B. (1994), Subduction systems and magmatism, Geological Society, London, Special Publications, 81(1), 3-28.

He, S. D., P. Kapp, P. G. DeCelles, G. E. Gehrels, and M. Heizler (2007), Cretaceous-Tertiary geology of the Gangdese Arc in the Linzhou area, southern Tibet, Tectonophysics, 433(1-4), 15-37.

Heuret, A., and S. Lallemand (2005), Plate motions, slab dynamics and back-arc deformation, Physics of the Earth and Planetary Interiors, 149(1), 31-51.

Heuret, A., F. Funiciello, C. Faccenna, and S. Lallemand (2007), Plate kinematics, slab shape and back-arc stress: a comparison between laboratory models and current subduction zones, Earth Planet Sc Lett, 256(3), 473-483.

Hickey, R. L., F. A. Frey, D. C. Gerlach, and L. Lopez-Escobar (1986), Multiple sources for basaltic arc rocks from the Southern Volcanic Zone of the Andes (34°- 41°S): Trace Element and isotopic evidence for contributions from subducted oceanic crust, mantle, and continental crust, J. Geophys. Res., 91(B6), 5963-5983.

Hildreth, W., and S. Moorbath (1988), Crustal Contributions to Arc Magmatism in the Andes of Central Chile, Contrib Mineral Petr, 98(4), 455-489.

Hoffmann, J. E., C. Münker, T. Næraa, M. T. Rosing, D. Herwartz, D. Garbe-Schönberg, and H. Svahnberg (2011), Mechanisms of Archean crust formation inferred from high-precision HFSE systematics in TTGs, Geochim Cosmochim Ac, 75(15), 4157-4178.

Howell, J. A., E. Schwarz, L. A. Spalletti, and G. D. Veiga (2005), The Neuquén Basin: an overview, Geological Society, London, Special Publications, 252(1), 1-14.

Hubbert, M. K., and D. G. Willis (1957), Mechanics of Hydraulic Fracturing, T Am I Min Met Eng, 210(6), 153-163.

Hutton, D. H. W. (1982), A Tectonic Model for the Emplacement of the Main Donegal Granite, New Ireland, J Geol Soc London, 139, 615-631.

Hutton, D. H. W. (1988), Granite emplacement mechanisms and tectonic controls: inferences from deformation studies, Earth and Environmental Science Transactions of the Royal Society of Edinburgh, 79(2-3), 245-255.

Hutton, D. H. W. (1997), Syntectonic granites and the principle of effective stress: A general solution to the space problem?, Petr Stru G, 8, 189-197.

Isacks, B. L. (1988), Uplift of the Central Andean Plateau and Bending of the Bolivian Orocline, J. Geophys. Res., 93(B4), 3211-3231.

Jaffey, A. H., K. F. Flynn, Glendeni.Le, W. C. Bentley, and A. M. Essling (1971), Precision Measurement of Half-Lives and Specific Activities of U-235 and U-238, Phys Rev C, 4(5), 1889.

Jordan, T. E., B. L. Isacks, R. W. Allmendinger, J. A. Brewer, V. A. Ramos, and C. J. Ando (1983), Andean tectonics related to geometry of subducted Nazca plate, Geol Soc Am Bull, 94(3), 341-361.

Jordan, T. E., W. M. Burns, R. Veiga, F. Pangaro, P. Copeland, S. Kelley, and C. Mpodozis (2001), Extension and basin formation in the southern Andes caused by increased convergence rate: A mid-

Cenozoic trigger for the Andes, Tectonics, 20(3), 308-324.

Kalakay, T. J., B. E. John, and D. R. Lageson (2001), Fault-controlled pluton emplacement in the Sevier fold-and-thrust belt of southwest Montana, USA, J Struct Geol, 23(6-7), 1151-1165.

Kapp, P., P. G. DeCelles, A. L. Leier, J. M. Fabianic, S. He, A. Pullen, G. E. Gehrels, and L. Ding (2007), The Gangadese retroarc thrust belt revealed, GSA Today, 17, 4-9.

Kay, S. M. (2005), Tertiary to Recent evolution of Andean arc and backarc magmas between 36°S and 38°S and evidence for Miocene shallowing of the Nazca Plate under the Neuquén Basin.

Kay, S. M., and V. A. Ramos (2006), Evolution of an Andean margin: a tectonic and magmatic view from the Andes to the Neuquén Basin, 343 pp., Geol Soc Am Special Paper

Kay, S. M., and P. Copeland (2006), Early to middle Miocene backarc magmas of the Neuquén Basin: Geochemical consequences of slab shallowing and the westward drift of South America, Geological Society of America - Special Papers, 407, 185.

Kay, S. M., Burns, M. W., Copeland, P. Mancilla, O. (2006), Upper Cretaceous to Holocene magmatism and evidence for transient Miocene shallowing of the Andean subduction zone under the northern Neuquén Basin, in Evolution of an Andean Margin: A Tectonic and Magmatic View From the Andes to the Neuquén Basin (35° – 39°S lat.), edited by S. M. K. and V. Ramos, pp. 19–60.

Keidel, J. (1925), Sobre la estructura tectónica de las capas petrolíferas en el oriente del territorio del Neuquén, Minist. de Agr.

Klotz, J., G. Khazaradze, D. Angermann, C. Reigber, R. Perdomo, and O. Cifuentes (2001), Earthquake cycle dominates contemporary crustal deformation in Central and Southern Andes, Earth Planet Sc Lett, 193(3), 437-446.

Kozlowski, E. E., C. E. Cruz, and C. A. Sylwan (1996), Geología estructural de la zona de Chos Malal, cuenca Neuquina, Argentina, paper presented at XIII Congreso Geológico Argentino y III Congreso de Exploración de Hidrocarburos, Buenos Aires, Acta.

Krogh, T. E. (1973), Low-Contamination Method for Hydrothermal Decomposition of Zircon and Extraction of U and Pb for Isotopic Age Determinations, Geochim Cosmochim Ac, 37(3), 485-494.

Lallemand, S., A. Heuret, and D. Boutelier (2005), On the relationships between slab dip, back-arc stress, upper plate absolute motion, and crustal nature in subduction zones, Geochem Geophy Geosy, 6(9), Q09006.

Le Maitre, R. W., Streckeisen, A., Zanettin, B., Le Bas, M.J., Bonin, B., Bateman, P., Bellieni, G., Dudek, A., Efremova, S., Keller, J., Lameyre, J., Sabine, P.A., Schmid, R., Sørensen, H., Woolley, A.R. (2002), Igneous Rocks. A Classification and Glossary of Terms. Recommendations of the International Union of Geological Sciences Subcommission on the Systematics of Igneous Rocks 2nd Edition ed., Cambridge University Press, Cambridge.

Leanza, H., Hugo, C., Repol, D., González, R., Danieli, J. (2001), Hoja geológica Zapala, 128, Instituto de Geología y Recursos Hoja 3969-I, Buenos Aires, Argentina.

Leanza, H. A. (unpublished), Mapa geológico de la Provincia del Neuquén, República Argentina, Edición 2011, Servicio Geológico Minero Argentino, Instituto de Geología y Recursos Minerales.

Legarreta, L., and M. A. Uliana (1996), The Jurassic succession in west-central Argentina: Stratal patterns, sequences and paleogeographic evolution, Palaeogeogr Palaeocl, 120(3-4), 303-330.

Legrand, D., A. Calahorrano, B. Guillier, L. Rivera, M. Ruiz, D. Villagómez, and H. Yepes (2002), Stress tensor analysis of the 1998-1999 tectonic swarm of northern Quito related to the volcanic swarm of Guagua Pichincha volcano, Ecuador, Tectonophysics, 344, 15-36.

Llambías, E., M. Palacios, J. Danderfer, and N. Brogioni (1978), Petrología de las rocas ígneas cenozoicas del Volcán Domuyo y áreas adyacentes, Provincia del Neuquén, paper presented at Proceedings, 7th Congreso Geológico Argentino: Neuquén, Asociación Geológica Argentina.

Lopez-Escobar, L., F. Frey, and M. Vergara (1977), Andesites and high-alumina basalts from the central-south Chile high Andes: Geochemical evidence bearing on their petrogenesis, Contrib Mineral Petr, 63(3), 199-228.

Ludwig, K. R. (2009), Isoplot 4.1. A geochronological toolkit for Microsoft Excel, Berkeley Geochronology Center Special Publications, 4(76).

Macdonald, R., R. S. J. Sparks, H. Sigurdsson, D. P. Mattey, D. W. Mcgarvie, and R. L. Smith (1987), The 1875 Eruption of Askja Volcano, Iceland - Combined Fractional Crystallization and Selective Contamination in the Generation of Rhyolitic Magma, Mineral Mag, 51(360), 183-202.

Marques, F. O., and P. R. Cobbold (2002), Topography as a major factor in the development of arcuate thrust belts: insights from sandbox experiments, Tectonophysics, 348(4), 247-268.

Mattinson, J. M. (2005), Zircon U-Pb chemical abrasion ("CA-TIMS") method: Combined annealing and multi-step partial dissolution analysis for improved precision and accuracy of zircon ages, Chem Geol, 220(1-2), 47-66.

Mattinson, J. M. (2010), Analysis of the relative decay constants of U-235 and U-238 by multi-step CA-TIMS measurements of closed-system natural zircon samples, Chem Geol, 275(3-4), 186-198.

Mazzarini, F., G. Musumeci, D. Montanari, and G. Corti (2010), Relations between deformation and upper crustal magma emplacement in laboratory physical models, Tectonophysics, 484(1-4), 139-146.

Mazzini, A., H. Svensen, H. A. Leanza, F. Corfu, and S. Planke (2010), Early Jurassic shale chemostratigraphy and U-Pb ages from the Neuquén Basin (Argentina): Implications for the Toarcian Oceanic Anoxic Event, Earth Planet Sc Lett, 297(3-4), 633-645.

McCaffrey, R. (1996), Slip partitioning at convergent plate boundaries of SE Asia, Geological Society, London, Special Publications, 106(1), 3-18.

McDonough, W. F., and S. s. Sun (1995), The composition of the Earth, Chem Geol, 120(3), 223-253.

Meijer, P. T., R. Govers, and M. J. R. Wortel (1997), Forces controlling the present-day state of stress in the Andes, Earth Planet Sc Lett, 148(1–2), 157-170.

Messager, G., B. Niviere, J. Martinod, P. Lacan, and J. P. Xavier (2010), Geomorphic evidence for Plio-Quaternary compression in the Andean foothills of the southern Neuquen Basin, Argentina, Tectonics, 29.

Miranda, F., A. Folguera, P. R. Leal, J. A. Naranjo, and A. Pesce (2006), Upper Pliocene to Lower Pleistocene volcanic complexes and Upper Neogene deformation in the south-central Andes (36°30'–38°S), Geological Society of America Special Papers(407), 287-298.

Miura, S., Ueki, S., Sato, T., Tachibana, K., and Hamaguchi, H. (2000), Crustal deformation associated with the 1998 seismo-volcanic crisis of Iwate Volcano, Northeastern Japan, as observed by a dense GPS network, Earth Planets Space,(52), 1003–1008.

Mo, X. X., Z. Q. Hou, Y. L. Niu, G. C. Dong, X. M. Qu, Z. D. Zhao, and Z. M. Yang (2007), Mantle contributions to crustal thickening during continental collision: Evidence from Cenozoic igneous rocks in southern Tibet, Lithos, 96(1-2), 225-242.

Montanari, D., G. Corti, and A. Simakin (2010), Magma chambers and localization of deformation during thrusting, Terra Nova, 22(5), 390-395.

Musumeci, G., F. Mazzarini, G. Corti, M. Barsella, and D. Montanari (2005), Magma emplacement in a thrust ramp anticline: The Gavorrano Granite (northern Apennines, Italy), Tectonics, 24(6).

Neumann, E. R., H. Svensen, C. Y. Galerne, and S. Planke (2011), Multistage Evolution of Dolerites in the Karoo Large Igneous Province, Central South Africa, J Petrol, 52(5), 959-984.

Odé, H. (1957), Mechanical analysis of the dike pattern of the Spanish Peaks area, Colorado, Geol Soc Am Bull, 68(5), 567-576.

Pardo-Casas, F., and P. Molnar (1987), Relative motion of the Nazca (Farallon) and South American Plates since Late Cretaceous time, Tectonics, 6(3), 233-248.

Ramos, V., and E. Rolleri (1978), Estructura, paper presented at Congreso Geológico Argentino.

Ramos, V. A. (1981), Descripción geológica de la hoja 33c, Los Chihuidos Norte, Provincia del Neuquén, Boletín(182), 5-98.

Ramos, V. A., and M. Barbieri (1989), El volcanismo Cenozoico de Huantraico: edad y relaciones

isotópicas iniciales, provincia del Neuquén, Revista de la Asociación Geológica Argentina, 43, 210 – 223.

Ramos, V. A., and A. Folguera (2005), Tectonic evolution of the Andes of Neuquén: Constraints derived from the magmatic arc and foreland deformation, Geological Society of London - Special Publication, 252, 15.

Ramos, V. A., and S. M. Kay (2006), Overview of the tectonic evolution of the southern Central Andes of Mendoza and Neuquén (35°-39° S), Evolution of an Andean Margin: A Tectonic and Magmatic View from the Andes to the Neuquén Basin (35°-39° S), 407, 1.

Rollinsson, H. R. (1993), Using Geochemical Data: Evaluation, Presentation, Interpretation, 352 pp. pp., Prentice Hall UK.

Roman-Berdiel, T., D. Gapais, and J. P. Brun (1995), Analogue models of laccolith formation, J Struct Geol, 17(9), 1337-1346.

Rosello, E., P. Cobbold, M. Diraison, and N. Arnaud (2002), Auca Mahuída (Neuquén Basin, Argentina): A quaternary shield volcano on a hydrocarbon-producing substrate, paper presented at 5th International Symposium Andean Geodynamics.

Rubin, A. M. (1993), Dikes vs Diapirs in Viscoelastic Rock Earth Planet Sc Lett, 119(4), 641-659.

Rubin, A. M. (1995), Propagation of Magma-Filled Cracks, Annu Rev Earth Pl Sc, 23, 287-336.

Rudnick, R. L. (2005), Treatise on Geochemistry: The Crust, Elsevier Science Limited.

Saal, A., F. Frey, D. Delpino, and A. Bermudez (1993), Geochemical characteristics of alkalic basalts erupted behind the Andean volcanic front (35-37 S); constraints on sources and processes involved in continental arc magmatism, EOS, 74, 43.

Schärer, U. (1984), The effect of initial 230Th disequilibrium on young U-Pb ages: the Makalu case, Himalaya, Earth Planet Sc Lett, 67(2), 191-204.

Schellart, W., D. Stegman, and J. Freeman (2008), Global trench migration velocities and slab migration induced upper mantle volume fluxes: Constraints to find an Earth reference frame based on minimizing viscous dissipation, Earth-Sci Rev, 88(1), 118-144.

Schellart, W., J. Freeman, D. Stegman, L. Moresi, and D. May (2007), Evolution and diversity of subduction zones controlled by slab width, Nature, 446(7133), 308-311.

Schoene, B., C. Latkoczy, U. Schaltegger, and D. Günther (2010), A new method integrating high-precision U-Pb geochronology with zircon trace element analysis (U-Pb TIMS-TEA), Geochim Cosmochim Ac, 74(24), 7144-7159.

Schwarz, E., and J. A. Howell (2005), Sedimentary evolution and depositional architecture of a

lowstand sequence set: the Lower Cretaceous Mulichinco Formation, Neuquén Basin, Argentina, Geological Society, London, Special Publications, 252(1), 109-138.

Seghedi, I., H. Downes, Z. Pécskay, M. F. Thirlwall, A. Szakács, M. Prychodko, and D. Mattey (2001), Magmagenesis in a subduction-related post-collisional volcanic arc segment: the Ukrainian Carpathians, Lithos, 57(4), 237-262.

Sibson, R. H. (1996), Structural permeability of fluid-driven fault-fracture meshes, J Struct Geol, 18(8), 1031-1042.

Sibson, R. H. (1998), Brittle failure mode plots for compressional and extensional tectonic regimes, J Struct Geol, 20(5), 655-660.

Sibson, R. H. (2003), Brittle-failure controls on maximum sustainable overpressure in different tectonic regimes, AAPG Bulletin, 87(6), 901-908.

Somoza, R. (1998), Updated azca (Farallon)—South America relative motions during the last 40 My: implications for mountain building in the central Andean region, Journal of South American Earth Sciences, 11(3), 211-215.

Stacey, J. S., and J. D. Kramers (1975), Approximation of Terrestrial Lead Isotope Evolution by a 2-Stage Model, Earth Planet Sc Lett, 26(2), 207-221.

Steinmann, G. (1929), Geologie von Peru, 448 pp., Winter, Heidelberg.

Strömbäck, A., J. A. Howell, and G. D. Veiga (2005), The transgression of an erg - sedimentation and reworking/soft-sediment deformation of aeolian facies: the Cretaceous Troncoso Member, Neuquén Basin, Argentina, Geological Society, London, Special Publications, 252(1), 163-183.

Tankard, A. J., et al. (1995), Structural and tectonic controls of basin evolution in southwestern Gondwana during the Phanerozoic; Petroleum basins of South America, American Geological Institute., 62, 5-52.

Tebbens, S., and S. Cande (1997), Southeast Pacific tectonic evolution from early Oligocene to Present, Journal of Geophysical Research, 102(B6), 12061-12012,12084.

Thorpe, R. S., P. W. Francis, L. O'Callaghan, R. Hutchison, and J. S. Turner (1984), Relative Roles of Source Composition, Fractional Crystallization and Crustal Contamination in the Petrogenesis of Andean Volcanic Rocks [and Discussion], Philosophical Transactions of the Royal Society of London. Series A, Mathematical and Physical Sciences, 310(1514), 675-692.

Tibaldi, A. (1995), Morphology of pyroclastic cones and tectonics, J. Geophys. Res., 100(B12), 24521-24535.

Tibaldi, A. (2005), Volcanism in compressional tectonic settings: Is it possible?, Geophys Res Lett, 32(6).

Tibaldi, A. (2008), Contractional tectonics and magma paths in volcanoes, Journal of Volcanology and Geothermal Research, 176(2), 291-301.

Tibaldi, A., and F. A. Pasquare (2008), A new mode of inner volcano growth: The "flower intrusive structure", Earth Planet Sc Lett, 271(1-4), 202-208.

Tibaldi, A., F. Pasquarè, and D. Tormey (2010), Volcanism in Reverse and Strike-Slip Fault Settings, New Frontiers in Integrated Solid Earth Sciences, edited by S. Cloetingh and J. Negendank, pp. 315-348, Springer Netherlands.

Townend, J., and M. D. Zoback (2006), Stress, strain, and mountain building in central Japan, J Geophys Res-Sol Ea, 111(B3).

Trumbull, R. B., U. Riller, O. Oncken, E. Scheuber, K. Munier, and F. Hongn (2006), The Time-Space Distribution of Cenozoic Volcanism in the South-Central Andes: a New Data Compilation and Some Tectonic Implications, The Andes, edited by O. Oncken, G. Chong, G. Franz, P. Giese, H.-J. Götze, V. A. Ramos, M. R. Strecker and P. Wigger, pp. 29-43, Springer Berlin Heidelberg.

Uliana, M., D. Dellapé, and G. Pando (1973), Estratigrafía, estructura y posibilidades petroleras del extremo noroeste de la provincia del Neuquén, Buenos Aires, Yacimientos Petrolíferos Fiscales Open-File Report.

Uliana, M. A., M. E. Arteaga, L. Legarreta, J. J. Cerdán, and G. O. Peroni (1995), Inversion structures and hydrocarbon occurrence in Argentina, Geological Society, London, Special Publications, 88(1), 211-233.

Urien, C. M., Zambrano, J.J (1994), Petroleum systems in the Neuquén Basin, Argentina, in The Petroleum System - From Source to Trap edited by L. B. Magoon, Dow, W.G, pp. 513–534, American Association of Petroleum Geologists Memoir.

van der Werff, W. (2000), Backarc deformation along the eastern Japan Sea margin, offshore northern Honshu, Journal of Asian Earth Sciences, 18(1), 71-95.

Veiga, G. D., J. A. Howell, and A. Strömbäck (2005), Anatomy of a mixed marine-non-marine lowstand wedge in a ramp setting. The Record of a Barremian-Aptian complex relative sea-level fall in the central Neuquén Basin, Argentina, Geological Society, London, Special Publications, 252(1), 139-162.

Vergani, G. D., A. J. Tankard, H. D. Belotti, and H. J. Welsink (1995), Tectonic evolution and paleogeography of the Neuquén basin, Argentina, in Petroleum basins of South America: AAPG Memoir edited by A. J. Tankard, Suárez S., Welsink, H.J., pp. 383–402.

Vergara, M., and F. Munizaga (1974), Age and evolution of the Upper Cenozoic andesitic volcanism in central-south Chile, Geol Soc Am Bull, 85(4), 603-606.

Walker, G. P. L. (1986), Koolau Dike Complex, Oahu - Intensity and Origin of a Sheeted-Dike

Complex High in a Hawaiian Volcanic Edifice, Geology, 14(4), 310-313.

Watanabe, T., T. Koyaguchi, and T. Seno (1999), Tectonic stress controls on ascent and emplacement of magmas, Journal of Volcanology and Geothermal Research, 91(1), 65-78.

Weaver, C. E. (1931), Paleontology of the Jurassic and Cretaceus of west central Argentina, 469 pp., University of Washington press, Seattle.

Wichmann, R. (1934), Contribución al conocimiento geológico de los territorios del Neuquén y del Río Negro, Talleres Gráficos del Ministerio de Agricultura de la Nación.

Windhausen, A. (1914), Contribución al conocimiento geológico de los territorios del Río Negro y Neuquén, con un estudio de la región petrolífera de la parte central del Neuquén (Cerro Lotena y Covunco), paper presented at Anales del Ministerio de Agricultura, Sección Geología, Mineralogía y Minería.

Yoshida, T. (2001), The evolution of arc magmatism in the NE Honshu arc, Japan, Tohoku Geophysical Journal(32), 131-149.

Zapata, T., A. Folguera, G. Veiga, A. Spalletti, J. Howell, and E. Schwarz (2005), Tectonic evolution of the Andean fold and thrust belt of the Southern Neuquén basin, Argentina, Geological Society of America - Special Publication, 252, 37.

Zellmer, G. F., C. Annen, B. L. A. Charlier, R. M. M. George, S. P. Turner, and C. J. Hawkesworth (2005), Magma evolution and ascent at volcanic arcs: constraining petrogenetic processes through rates and chronologies, Journal of Volcanology and Geothermal Research, 140(1-3), 171-191.

Zoback, M. L. (1992), First-and second-order patterns of stress in the lithosphere: the world stress map project.

Zöllner, W., and A. Amos (1973), Descripción geológica de la Hoja 32b, Chos Malal (Provincia del Neuquén), 91.